Development of an air-stable, high energy density printed silver oxide battery for printed electronics

Kyle Braam

Electrical Engineering and Computer Sciences
University of California at Berkeley

Technical Report No. UCB/EECS-2015-33
http://www.eecs.berkeley.edu/Pubs/TechRpts/2015/EECS-2015-33.html

May 1, 2015

Copyright © 2015, by the author(s).
All rights reserved.

Permission to make digital or hard copies of all or part of this work for personal or classroom use is granted without fee provided that copies are not made or distributed for profit or commercial advantage and that copies bear this notice and the full citation on the first page. To copy otherwise, to republish, to post on servers or to redistribute to lists, requires prior specific permission.

Development of an air-stable, high energy density printed silver oxide battery for printed electronics

by

Kyle Theunis Braam

A dissertation submitted in partial satisfaction of the

requirements for the degree of

Doctor of Philosophy

in

Engineering - Electrical Engineering and Computer Sciences

in the

Graduate Division

of the

University of California, Berkeley

Committee in charge:

Professor Vivek Subramanian, Chair

Professor Ana Claudia Arias

Professor Paul Wright

Spring 2014

Abstract

Development of an air-stable, high energy density printed silver oxide battery for printed electronics

by

Kyle Theunis Braam

Doctor of Philosophy in Engineering – Electrical Engineering and Computer Sciences

University of California, Berkeley

Professor Vivek Subramanian, Chair

Printed batteries are emerging battery technology that has the potential to enable the production of cheap, small form factor, flexible batteries capable of powering a diverse set of existing and emerging applications such as RFID tags, flexible displays, and distributed sensors. Partially printed battery systems have been demonstrated with various chemistries, but what is needed is a low cost, air stable method of fully printing a high energy density batteries. The silver oxide chemistry is attractive for developing a printed battery as this chemistry has demonstrated high energy densities and is capable of air stable fabrication processes due to its aqueous based chemistry. To facilitate the advancement of this technology, material components and printing techniques need to be developed to demonstrate a printed silver oxide battery.

In this thesis, I will present a printed, high energy density silver oxide battery using stencil printing. A key development of this work is the demonstration of a novel photopolymerized polyacrylic acid separator layer. The mechanical and conductivity properties of this layer are characterized and optimized for an alkaline silver oxide battery. The incorporation of this layer has enabled a printed battery capable of high rates of discharge. The batteries show no difference in discharge upon flexing at a bend radius of 1.0 cm, indicating their potential in flexible applications. The fabricated batteries have demonstrated high energy densities of 10 mWhr cm^{-3} and areal capacities of 5.4 mAhr cm^{-2}, which satisfies the power and capacity requirements for most of the proposed applications. In addition, we have examined several printed encapsulation schemes (epoxy and silicone caulk) for encapsulating an alkaline battery.

Acknowledgements

I have had a great experience as a graduate student in the electrical engineering department at the University of California, Berkeley. I would like to thank all the people who have made my experience enjoyable for the six years that I have been here at Cal.

I would like to thank the people who have contributed to the battery project. I thank Dan Steingart and Steve Volkman who had worked on the printed battery project before I started to work on it and set the groundwork for my research. I thank Christine Ho for her discussions about battery chemistry and all her guidance about printed batteries. Working with her as part of the Cleantech to Market class was an extremely useful experience. I also appreciate the funding sources, the National Science Foundation (NSF) and the Semiconductor Research Corporation (SRC), that have supported my research here at UC Berkeley. Without them, this work would not be possible.

I would like to thank the past and current members of the organic electronics group who have made my experience at Berkeley memorable. Their support, conversations, and companionship have been invaluable during my graduate career. I would like to thank Steve Volkman for his many hours of conversation about science, philosophy, and life. I also would like to thank Feng Pan for his conversations about electrochemistry and our random jogs that we go on. I thank Shong Yin for our conversations about technology and life. I also appreciate all the advice that I have received from Alejandro de la Fuente Vornbrock as a first year grad student and as an intern at HP Labs. I appreciate the efforts from Jaewon Jang, Hongki Kang, and Eung Seok Park to teach me some Korean and to help me as a fellow graduate student. I thank Jake Sadie for his humor and his service to the group, Sarah Swisher for her thoroughness, Rungrot (Jack) Kitsomboonloha for the interesting discussions about printing, Gerd Grau for his enthusiasm, Rumi Karim for his thoughtfulness, and Andre Zeumault for his deep and insightful conversations about semiconductor physics. You all have made being part of this group a great and supportive experience.

I would not be here at the University of California, Berkeley without all of the people who supported me through my undergraduate career at Macalester College. I thank the Mac Pack and Matt Haugan for their companionship, support, and runs in rain or snow. My undergraduate research advisor, Jim Doyle, was a key person who started my scientific career in semiconductor physics. I thank him for all his efforts to teach me about sputtering and semiconductor characterization techniques. I learned a lot from him while performing research on RF sputtered zinc oxide films for my Honors thesis. I would also like to thank Tonnis Ter Veldhuis and James Heyman for their support and guidance.

I also thank Vivek Subramanian for his advice, tutorship, and support that he has provided to me throughout my graduate career. He has been a source of inspiration for me. His enthusiasm in the classroom and for research has profoundly influenced me. I appreciate the freedom and support he has provided me that has allowed me to advance as a researcher and as a person. I am grateful to be able a part of his group and to have worked with him. I also would like to thank professor Ana Claudia Arias, Jeff Bokor, Vivek Subramanian, and Elton Cairns for being on my qualifying committee. I also would like to thank Vivek Subramanian, Ana Claudia Arias, and Paul

Wright for being on my Ph.D. thesis committee and taking the time to read my thesis. Thank you for all your support and insightful comments.

I also want to thank my family for all their love and help. I am here today because of you. Thank you mom, dad, Eric, and Krista for all that you have done. I want to give a special thanks to my girlfriend, Clarissa Liang, for her support and her patience as I have finished my thesis.

Table of Contents

Chapter 1. Introduction 1

1.1 Development of printed electronics 1

1.2 Printed energy systems 2

1.3 Advantages of printed batteries 3

1.4 Objectives of this work 4

1.5 Organization 4

Chapter 2. Background on printed batteries for printed electronic applications 6

2.1 Printing techniques 6

2.1.1 Inkjet printing 6

2.1.2 Roll-to-roll printing 7

2.1.3 Stencil printing and screen printing 8

2.1.4 Extrusion printing 9

2.1.5 Printing techniques applied to printed batteries 9

2.2 Printed battery applications 10

2.2.1 Printed battery voltage and power requirements 10

2.2.2 Example application for printed batteries: printed RFID 11

2.3 Printed and thin film batteries 12

2.3.1 Printed battery architectures 12

2.3.2 Lithium-ion batteries 13

2.3.3 Alkaline batteries: Zn-MnO_2 printed batteries 16

2.3.4 Alkaline batteries: Silver-zinc chemistry 17

2.4 Advantages and disadvantages of silver oxide batteries for printed electronics 20

2.4.1 Cost analysis of the Zn-Ag_2O battery 21

2.5 Discharge characteristics 22

2.6 Conclusion 24

Chapter 3. Planar printed battery 25

3.1 Current collector 26
3.2 Printed alkaline separator 26
3.2.1 Ideal properties of an alkaline separator 26
3.2.2 Printed alkaline separators 27
3.3 Printed separator for an alkaline silver oxide battery 32
3.3.1 Separator optimization 33
3.3.2 Separator Optimization: Conclusion 34
3.4 Silver oxide electrode optimization 34
3.5 Zinc electrode optimization 37
3.6 Three-electrode measurement 38
3.7 Performance of a planar printed silver oxide battery 39
3.8 Conclusion 40
Chapter 4. Printed battery with vertical architecture 41
4.1 Printed current collector 41
4.1.1 Bottom printed current collector 42
4.1.2 Top printed current collector 44
4.2 Printed PAA separator 46
4.2.1 Photopolymerization of the PAA gel separator 48
4.2.2 Mechanical properties of PAA separator 50
4.2.3 Printability of the PAA separator 51
4.2.4 Swelling properties of PAA separator 52
4.2.5 Conductivity of the PAA separator 54
4.2.6 Optimized alkaline separator 56
4.3 Printed electrodes 57
4.3.1 Printed zinc electrode 57
4.3.2 Printed silver oxide electrode 58
4.4 Discharge performance 59

4.5 Conclusion 61
Chapter 5. Battery Characterization 63
5.1 Polarization curve 63
5.2 Electrochemical impedance spectroscopy (EIS) 65
5.3 EIS modeling 67
5.3.1 Conductive electrodes 67
5.3.2 Partially polarizable electrodes 68
5.4 Impedance spectroscopy of a PAA electrolyte 70
5.4.1 Experimental setup 70
5.4.2 Measurement results and discussion 70
5.5 EIS: Three-electrode measurement 74
5.5.1 Experimental setup 74
5.5.2 Measurement results and discussion 75
5.6 Application of the EIS data to the polarization curve 78
5.7 Conclusion 79
Chapter 6. Printed alkaline battery encapsulation 81
6.1 Alkaline battery requirements 81
6.2 Packaging in commercial alkaline batteries 82
6.3 Printed encapsulation schemes 83
6.4 Encapsulation metrics 86
6.4.1 Conductivity change measurements 87
6.4.2 Open circuit measurements 87
6.5 Epoxy encapsulation 89
6.5.1 Conductivity change measurements 89
6.6 Silicone encapsulation 90
6.6.1 Conductivity change measurements 91
6.7 Corrosion of the zinc electrode 94

6.8 Conclusion 95
Chapter 7. Conclusions and Future Work 96
7.1 Conclusions 96
7.2 Future Work 97
References 99

Chapter 1. Introduction

1.1 Development of printed electronics

Printed electronics is a growing field that has the potential for cheap, flexible and large area electronics. The printed electronics consists of a wide range of technologies including photovoltaics [1], displays [2], memories [3], and logic devices [4] among many others. The future economic impact of printed electronics is unknown as there are very few printed products on the market. However, market studies from IDTechEx have projected the market for printed electronics to be worth $30 billion in 2015 and upwards of $96 billion in 2020 [5]. The interest in printed electronics results from the unique advantages of the printing process.

Printing is usually an additive process where material is put down in specific positions without any masking steps or material removal [6]. The cost savings of printed electronics come from the fact that an additive process reduces the number of processing steps and waste produced. This allows for efficient use of expensive inks and materials. The printing process is in contrast to conventional lithography which is a subtractive process. This requires not only material deposition steps, but also multiple photoresist depositions, exposures to define areas to be removed or kept, photoresist developing steps and etching steps to remove material. All of these processes add to the collective cost to produce the electronic circuit.

Another advantage of printed electronics is that some printing processes, such as gravure, can be incorporated into a roll-to-roll (R2R) process which would allow for circuit or device fabrication on a similar scale to newspaper printing. The printing process can be fast, allowing for high throughput with printing spends of 100km h^{-1} or 100m min^{-1} [7]. Printing also allows for the use of cheap, flexible plastic substrates rather than the rigid, expensive silicon wafers used in the conventional semiconductor industry. This has the potential for the creation of “unbreakable” electronics or flexible electronics. A further advantage of using plastic substrates for printed electronics is that the cost per area of a plastic substrate, such as polyethylene terephthalate (PET) or polyethylene naphthalene (PEN), is low [8].

The printing resolution and low performance of printed materials limits the number and performance of the printed transistors in a given printed electronics application. As a result, the cost per transistor will be much higher compared to silicon based transistors [5]. However, printed electronics will likely have a cost benefit per area rather than per transistor for simple circuits or large area applications. The printing process is not likely to be used for applications that require high efficiency electronics, very small features, complex processes that require multiple layers, and processes that require significant transistor performance. Despite these constraints, there are many applications that will benefit from printed electronics. These examples include relatively simple, large area applications such as printed displays [9], wireless sensors [10], and RFID tags [11]. Printed electronics also has the potential to enable new fields such as wearable electronics [12], and electronic skin [13]. These fields will benefit from the fact that the printing can occur on a flexible substrate. These examples above show the growth and potential for the emerging field of printed electronics.

However, bringing the printed electronics field to the point of commercialization requires the development of new printing techniques, tools, materials and substrates. For example, this includes development of gravure tools to allow for fast, high resolution printing processes [14]. Significant materials development needs to occur to realize low processing temperature and high performance semiconductor materials, metals and dielectrics. In addition to the work needed to develop the materials and processes for printed circuits, work needs to be done to develop printed energy systems that are low cost and capable of being integrated with the printing process. One key technology that needs to be developed is the field of printed energy systems. This includes developing the printing techniques and materials required for a printed power source.

1.2 Printed energy systems

There have been numerous printed electronics demonstrations including printed RFID tags, photovoltaic, wireless sensors and electronic paper. Many techniques could be used to reduce the energy used during the operation of these circuits such as low power circuits [15] and energy harvesting [16]. However, all these techniques still require a power source or a way to supply or store energy. Besides using power from a grid, there are several other ways which printed electronic based systems can be powered which include energy-scavenging, capacitors and batteries. Energy scavenging devices, such as inductive coupling [17], thermoelectrics [18], solar cells [19] and piezoelectric materials [20] are capable of converting energy from the environment, but these systems often require batteries or capacitors to store the generated energy to deal with the intermittency and unpredictability of the environment. The power that can be harvested from the environment is low; harvest power is on the order of 1-330 $\mu W/cm^3$ and depends on the method of conversion, the ambient source and device design [21]. For these reasons, batteries or capacitors are still likely to be required in addition to energy harvesting schemes.

Capacitors have great power density, but poor specific energy density compared to batteries (Fig. 1.1). They are great at storing small amounts of energy and having high power density. Capacitors store charge on two conductors separated by a dielectric. The charge stored on a capacitor is related to voltage by the following equation:

$$Q = CV$$

where C is the capacitance of the dielectric, and V is the voltage difference between the two conductors. Super capacitors which bridge the gap between batteries and capacitors store charge through a combination of double-layer capacitance and faradic reactions, such as intercalation or electrosorption. Work is currently being done to improve the energy densities of capacitors up to 10 Wh kg^{-1} and power densities up to 1-2 kW kg^{-1} [22]. There is interest in developing printed capacitors for printed electronics with several reports demonstrating high power densities [23], [24]. Developing capacitors is a worthwhile goal, but for the scope of this thesis, we focus on printed batteries.

Batteries are commonly used over capacitors because of the higher gravimetric energy density, volumetric density and suitable power density for most applications. This is seen in the

Ragone plot (Fig. 1.1) which plots the specific energy versus specific power. We see that battery chemistries have a higher specific energy compared to capacitors and Supercapacitors. The energy from a battery is generated from two chemical reactions: an oxidation and a reduction reaction. The potential difference between these two reduction potentials provides the voltage of the battery. Cycle life and shelf life will depend on the battery chemistry and battery design. Some battery chemistries are better suited for single use batteries or otherwise known as primary batteries, while others, such as lithium-ion batteries, are secondary batteries capable of discharging and charging for thousands of cycles. The high energy density, high power density and long shelf life of several years are attractive for their potential use in printed electronics. For these reasons, we have looked at developing a printed battery for printed electronics. We have specifically chosen to work with the silver oxide-zinc (Zn/Ag_2O) chemistry. The reasons for this choice will be discussed in Chapter 2.

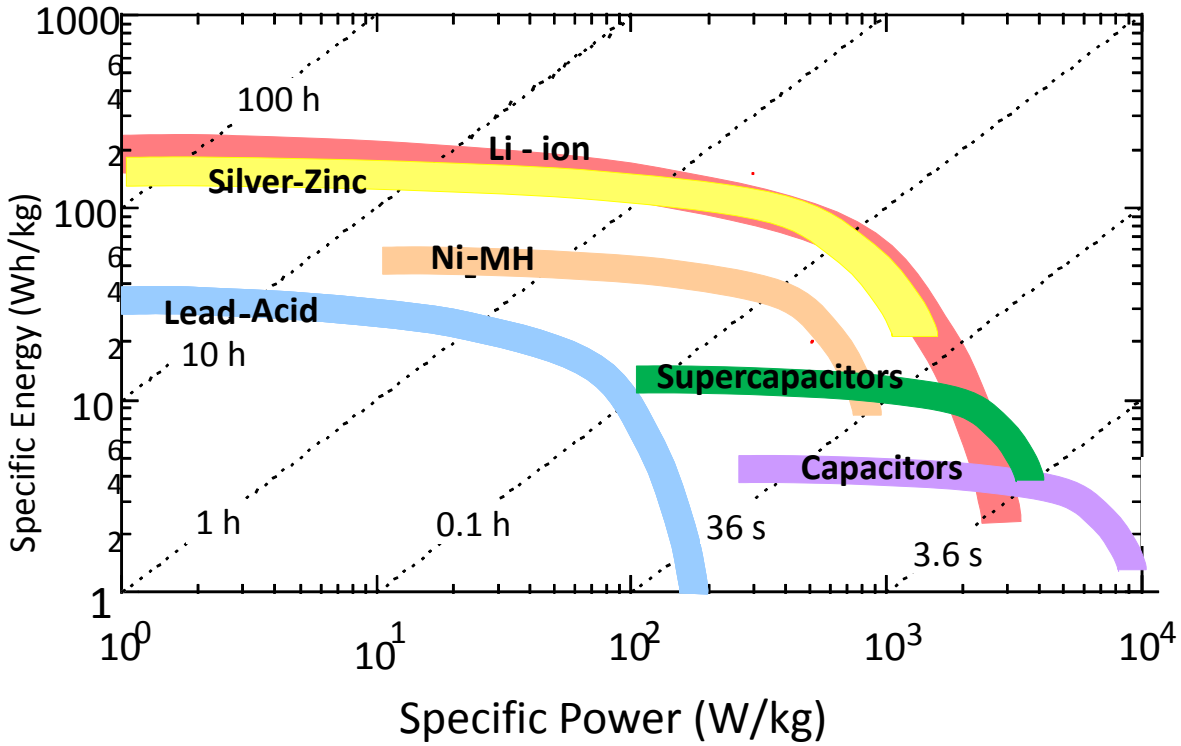

Figure 1.1 Ragone plot for various battery chemistries and capacitors (adapted from Clean Tech to Market Class 2010, UC Berkeley, Haas School of Business)

1.3 Advantages of printed batteries

Printed batteries fulfill an unmet need in printed electronics. Currently, energy to an electronics circuit is provided from the electric grid or large macro batteries such as AA or AAA batteries or coin cell batteries. Small coin cell batteries can have capacities on the order of 100-200 mAh or larger. Smaller capacity batteries are a niche market. A couple of companies, such as Solicore, produce thin, flexible low capacity batteries. For example, Solicore's Flexion line of lithium polymer batteries has a 10 mAh primary lithium battery [25]. Despite a couple of examples, there is still a lot of work that needs to occur to demonstrate low cost, small capacity

batteries, also known as microbatteries [26]. There is market not only for primary batteries, but also rechargeable secondary batteries. By developing an air stable, printed technique for fabricating batteries, we can provide a low cost microbattery suitable for applications that require a low capacity, small form factor battery.

In addition to fitting into a new capacity, printed batteries have certain benefits over conventional batteries. A printed, thin film battery deposited on a flexible substrate has the potential to be extremely flexible. This is desirable for certain thin form factor applications such as electronic paper or wearable electronics. Smart cards also would benefit from a thin form battery that could be directly printed on the card.

Printed batteries also have the potential to reduce the cost of fabrication. A printed battery could be integrated directly into the printed electronics process flow or be printed on a chip. For example, the printed battery could be integrated into the substrate of the printed electronic circuit by directly printing on the substrate. This will reduce the cost of integration, since battery holders and attachment of the battery are no longer required. The inactive material will also be reduced by using the already present electronic circuit substrate as part of the encapsulation. Another benefit is the increase in energy density due to the reduction of the inactive materials of a battery, such as the encapsulation and battery holders.

1.4 Objectives of this work

This work focuses on the development of a fully printed silver oxide battery for printed electronics applications. The chemistry and material components for the silver oxide-zinc system are well understood, with commercial silver oxide-zinc batteries already on the market. A lot of the current works have demonstrated partially printed systems that require assembly or lamination [27], [28]. To achieve a fully printed silver oxide battery requires the development of new processes and materials.

Using several printing processes (extrusion printing and stencil printing), we have developed a high energy density, printed, primary battery for printed electronics. To achieve this goal requires the development of a printable separator layer. We have demonstrated a novel, photopolymerizable, polyacrylic acid gel separator that allows for direct incorporation of the separator into the battery stack. This separator is characterized in detail and optimized for good mechanical stability and high ionic conductivity. We characterize the battery performance using a technique known as electrochemical impedance spectroscopy. This technique allows us to individually isolate specific phenomena of the battery. We have also presented work on developing a printed encapsulation scheme that is compatible with the alkaline chemistry, with an aim to demonstrate an encapsulated, fully printed battery.

1.5 Organization

The topics of this thesis include electrochemistry and material development. For a good introduction to the fundamentals of electrochemistry, one should consult John Newman's "*Electrochemical Systems*" [29]. For fundamentals of electrochemical impedance spectroscopy (EIS), one should read the book *"Electrochemical impedance spectroscopy"* by Mark E. Orazem

[30]. This thesis is divided into six chapters which describe the development and characterization of a printed silver oxide battery.

Chapter 2 covers the current state of printed and thin form commercial and research batteries with an emphasis on printed batteries. We discuss the various printing techniques and their application to printed batteries. The advantages and disadvantages of different battery chemistries are analyzed for their applicability to printed batteries. In addition, a simple cost analysis for the silver oxide/zinc system is included.

Chapter 3 describes the fabrication and characterization of a planar silver oxide battery. The planar architecture allows for the development of the printed electrodes and printed separator. We introduce a three electrode technique that is capable of monitoring the state of charge during discharge.

Chapter 4 describes the development of a vertically printed silver oxide battery. To achieve this structure, required the development of a novel, photopolymerized polyacrylic acid separator layer. This layer demonstrates good mechanical properties and high ionic conductivity.

Chapter 5 examines the use of electrochemical impedance spectroscopy to characterize the chemical reactions occurring in the printed silver oxide battery. We examine the contributions to the internal resistance of the battery as a function of discharge current. We propose ways of improving the discharge potential.

Finally, chapter 6 examines printed alkaline encapsulation schemes to develop a printed means of encapsulating a silver oxide-zinc battery. The work done with the silver oxide-zinc chemistry should generalize to other alkaline battery systems, such as zinc-manganese dioxide.

Chapter 2. Background on printed batteries for printed electronic applications

In this chapter we discuss the techniques and chemistries that are used in the field of printed batteries. There are several printed techniques that are commonly used in the printed electronics field. These include: inkjet, gravure, screen printing, and extrusion printing. We examine these various techniques and discuss their disadvantage and advantages. Two of these techniques, screen printing and extrusion printing, are attractive for printing batteries as they can deposit thick films (1-100 µm); this is necessary for printing high energy batteries since areal capacity is strongly related to film thickness.

A discussion of the applications for printed batteries is included, with a focus on the particular example of RFID tags. We then examine various battery chemistries (Li-ion, Zn-Ag_2O and Zn-Mn_2O) and their advantages and disadvantages for use as a printed battery chemistry in terms of chemistry, cycle life, and energy density. We examine commercial and literature examples of printed battery systems and discuss the features of each battery system. We explain why we have decided to work with Zn-Ag_2O chemistry to develop a printed battery. We also briefly discuss some of the battery characterization methods used to quantify the printed battery performance.

2.1 Printing techniques

There are numerous techniques that have been used to demonstrate printed electronics, such as gravure, flexography printing, offset printing, inkjet, stencil, and screen printing (Figure 2.1). Each process varies in terms of ink requirements, minimum feature size achievable, registration limits and achievable throughput. Ultimately, each technique has its advantages and disadvantages. For example, inkjet printing allows for printing of customizable patterns, but suffers from low throughput. Current research is still underway to determine what the physical limitations associated with each technique are in terms of print resolution, alignment resolution and throughput. In the following sections, the major printing techniques are briefly discussed.

2.1.1 Inkjet printing

Inkjet is a widely used printing technique that is used to print electronic and optical devices [31]. Inkjet is a versatile printing tool that is capable of droplet on demand printing (DOD). This enables great flexibility; once a pattern has been made, an inkjet printer can print drops corresponding to the pattern size and shape. Multiple layers of different material can be built up using print heads filled with different inks [32].

There are two main ways an inkjet printer deposits droplets of ink from a print head: a thermal process and a piezoelectric process [31]. In the thermal process, ink in a chamber is heated up by applying current through a heater which in turns heats the ink. This evaporates the ink which results in a bubble that expands and pushes ink out of the chamber.

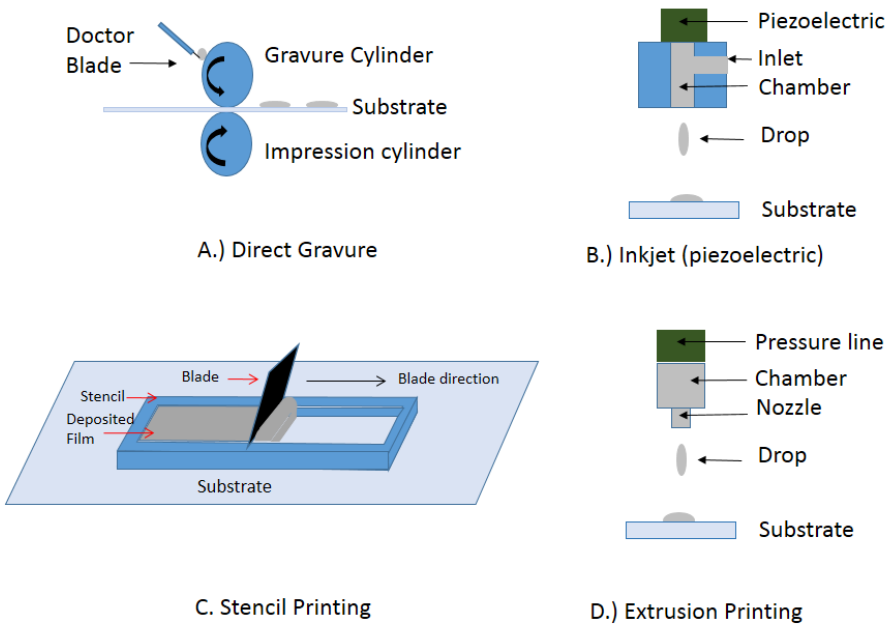

Figure 2.1 Common printing techniques A.) Direct Gravure B.) Inkjet C.) Stencil Printing. D.) Extrusion Printing

Inkjet is a versatile tool capable of obtaining feature sizes in the range of 20-50 ums [33]. Inkjet requires inks of relatively low viscosity (2-30 cP) to be printable. The ultimate feature size is dependent on the ink properties, printing technique, surface properties, printhead and substrate temperatures [34]. For example, smaller features can be made by tuning the surface properties of the substrate, such as making areas hydrophobic or hydrophilic to control wetting of the ink on the substrate. Two disadvantages of inkjet printing are the limitation in printing speed and the small amount of the material printed. Specifically, the dry thickness is given by:

$$d = N_d V_d \frac{c}{\rho}$$

where N_d is the number of droplets delivered per area, V_d is the volume of the droplets, c is the concentration, and ρ is the density of the ink [35]. Inkjet printers print extremely small amounts of fluid on the order of 1-100 µL. As a result, not a lot of material is deposited during the printing process and therefore, inkjet printing tends to be slow. However, the throughput and thickness can be increased by increasing the number of nozzles. This introduces complexity to the printing process [36].

2.1.2 Roll-to-roll printing

Roll-to-roll (R2R) printing is a broad category that contains gravure, flexography and offset lithography [37]. Roll-to-roll printing is attractive for large-scale manufacturing of printed electronics so that electronics can be printed in manner similar to the way paper newspapers are

printed. Such a technique allows for a fast, cheap, mass manufacturing process of printed electronics.

One specific R2R printing technique that is of interest is direct gravure due to its high speed [37]. In gravure printing, ink is filled into wells on a gravure cylinder (Fig. 2.1 A). A doctor blade wipes excess ink from the gravure cylinder. An impression cylinder holds the substrate in contact with the gravure cylinder. As the cylinders are rolled across the substrate, ink is transferred from the wells of the gravure cylinder to the substrate. Through optimizing ink viscosities, substrate properties and printing speeds, printed line spacings as small as 2 um can be achieved at speeds as high as 1 m/s [14]. The thickness of the transferred ink depends on the cell depth, line width and ink properties. Using gravure thickness of up to 0.4 µm have been demonstrated [38]. Gravure is useful for printing thin layers of material quickly. This technique shows promise in terms of enabling a low cost and high throughput fabrication of printed electronics applications.

2.1.3 Stencil printing and screen printing

Stencil printing and screen printing are similar techniques where ink is passed through a stencil to the substrate [39]. Currently, stencil and screen printing are commonly used techniques to deposit solder on PCB boards in one step [40]. Now the technique is being developed for its use in other printed electronics applications, such as printed capacitors [41] and resonant circuits (also known as electronic article surveillance (EAS) tags) [42].

Stencil printing consists of a single stencil that has holes at different locations on the stencil. First, the stencil is placed on the substrate. Then, ink is placed in the holes of the stencil, and a doctor blade is run over the stencil to remove excess ink (Fig 2.1 C). The stencil is removed from the substrate and the ink is left on the substrate. An annealing step can be performed to remove excess solvent from the ink.

A related technique used to deposit patterns of material is screen printing (Fig 2.2). Screen printing is commonly used to deposit material, such as inks for t-shirts and logos. The screen printing process allows for the deposition of multiple layers. In the screen printing technique, a screen with meshes of various sizes is filled with an ink. The ink used for screen printing has a high viscosity (1,000-50,000 cPs) and low volatility. [43] A squeegee is dragged across the screen surface to transfer the ink from the screen to the substrate. As the squeegee moves across the screen, the ink is squeezed out of the mesh by capillary action onto the substrate. The film thickness is determined by the ink properties and mesh size.

Both stencil and screen printing are useful techniques for printed electronics applications. Stencil printing has advantages of longer stencil lifetimes, higher and more controlled ink/paste depths and less snap-off distances (the distance of the screen/stencil and the substrate) [40]. On the other hand, screen printing has the advantage of typically cheaper screens, and the technique allows for printing over a large area, thus increasing throughput. Development of both of these techniques in the field of printed electronics will likely continue.

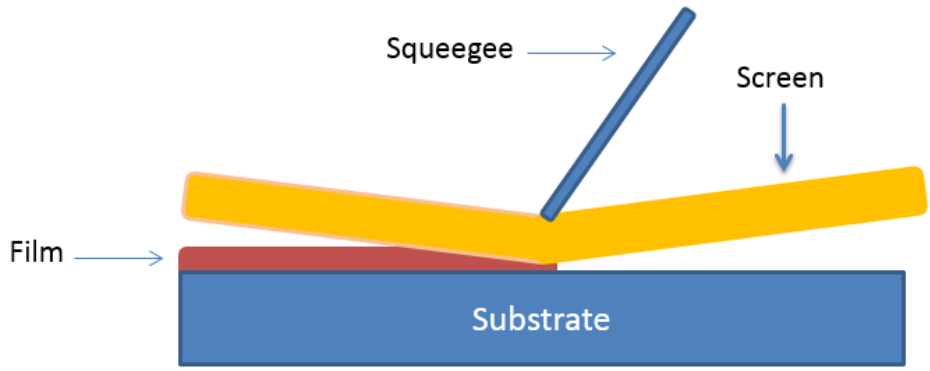

Figure 2.2 Screen printing process. Ink is transferred from the screen to the substrate by application of a squeegee.

2.1.4 Extrusion printing

Extrusion printing or direct write pneumatic dispenser printing is a printing technique that is used to print relatively thick films [44], [45]. Extrusion printing or flow-based printing uses a pneumatic-controlled injector to create a positive pressure to dispense ink through a syringe needle (Fig 2.1 D). This technique is capable of printing feature sizes of 50 µm and film thicknesses of 10-100 µm. The feature size is determined by the needle size, the ink properties and the print spacing. The inner diameter of the syringe needle can be chosen down to 100 µm, and smaller diameter needles can be made by pulling borosilicate glass. The ink, or slurries, can have high viscosities ranging from 5 to 1,000,000 cp and can contain material that has large particle sizes, for example, on the order of 1-20 µm. The slurries are typically a suspension consisting of the material one wishes to deposit, the solvent and filling materials such as polymers.

The extrusion printing technique has been used to deposit materials that require large features or for applications that require large areas. Specifically, extrusion printing has been used to demonstrate capacitors [46], batteries [45], [47] and thermoelectric materials [18]. In the future, this technique will likely be applied to other areas of printed electronics that require thicker layers.

2.1.5 Printing techniques applied to printed batteries

Inkjet, gravure, stencil/screen and extrusion printing have advantages and disadvantages with respect to each other. Table 2.1 shows a comparison of the various limitations and properties of these common printing techniques. The values listed are based on reported literature values, and work is currently being done to determine what the fundamental limitations associated with each printing technique are. However, based on the current techniques available, we can select the appropriate printing technique for developing a high energy density, printed battery.

Printing Method	Viscosity (Pa-s)	Layer Thickness (µm)	Feature Size (µm)	Registration (µm)	Throughput (m^2/s)
Gravure Printing	0.01-0.2	<0.1-8	10	>20	3-60
Flexography Printing	0.05-0.5	0.04-2.5	80	<200	3-30
Inkjet Printing	0.001-0.04	0.05-20	2-50	5-20	0.01-.05
Extrusion Printing	0.01-100	10-100	50-100	>20	0.01-0.1
Screen Printing/Doctor Blading	100-1000	0.015-100	20-100	>25	2-3

Table 2.1 Performance and limitations of printing techniques used in printed electronics [26],[48],[14] .

In designing a high energy density battery, we need to be concerned about the feature size, the thickness of the printed layer and the registration capabilities. The feature size can be large due the fact that most printed battery applications will require capacities with an aerial requirement greater than 100x100 um^2. Low capacity batteries with µAh capacities may require smaller sizes and thicknesses. However, for our applications and areal energy capacities, we are looking at larger areas and thicker films (t > 1 µm). Registration may be an issue to prevent shorting of electrodes, however, this can be avoided by designing enough tolerance into the layers, especially into the separator layer. The separator layer area should have a larger area than the electrode area. One of the key properties that is required to develop a high areal capacity battery is film thickness. For this reason, we have decided to use a combination of extrusion printing and stencil printing for the fabrication of our printed batteries since both of these techniques are capable of depositing the required thicknesses. Specifically, we have used extrusion printing to develop a planar printed battery and stencil printing to demonstrate a vertical printed battery.

2.2 Printed battery applications

There are many applications that could be enabled by the creation of a cheap, flexible battery. The potential applications include distributed sensors, RFID tags, and flexible displays. The exact current, voltage, power and energy density requirements will be set by the application requirements, such as the application lifetime and the material choice. However, the physical limits associated with chemistry will limit what is achievable by a printed battery in terms of voltage, or energy density.

2.2.1 Printed battery voltage and power requirements

The power and energy requirements from a battery will depend on the application and desired lifetime. The required voltage will also depend on the circuit design and materials used. Printed batteries based on lithium-ion chemistry have voltages near 3.0 V, whereas alkaline chemistries have a reduced voltage near 1.5 to 1.6 V. In order to achieve a high voltage, batteries

can be printed in a series to achieve the correct voltage for the circuit application [49]. In theory, any potential in multiples of the individual battery voltage can be realized.

Printed electronic applications or wireless sensor network applications would require capacities between 1-500 mAh capacities. The exact capacity will depend on the application power requirements, lifetime and discharge rate. Sensors that require a constant power source for monitoring the environment would also benefit from a printed battery that could be integrated into the substrate or printed on chip. One potential sensor example is that of an implantable glucose sensor [50]. This sensor is designed to monitor glucose levels and transmit the data using a low power transmitter. The peak power of this system is set by the transmitter at 3.4 mW. State of the art glucose sensors consume 10 uW during the five second measurement period. The power used during the off state is determined by the quartz crystal oscillator and control unit which is less than 1 µW. The average power consumed for the entire system is 2 µW. Assuming a seven day measurement period and a battery that has a potential of 1.5 V, we calculate that a battery should have a capacity of 0.22 mAh. If we assume an areal capacity density of 4 mAh cm^{-2}, then this would require a battery with an area of 2.4 mm^2 which is feasible for a printed battery system.

2.2.2 Example application for printed batteries: printed RFID

One of the growing technology markets is the radio-frequency identification (RFID) market. RFID tags are used for tracking items such as pharmaceuticals, clothing, autos and animals. If the cost of an RFID tag could be reduced to a low enough level, RFID tags could potentially replace bar codes on goods in a store. These tags, also known as electronic product codes (EPC), would allow for product tracking from the factory to the consumer. This could potentially reduce check out times, since goods could be scanned from a distance. One of the largest implementations of RFID in the marketplace was in 2005 when Wal-Mart required its top one hundred suppliers to tag pallets and cases of goods with RFID tags [51]. More recently, Wal-Mart and a number of other retailers have been tracking individual clothing garments to better track inventory and make sure shelves are stocked. The tags will also reduce any potential employee theft from backroom supplies [52]. These examples show the increasing demand for RFID tags and their potential market value in the future. However, the current RFID tags are too expensive for widespread market deployment. The hope is to use printed electronics to manufacture a RFID tag below one cent per tag.

RFID tags are a particularly interesting application for printed batteries. For wireless RFID tags, button and coin cells are often used. A traditional passive RFID tag relies completely on the transmitted signal to power the circuit and generate a response. A passive RFID system requires strong RF signals and close proximity of the RFID tag to the generator. An active RFID battery contains a battery that continuously powers the tag and RF communication circuitry. The active tag is able to read low intensity RF signals and generate high intensity. In between active and passive RFID tags are semi-passive tags. Typically, semi-passive tags use a battery for a chips standby operation but require transmitted RF energy from the reader to power the tag response. The power consumption when an RFID tag is active can be on the order of a few microamps [53]. This low current density doesn't necessarily demand a high power density battery. For example,

a passive UHF RFID (860 -960 MHz) tag with integrated temperature and photo sensor has been developed for a 0.25-µm CMOS process [54]. The demonstrated RFID tag requires only 5.14-µW during the active state with a current consumption of 700 nA at 1.5 V. The low power consumption allows for a ten year operation with a 100 mAH capacity battery [54].

Printed RFID tags are an emerging technology that has the potential to supplement the usage of silicon-based RFID tags by introducing a low cost alternative. The current cost of silicon-based RFID tags is a function of the cost of the silicon chip, the off-circuit antenna plus the cost of the antenna attachment [55]. The silicon chip (<0.5 mm a side) is typically a few cents while both the antenna and attachment cost a couple of cents. Printed RFID tags attempt to reduce the cost of RFID tags by eliminating the cost of the attachment. Areal requirements and cost will limit the number of transistors to a few thousand, which limits printed RFID tags to simple applications, such as read-only bar codes.

Printed RFID tags would benefit from printed batteries. In fact, high energy density, low cost printed batteries could potentially enable the deployment of semi-passive printed RFID tags. The use of low temperature processing materials such as printed thin-film transistors will require higher voltages (10 V to 30V) and higher power for operation due to the larger off current in these devices [56]. These high voltages can be met by printed batteries in series [49].

2.3 Printed and thin film batteries

2.3.1 Printed battery architectures

There are two main printed battery architectures: the planar cell and the vertical battery (Fig. 2.3). Printed batteries have been demonstrated using both architectures. There are advantages and disadvantages associated with both of these structures that affect their use in certain applications.

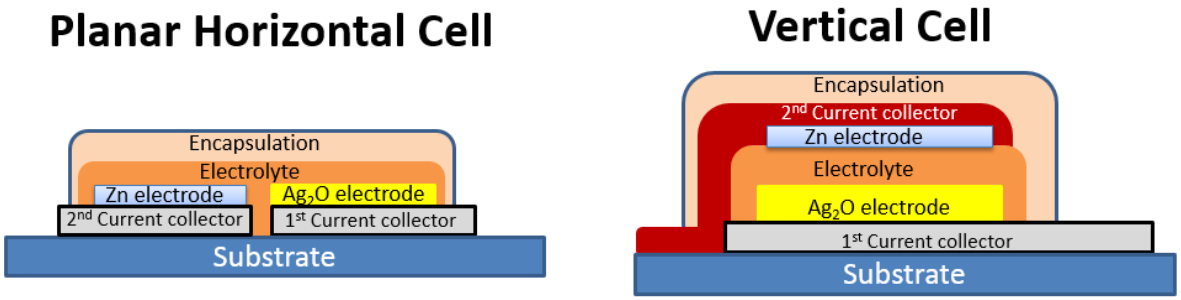

Figure 2.3 Cross section of the two main architectures, planar and vertical, used to fabricate a printed battery.

The horizontal structure has electrodes in the same plane with a separator or electrolyte connecting the tops of the electrodes. These cells typically suffer from high impedance due to the larger effective separation distance between the two electrodes. This leads to non-uniform current distributions which may be a problem for high discharge rates and in rechargeable batteries [57]. The energy density of the horizontal cell is also lower due to a larger fraction of

the electrolyte and encapsulating layer. The internal resistance can be reduced by making interdigitated electrodes, as demonstrated by other groups [58], [59].

The vertical cell, on the other hand, has the electrodes face-to-face. This is the ideal structure that minimizes the separator resistance and has a higher energy density due to the more compact volume. The parallel plate configuration of the vertical systems also allows for a more uniform current distribution, which can reduce filament formation in systems that form filaments upon recharge, such as Zn/MnO_2 and Zn/Ag_2O. Commercial batteries typically use the vertical architecture, like the li-ion technology that is a thin vertical stack that is rolled on itself after being laminated together.

The vertical structure is more difficult to achieve from a printing standpoint. Each layer has to be deposited upon the previous layer. This introduces a lot of complexity since there are five battery layers (six if the encapsulation layer is included). Each printing step has to be compatible with the previously deposited layer. The ink or slurry being printed should not dissolve the previously deposited layer. The deposited layers should be capable of withstanding the processing steps of the subsequent steps, whether that be annealing steps or chemical reactions. Layer uniformity is also important since a non-uniform bottom electrode can potentially protrude through the separator leading to a short in the battery.

Using these architectures, there are multiple different chemistries that can be developed into a printed battery, each having advantages and disadvantages in terms of chemistry and processing. These chemistries have been demonstrated in literature and in commercial products. Examples of literature and commercial batteries are discussed below after an introduction of the chemistry involved. We focus specifically on lithium-ion and alkaline based chemistries.

2.3.2 Lithium-ion batteries

The lithium-ion chemistry is an attractive chemistry that has found many uses in personal electronics and hybrid vehicles. The lithium-ion chemistry is used for many portable electronic applications due to its high energy density and high demonstrated cycle lifetime. The energy density of the lithium-ion chemistry is one of the highest available energy densities with demonstrated volumetric energy densities of 350 Wh l^{-1} and gravimetric energy densities of 150 Wh kg^{-1} [60]. The high energy density comes from the fact that lithium is one of the lightest elements (3rd lightest) on the periodic table and has one of the highest oxidation potentials (+3 vs SHE). As a result, the open circuit voltage of these batteries, which depends on the reduction potential of the half-cell equations, can have values that range from 2.5V to 4.2V [61].

Lithium-ion batteries are not only attractive for their high energy densities, but also for their high cycle lifetimes, with demonstrated cycles of 30,000 charge/discharge cycles at an acceptable discharge and recharge rate [62]. This corresponds to a ten year operational lifetime. A key focus in the Li-ion field is extending the high cycle lifetime for higher energy density batteries and at higher discharge rates. Ideally, a rechargeable battery would have a coulomb efficiency of 1, i.e.

$$CE = Q_d / Q_c = \text{charge in/charge out}$$

Side reactions, such as loss of lithium-ions due to SEI formation, electrode deterioration or electrolyte oxidation limit this number from being one [63].

The high cycle lifetime of the lithium ion chemistry is enabled by the intercalation mechanism by which charge is stored. In this process, the lithium-ion is inserted into the layered structure of the electrode material (Fig 2.4). Essentially, lithium is transferred to and from the positive and negative electrodes. During discharge, ions move from the negative electrodes, which is typically graphite or Li_xC_6, and inserted into the positive electrodes, which is typically $LiCoO_2$. The reverse reaction happens on recharge of the cell. The electrolyte consists of lithium salt in an organic solvent, usually a mixture of ethylene carbonate or diethyl carbonate. An organic solvent with a high electrochemical window has to be used; otherwise it would be oxidized due to the high potential found in the lithium-ion cell.

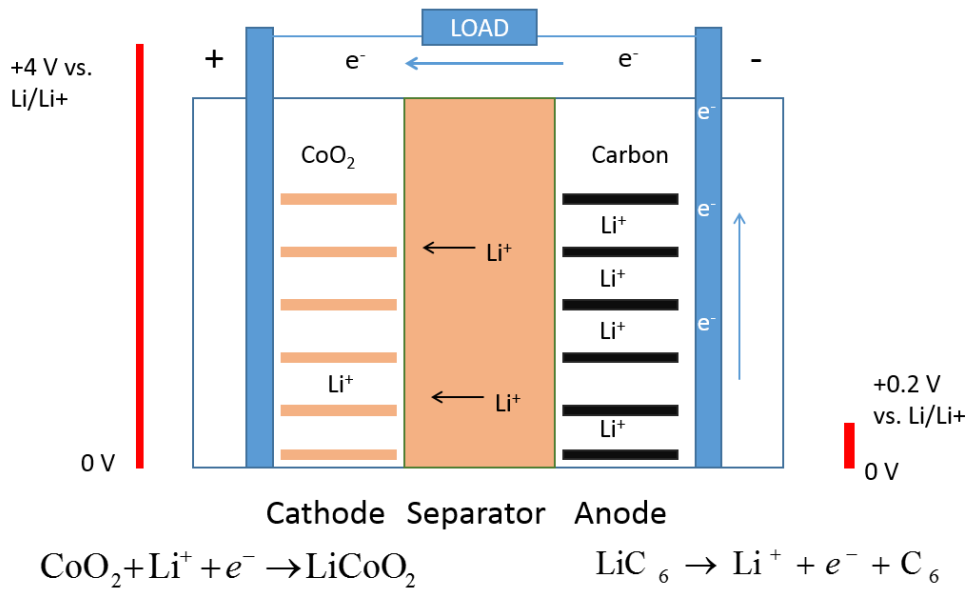

Figure 2.4. Cross section schematic of the lithium-ion chemistry during discharge. Chemistry is based on intercalation of the lithium-ion into the electrode material.

There are several disadvantages with the lithium-ion chemistry. One disadvantage of lithium-ion chemistry is sensitivity to contamination. Nonaqueous solutions with oxygen or water present will form the reduction products LiO_2, Li_2O_2 (for O2, 1.5-2 V vs. Li/Li^+) and LiOH (for H_20, 1.5-1.2 V vs. Li/Li^+) [64]. Lithium-ion batteries also suffer from a problem known as thermal runaway. Dangers of thermal runaway reactions are fire, burns and release of hydrogen fluoride from the electrolyte. Thermal runaway in batteries is avoided by monitoring each cell and the use of a self-clogging polyolefin separator [65].

Certain aspects of the lithium-ion battery fabrication process are not practical for the fabrication of a printed battery; one disadvantage is that the Li-ion chemistry is water sensitive and requires inert processing steps which add to the cost to the fabrication. In the typical lithium

ion battery, a lithium polymer battery is formed by laminating a lithium metal or a carbon anode, a lithium-ion conducting membrane, and a composite cathode with a metal current collector [66]. The cell is made as a continuous sheet, and then either rolled or folded depending on the final shape and application. The rolled battery is then inserted into a battery case. Introduction of an electrolyte/solvent mixture typically requires a dehydration step to remove water from the fabricated stack and a vacuum step to remove any oxygen and residual water. This step is followed by the introduction of the electrolyte/solvent to the evacuated lithium-ion stack. The electrolyte/solvent fills the pores of the electrodes and separator. Annealing and vacuum steps are not practical or cost-effective for the production of large scale microbatteries.

Despite the widespread use of lithium-ion batteries, there are only a few demonstrations of printed lithium-ion batteries. These systems include partially and fully printed batteries, both in literature and commercial batteries. One thing to note about these examples is that they require hermetic packaging to remove exposure to oxygen and water.

A spray painted lithium-ion battery has been demonstrated to have energy densities of 6 Wh/m^2 [67]. The fabrication of this battery consists of spray painting a cathode which consists of a single walled carbon nanotube and lithiated cobalt oxide ($LiCoO_2$ or LCO), a separator layer consisting of Kynarflex and poly(methylmethacrylate) PMMA and fumed SiO_2 , and finally, a negative electrode consisting of lithium titanium oxide ($Li_4Ti_5O_{12}$ or LTO) with a copper paint current collector. This technique demonstrates promise for a printed battery system. However, it still suffers from being a water and air sensitive chemistry. After fabrication, the battery was transferred to an argon glovebox to be saturated for two hours with the lithium salt electrolyte. This chemistry also requires hermetically sealed packaging. Despite these limitations, the spray painted battery does have the potential to be deposited over large areas on any arbitrary surface.

A 3D printed lithium-ion battery has also been demonstrated using extrusion printing [58]. Here, interdigitated electrodes consisting of $Li_4Ti_5O_{12}$ (LTO) and $LiFePO_4$ (LFP) are extrusion printed on to gold current collectors for the anode and cathode materials, respectively. The demonstrated areal energy density was 9.7 J cm^{-2} and the power density was 2.7 mW cm^{-2}. The li-ion microbattery was packaged using a laser cut PMMA preform to encircle the cell. The preform is sealed to the substrate with PDMS. After the introduction of the electrolyte, a glass slide is placed on top and sealed with PDMS. This encapsulation scheme is not ideal and will not be a hermetic seal that enables long-term use. This demonstration illustrates a 3-D printing technique use to fabricate a lithium-ion battery with a unique structural configuration.

The structure of commercial batteries are typically simpler than their printed counterparts. The prototypical lithium ion battery consists of a negative electrode (anode on discharge) that is typically graphite and a positive electrode (cathode on discharge) that consists of a lithiated transition metal oxide (common metals are cobalt, nickel or manganese). The electrolyte consists of an ethylene carbonate and $LiPF_6$ ($LiBF_4$)-based electrolyte. The cathode and anode materials are typically deposited as inks that are printed on a current collector. These electrodes are then calendared to get a uniform thickness. Then, the electrode layers are laminated together with a polymer separator layer. Although the fabrication process for commercial batteries uses printing to deposit the electrode layers, no completely printed

commercial lithium-ion battery exists. One company, Solicore, has a partially printed microbattery available on the market.

Solicore has announced the development of a printed, ultra-thin, flexible lithium polymer battery [68]. The company is capable of both screen printing and digitally printing lithium-ion batteries. Their product line of batteries is primarily batteries designed for single use applications. The *Flexion* line of batteries that they manufacture is designed for powered cards, RFID and micro medical devices with capacities of 10-25 mAh or customizable capacities based on the application [25]. For example, one of their *Flexion* batteries has a capacity of 25 mAh, an open circuit voltage of 3.0 V, a thickness of 450 um and an area of 49 x 23 mm^2. The Solicore thin film batteries illustrate the market for a fully printed battery exists and demonstrate that lithium-ion chemistries can be printed at a competitive cost to produce microbatteries. However, note that all of these batteries require careful encapsulation, and therefore, suffer from degraded overall effective energy density, particularly when the batteries are reduced in size; in small batteries, encapsulation is an increased fraction of the overall battery mass and volume.

2.3.3 Alkaline batteries: Zn-MnO_2 printed batteries

Alkaline batteries are based on a chemistry that utilizes a hydroxide ion, OH^-. These chemistries use KOH or NaOH as the electrolyte. The hydroxide ion is an active participant in the reaction. During discharge, there is an equal amount of OH^- consumed and produced. Common alkaline chemistries include Zn/MnO_2 and Zn/Ag_2O. The basic environments in these batteries typically have a pH~14.

The half-cell reactions associated with the Zn/MnO_2 chemistry are:

$$\mathrm{Zn} + 2\mathrm{OH}^- \leftrightarrows \mathrm{ZnO} + \mathrm{H_2O} + 2\mathrm{e}^-, \qquad U = 1.28\,V$$

$$\mathrm{Mn}O_2 + H_2\mathrm{O} + 2e^- \leftrightarrows \mathrm{MnOOH} + OH^- \qquad U = 0.15\,V$$

During discharge, the lattice of MnO_2 accepts electrons and protons which are capable of moving through the MnO_2 lattice. During this process, the MnO_2 is reduced to MnOOH. This reaction is a one phase reaction as the MnO_2 matrix remains [69]. As a result of this one phase reaction, the open circuit voltage decreases with depth of discharge. This is a disadvantage with this chemistry since a constant voltage is desired for the circuit. Circuit applications using Zn/MnO_2 need to take into account the sloping open circuit voltage (and thus closed circuit voltage) that occurs with increasing discharge time.

Fully printed batteries based on the Zn-MnO_2 chemistry have not been fully developed. Printed Zn-MnO_2 batteries using a nylon mesh support to provide mechanical support have demonstrated current densities of 5.6 mAh cm^{-2} at discharge rates of 0.5 mA [28]. This fabricated battery relies on partially printed battery layers and requires assembly after deposition. The separator is formed by saturating a mesh with polyacrylic acid that has been saturated with KOH. The piecewise assembly is not ideal for a large scale fabrication process, and the meshes add to the mass and volume as inactive components, thus reducing volumetric and gravimetric energy density.

Commercial partially printed Zn/MnO_2 batteries are available for purchase; however, these are typically based on the carbon zinc chemistry [70]. One such example is from the company Blue Spark, which has a printed planar Zn/MnO_2 battery. In this battery, a zinc foil is laminated on to a plastic substrate. Next to the zinc foil, a carbon based collector is printed, followed by the printing of the MnO_2 electrode. A "paper" separator layer is placed on top of the electrodes to retain the electrolyte. A mulit-ply encapsulating layer is adhered to the substrate with a pressure sensitive, heat activated adhesive. This commercial battery is designed for low drain applications, as the planar architecture is not ideal for a low internal resistance battery.

2.3.4 Alkaline batteries: Silver-zinc chemistry

A related alkaline chemistry is the Zn/Ag_2O chemistry, where Ag_2O is used to make the positive electrode. The silver-zinc chemistry is an alkaline chemistry known for its high power and high energy density chemistry [71]. The high energy density results from the fact that zinc is the most electropositive metal that is compatible with aqueous solutions. It has a high hydrogen overpotential and a negative electrode potential ($Zn^{2+} + 2e^- \rightarrow Zn$ E=-0.76V vs. SHE). Primary silver-zinc batteries have found applications as primary batteries in the Apollo satellites and hearing aids due to their high energy density. For hearing aids, the current draw is low, with hearing aids drawing currents on the order of a few hundred microamperes, with power levels less than 500 µW [72]. The typical properties of a silver-zinc button cell (SR 44 IEC reference) from VARTA Microbattery GmbH are a 1.55V voltage, 175 mAH capacity, an internal resistance of 3-5 Ω for a 11.6 mm diameter, 5.4 mm height and a weight of 2.4 g.

A cross section of a silver-zinc system is shown in Figure 2.5. The silver oxide layer is separated from the zinc layer with a separator layer. The separator allows transport of water and potassium and hydroxide ions through the holes of the porous separator layer. This layer should have high ionic conductivity and prevent the battery from shorting.

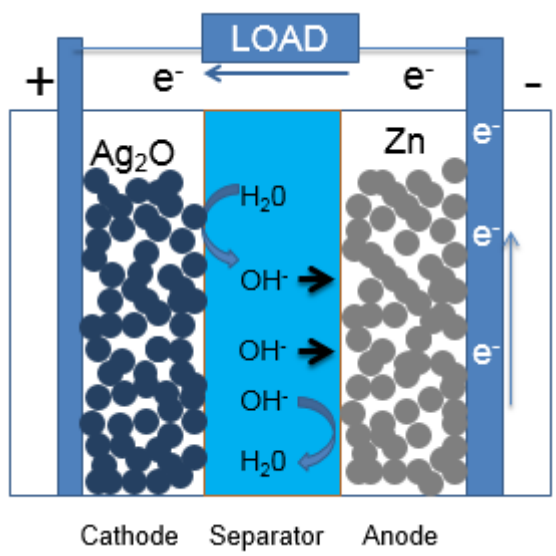

Figure 2.5. Cross section of silver-zinc battery with porous electrodes during discharge.

The chemistry of the silver-zinc systems is based on the reduction of silver oxide and the oxidation of zinc. There are two possible chemical reactions that can occur at the cathode

depending on the chemical species of silver oxide present. The chemical reactions that occur at the cathode for bivalent AgO and monovalent Ag_2O are:

$$2\mathrm{AgO} + \mathrm{H_2 0} + 2\mathrm{e}^- \leftrightarrows \mathrm{Ag_2O} + 2\mathrm{OH}^-, \quad E^0 = +0.607\ V$$

$$\mathrm{Ag_2O} + \mathrm{H_2 0} + 2\mathrm{e}^- \leftrightarrows 2\mathrm{Ag} + 2\mathrm{OH}^-, \quad E^0 = +0.345\ V$$

The traditional silver-zinc battery consists of a chemically prepared pressed powder silver oxide electrode or an electroformed silver oxide electrode. The sintered silver powder electrode consists of sintering a silver oxide pasted layer at 500˚C to form a porous silver grid, followed by electroforming the grid to monovalent (Ag_2O) or divalent oxide (AgO) at low discharge rates in a KOH solution. The monovalent silver oxide (AgO) provides for higher energy densities and a greater operating voltage. However, monovalent silver oxide is thermodynamically unstable (decomposition temperature of 220°C) and is converted to silver over time. There is also a significant difference between the resistivity between the two species, with AgO (ρ = 14 ohm cm) being significantly more conductive than Ag_2O (ρ = 10^8 ohm cm) [73]. In pressed powder electrodes, monovalent silver oxide is used with the addition of conductive additives, such as 1-5 wt% graphite [74]. Some silver oxide electrodes are treated with the reducing agent, such as hydrazine, to produce a thin layer of silver across the pellet to provide good contact with the cathode terminal [75].

At the anode, the zinc electrode is oxidized by a dissolution and precipitation reaction which proceeds by

$$\mathrm{Zn} + 4\mathrm{OH}^- \leftrightarrows \mathrm{Zn(OH)_4^{2-}} + 2\mathrm{e}^-, \quad E^0 = -1.249$$

$$\mathrm{Zn(OH)_4^{2-}} \leftrightarrows \mathrm{ZnO} + H_2\mathrm{O} + 2\mathrm{OH}^-$$

As the zinc is oxidized to zincate, it goes into a solution where it diffuses and drifts throughout the battery. Once the solid solubility limit is reached for a given solution volume, the zincate will precipitate out to zinc oxide. This precipitation mechanism can occur throughout the cell. At high rates of discharge, this can potentially lead to pore clogging in the zinc electrode or separator.

The sum of the two half reactions for monovalent silver oxide and zinc gives the entire reaction:

$$\mathrm{Ag_2O} + Zn \leftrightarrows 2\mathrm{Ag} + \mathrm{ZnO}$$

The open circuit potential of the entire battery is 1.60 V. Typical batteries will have open circuit voltages between 1.55 and 1.60 V depending on the hydroxide ion concentration and the state of the zinc/electrolyte interface. The number of hydroxide ions does not change during the discharge reaction. The water and hydroxide ions are transported through the separator layer by drift and diffusion during the discharge reaction.

The transport of these ions is mediated by the separator layer. The separator layer of a silver oxide battery is typically divided into three regions: the layer near the silver oxide, the middle layer and the layer next to the zinc electrode. One separator layer would be ideal;

however, due to constraints imposed by the chemistry of the silver-zinc battery, multiple layers are typically needed.

Adjacent to the silver electrode is a spacer layer that consists of a chemically inert material that maintains the electrolyte next to the silver oxide electrode and simultaneously prevents the middle separator layer from touching the highly oxidizing silver oxide. The middle separator layer serves two functions. One is to prevent the growth of zinc dendrites from the zinc electrode reaching the silver oxide electrode on recharge and shorting the battery. The second is to prevent soluble silver species from reaching the zinc anode. The next layer is a zinc spacer layer that maintains the electrolyte near the zinc electrode. The silver spacer layer consists of nonwoven fabric such as nylon or polypropylene. This layer ideally should be able wet to provide electrolyte to the silver electrode.

The middle separator should have high ionic conductivity, but at the same time be stable enough to prevent zinc dendrites from forming and prevent soluble silver species from reaching the zinc electrode. The separator layer should impede the diffusion of soluble silver species. The diffusion of silver species, such as $Ag(OH)_2^-$, causes a reduction in capacity upon reaching the zinc anode due to a reduction of the silver oxide species and oxidation of the zinc. The loss of the soluble silver oxide species allows for more sliver oxide to be solubilized, which can in turn, be reduced once it reaches the zinc electrode. This process will lead to a steady decrease in capacity over time and potentially shorts in the cell. The process is slow due to the fact that the solubility of silver oxide is low.

The separator material that has typically been used is cellophane which is a cellulosic material. Cellophane is formed from regenerated cellulose. Cellulose is dissolved in an alkaline bath with carbon sulfide to form a solution called viscose. Viscose is then extruded into the desired shape and then, into a sulfuric acid and sodium sulfate bath to convert the viscose back into cellulose. The cellulose is passed through further baths to remove any remaining unconverted cellulose. The results sheets are layered or wrapped on the electrodes of the silver-zinc battery. The cellophane offers relatively good ionic conductivities for potassium hydroxide due to the presence of the hydroxyl groups on the glucose units and the β(1-4) glycosidic bond between the glucose units. The stability of the cellophane in an alkaline environment depends on the concentration of the hydroxide ions.

It is not conceivable to regenerate cellulose directly on an electrode in a printed manner. The presence of an acidic solution on zinc will result in an oxidation of the zinc metal and the formation of hydrogen gas. At the silver oxide electrode, the soluble silver species will form along the formation of water. This means a printed separator requires the development of new materials and processes.

Silver-zinc batteries are usually found as single use or primary batteries. Silver-zinc batteries can be recharged, but there are several difficulties associated with the recharging process. One problem is the formation of a non-adherent mossy form of zinc which forms during recharge and results in a loss of capacity [76]. A second problem is the formation of zinc dendrites

that can short through the separator [77]. This limits the useful cycle lifetime to 50-100 cycles before failure.

Besides the commercial silver oxide cells that can be purchased in small button cells, there have been a couple of demonstrations of thin film or printed silver oxide batteries. Ho et al. have demonstrated a printed silver oxide zinc battery by printing silver pillars on silver electrodes followed by electroplating zincate onto one of the electrodes and oxidizing the other silver pillars and pad [78]. They print the electrodes and use electroplating to charge the battery. The geometry is not ideal; however, this work shows an interesting use of extrusion printing to form 3D pillars to increase surface area for a Zn/Ag_2O battery.

A second example is a laser direct-write zinc-silver oxide alkaline battery [79]. This technique uses a laser to transfer ink from an ink coated glass slide that is 100 µm from the surface of the substrate. The laser causes a transfer of the ink to the substrate by local evaporation of material on the glass slide. Using this technique, Arnold et al. have demonstrated a 450 $\mu A\ h\ cm^{-2}$ planar microbattery. Although this capacity is low, it demonstrates a potential low capacity thin film battery.

These examples illustrate some of the approaches taken to achieve a thin printed zinc-silver oxide battery. Despite these examples, there is still a lot of work needed to occur in order to develop a fully printed, high energy density zinc-silver oxide battery.

2.4 Advantages and disadvantages of silver oxide batteries for printed electronics

There are several reasons why zinc-silver oxide chemistry would be chosen over other battery chemistries, such as lithium-ion and alkaline Zn/MnO_2, for development of a printed battery for printed electronics.

One advantage of the Zn/Ag_2O chemistry is that it is an aqueous chemistry. This chemistry is inherently not water sensitive as compared to the water sensitive chemistry of Li-ion. This means the processing steps used to fabricate an alkaline battery are not as stringent, such as requiring the use of an inert atmosphere for electrolyte processing. This is attractive for making a low cost fabrication process. Oxygen is still an issue due to the oxidation of the zinc electrode. However, this can be overcome by degassing the alkaline electrolyte. Furthermore, the use of an aqueous chemistry will likely reduce the packaging requirements. Complete hermetic packaging may not be necessary for a Zn/Ag_2O battery depending on the desired lifetime of the battery.

A second advantage of the Zn/Ag_2O chemistry is the high energy density. This is due to a combination of the high, flat closed circuit potential near 1.5-1.6 V and the large columbic capacity of the electrodes. The high potential is due to the high ionic conductivity and the low activation polarization. The flat, steady potential is due to the two phase reduction of the zinc and silver oxide electrodes [69]. The energy density of this chemistry is slightly lower but still comparable to the energy density of lithium-ion chemistry. The high ionic conductivity and low activation polarization also enable the chemistry to have a high power density as seen by the Ragone plot (Figure 1.1).

For the reasons listed above, we have chosen to fabricate a zinc-silver oxide, printed battery. This high energy density and potentially air stable chemistry are ideal for developing a low cost, air stable process compatible with printed electronics applications.

2.4.1 Cost analysis of the Zn-Ag_2O battery

We can estimate the cost of the material components for a silver oxide-zinc battery to get an idea of the cost range for a printed battery. Silver is a precious metal with a cost of $19.65 a ounce [80]. At smaller battery sizes, the cost of the inactive material components and the processing costs become a larger fraction of the total battery cost. In this regime, the cost of the silver oxide will be a small fraction of the cost.

For this cost calculation, we look at the major components of the system which consist of the silver oxide electrode, the silver current collector, the zinc electrode and potassium hydroxide. For example, suppose we want a 5x5 mm^2, 1 mAh capacity battery. This corresponds to a capacity density of 4 mAh cm^{-2}, which is a demonstrated capacity in this work. For an ideally matched battery with equal electrode capacities, we can calculate the resulting thicknesses and mass of the electrodes. We assume the zinc and silver oxide electrodes have both porosities of 20% (i.e. 80% is active material). The silver current collector is assumed to be a thickness of 20 um. This cost could be reduced by decreasing the thickness or changing the material used for the current collector. Based on this calculation, the cost for the active components of the 1 mAh battery will be 1.6¢ (Table 2.2).

Component	Thickness (µm)	Material	Mass (mg)	Cost per gram (¢)	Total cost (¢)
Silver oxide electrode	112	Silver	16.1	64	1.03
Zinc electrode	34	Zinc	4.9	0.04	0.00019
Silver current collector	2x20=40	Silver	9.3	64	0.60
Potassium hydroxide	NA	KOH	5	0.003	0.000015

Table 2.2. Material components and costs for a silver oxide-zinc battery. Prices are determined from market value prices in April 2014.

This cost only looks at the active material components of the cell. Other parts of the battery including processing and labor costs will increase the amount, but that will be determined by the process used to fabricate the batteries and the total number of batteries produced. However, this calculation gives a lower limit in calculating the cost of a printed battery.

Although we are using silver oxide (Ag_2O) which is a more expensive electrode material than MnO2, the total cost of a small battery is likely going to be dominated by the processing costs. For this reason, Zn/Ag_2O is an appropriate choice for developing a printed battery. However, we note that if the cost is too high for a particular application or capacity, then, the positive electrode material could potentially be replaced with a lower costing component such

as MnO_2 with minor changes to the battery structure. The separator developed in this thesis for a Zn/Ag_2O battery should be compatible with a Zn/MnO_2 battery.

We examine how this cost will affect a particular printed application, RFID. An example where printed batteries may have use, is the incorporation of a battery with a printed RFID tag, to form a battery assisted passive RFID tag. Ideally, printed RFID tags should be as inexpensive as possible. To apply tags to all goods, the cost of an RFID tag applied to all goods should be less than a cent [42]. The addition of 1 mAh which costs a minimum of 1.6¢ would push the cost over what is necessary for the wide spread use of RFID. This means a smaller capacity would be needed or the battery assisted RFID tag would be used only for applications that warranted the cost. A 1mAh battery that only cost a couple of cents is still likely to find many new applications in the field of printed electronics and small form factor applications.

2.5 Discharge characteristics

We have characterized the printed silver oxide batteries by looking at the discharge characteristics. In the typical battery, we discharge at a fixed current and record the battery potential. The printed batteries are typically discharged at a fixed rate of C/2. The C/X rate is defined as the discharge rate in amperes or A cm^{-2} required to use the entire capacity in X hours. For example, a C/2 discharge rate means that in two hours, the total capacity will be used up. We have kept the experimental conditions constant by discharging at a C/2 rate. The capacity of the battery is determined by the capacity of the limiting electrode. For example, in a silver oxide limited battery, we discharge with respect to the silver oxide capacity. For example, in the situation where we have a silver oxide electrode with capacity of 10 mAh and a zinc electrode with 40 mAh, the silver oxide electrode is the limiting electrode.

We analyze the performance of the fabricated batteries in terms of several metrics: open circuit voltage and internal resistance. The open circuit voltage is determined by the potential of the battery under effectively no load conditions. Another parameter of interest is the percent utilization. In particular, since we always work with silver-limited cells (i.e., the cells have an excess of zinc; this is done since silver is the most expensive component and will almost certainly be limited in real applications), we focus on silver utilization. We define the percent of silver oxide (or percent of zinc) utilized by the following equation:

$$\%\ Utilization = \frac{discharged\ capacity}{expected\ capacity} = \frac{i_{dis} \times t}{m \times M_w \times n \times e},$$

where i_{dis} is the discharge current, t is the total time, m is the mass of the active material in the limiting electrode, M_w is the molecular weight of the limiting active material, and e is elementary charge. The expected capacity is determined from measuring the mass of the limiting reagent. For the fabricated batteries, this is typically 10 mg. Variations in the printing process will introduce sample–to-sample variation; however, we measure that variation by measuring the mass of the dried electrode to calculate the percentage of the active material in the electrode. We use this measurement to calculate the expected capacity in the limiting electrode. By comparing the charge, we were able to extract the expected charge available, and then, we calculated the percentage of the limiting electrode utilized. This assumes we are limited by the

electrode with the limited capacity. An example of a planar printed battery is shown in Figure 2.6 which shows the discharge potential as a function of the percentage of silver oxide utilized during a discharge at constant C/2 discharge rate. In this case, we see that the fabricated battery was able to achieve utilizations of 70-80% before a cut-off voltage of 0.6 V is reached. The results of the discharged batteries in Figure 2.6 will be discussed further in Chapter 3.

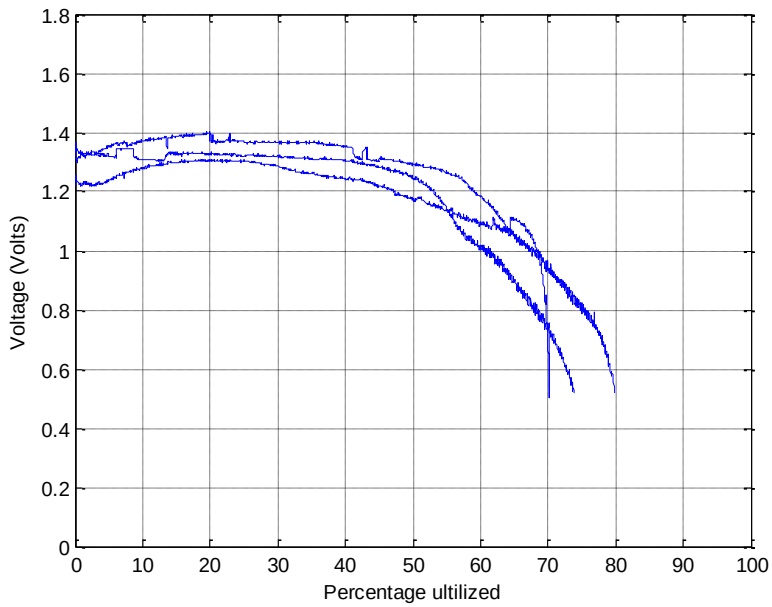

Figure 2.6 Discharge characteristics of an exemplary silver oxide limited cell; a printed planar battery discharged at a rate of C/2 with a 2% PVDF polymer binder repeated in triplicate

We also have characterized the internal resistance using the following definition:

$$R_{internal} = \frac{V_{OCV} - V_{CCV}}{i_{dis}},$$

where V_{OCV} is the open circuit voltage, and V_{CCV} is the closed circuit voltage or the voltage during discharge after the potential has stabilized. We use the V_{CCV} after an initial five minutes of discharge and take the average value for 1 minute of discharge. This measurement contains multiple potential drops, including ohmic resistance, surface overpotential and concentration overpotential [29]. These voltage drops will be dependent on the current density; however, by discharging at a constant rate, the potential drops should be kept constant. This assumes that the parameter varied during fabrication doesn't change the battery structure, in which case, we would see a change in the internal resistance. More detailed characterization of the resistances will be performed in Chapter 5, where we use electrochemical impedance spectroscopy (EIS) to characterize the battery structure.

Using the metrics of internal resistance and percent utilized allows us to examine the effect of changing different parameters of the printed silver oxide battery. This allows us to quantify the effect of the changes.

2.6 Conclusion

Various aspects of printed batteries were discussed in this chapter. We examine the different printing techniques used in printed electronics and found that stencil printing, screen printing, and extrusion printing are suitable for printing the thick films required for a printed battery. We examine various battery chemistries and their examples in literature and in the commercial marketplace. After comparing their advantages and disadvantages of each chemistry, we found that the advantages of the zinc-silver oxide chemistry are particularly attractive for developing a printed battery. The zinc-silver oxide has the advantage of having a high energy density, a high power density, and has an air stable chemistry that doesn't require special vacuum processing steps like lithium ion technologies. For these reasons, we have decide to use this chemistry in a printed battery. We have demonstrated this chemistry both in a planar architecture (Chapter 3) and a vertical architecture (Chapter 4).

Chapter 3. Planar printed battery

A planar printed battery requires the development of printed current collectors, printed electrodes and a printed separator. We have developed a printed silver oxide battery using the planar architecture where the battery electrodes are printed side-by-side. This reduces the physical requirements of the separator layer and printed electrode layers. This allows for developing a separator that has less stringent requirements. Specifically, the separator doesn't have to support the subsequent electrode and current collector printing steps. We also do not worry about the compatibility of the electrode ink with the separator layer because we deposit the two electrodes directly onto the planar current collectors. We can also print the same current collector material for both electrodes in the planar architecture which reduces the complexity of the material systems that we have to develop.

We fabricate the printed, planar silver oxide battery using extrusion printing to deposit the separator and electrode components (Fig 3.1). The extrusion printer consists of three-axis stage that is controlled with a Newmark Systems MSC-M four stage controller with a 1 um resolution. The ink is dispensed from pneumatically controlled dispensing syringe head using a Musasahi ML-808FX pneumatic controller. This setup is capable of printing feature sizes down to 50 µm and thickness of 10 to 200 µm depending of the ink rheology, syringe needle size, shot pressure, and drop spacing [44].

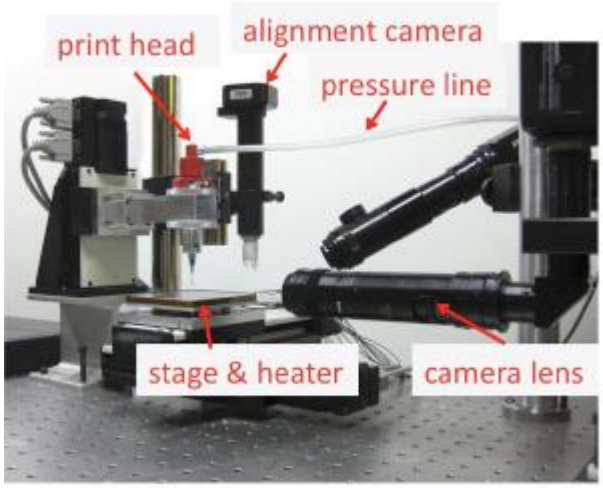

Figure 3.1 Custom built extrusion printer used to deposit electrode and polymer solutions [26].

We focus on the development of the formulation of a printed separator and silver oxide and zinc electrodes. We extrusion printed zinc slurries for the zinc electrode, silver oxide slurries for the silver oxide electrode, and polymer solutions for the separator layer [47]. For the electrode materials, the slurry solutions consist of a solvent, a polymer binder that is soluble in the solution, active material particles (zinc and silver oxide) that are on the order of 1-10 µms and a conductive filler. The separator/electrolyte system is deposited in a two-step process where, first, the polymer is deposited, followed by the activation of the separator with a KOH

electrolyte. Using these techniques, we have demonstrated a high energy density printed battery with the planar architecture.

3.1 Current collector

An ideal current collector for an alkaline battery should demonstrate a low resistivity and be chemically stable at a high pH. A low resistivity material enables the current collector to be thin and flexible. The reduced mass and volume of the current collector enables a higher volumetric and specific energy density, a desired characteristic for a printed battery.

For development purposes, we have used an evaporated metal layer on glass slides as the current collector and substrate, respectively. To simplify our systems and focus on the development of the printed electrodes and separator materials, we have chosen to use metal evaporation to deposit the current collector. Printing of metal nanoparticle inks or precursor metallic inks are a potential printed replacement for the evaporated metal current collector [81].

We evaporated a thin layer of gold for the current collector due to its inertness to corrosion. To obtain adhesion of the evaporated gold to the glass substrate, we have used a thin evaporated chrome layer of 2nm. The evaporated gold layer was 80-100 nm in thickness. The evaporated layer exhibits high conductivity and is within an order of magnitude of the bulk conductivity level of 2.44×10^{-8} Ω-cm, determined by four point probe measurements. The gold pads were separated by 1 mm wide by a Kapton tape masking layer (Fig. 3.2). This is not an ideal separation distance, but for process development, the wide distance prevents shortening and allows for the placement of a zinc reference electrode between the electrodes which is useful to perform 3-electrode measurements (Section 3.6).

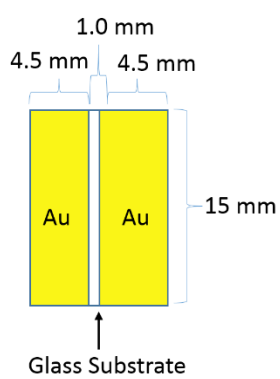

Figure 3.2 Evaporated gold current collectors contacts for printed planar architecture.

3.2 Printed alkaline separator

An alkaline printed battery requires the development of a separator layer that demonstrates high ionic conductivity and chemical inertness to alkaline environment. This layer also has to be printable to allow for easy integration into an all-printed process flow.

3.2.1 Ideal properties of an alkaline separator

The separator layer of an alkaline battery allows ions and water to be transported through the separator material. An alkaline separator should be capable of having high ionic conductivity,

good mechanical stability and be chemically inert. For rechargeable applications, it should resist zinc dendrite formation. The separator should be as thin as possible and still maintain good mechanical properties, such as resistance to rupture. A thin separator also allows for a higher energy density.

Commercial batteries typically use porous sheets of polypropylene that have been functionalized (Celgard) or cellophane (regenerated methylcellose). The sheets are laminated to the electrodes before insertion into the battery case. Sheets of alkaline separators can be purchased to be used in the assembly of alkaline based chemistries. Commercial separators based on cellulose and polypropylenes are available [82], [83]. These separators have been optimized to have high ionic conductivity, be mechanically robust and thin. The separator material can be purchased in rolls of various widths. These separator layers are not capable of being printed; thus we require the development of a printable layer that can have high ionic conductivity, be chemically inert, and have good mechanical properties.

However, for the demonstration of a printed battery, the requirements could be reduced. This is case for a planar battery; as the requirements of puncture strength and mechanical stability will be reduced since the electrodes are printed side by side and rupture of the separator will not result in shorting of the battery. From this viewpoint the planar battery is a good test structure to identify possible candidates for a printed separator layer.

3.2.2 Printed alkaline separators

A printed separator introduces a new requirement for alkaline separator development; namely, the separator has to be capable of being printed directly on top of the electrodes with minimal process steps. It is common in the printed battery field to assemble the battery after printing the electrodes. The separator layer in this case is not printed or a commercial separator. This has been done in the partially printed batteries using Zn/Mn_2O [84], [28]. Ghiurcan et al. has used electrolyte-wetted separator paper (Nippon Kodoshi Corp., VLZ 105). The separator paper was cut to extend beyond the cell, and the excess paper was submerged in electrolyte [84]. This process is not ideal for a commercially fabricated battery. Ideally, one would like a fully printed alkaline separator.

Polymers are an ideal choice for developing a printed separator because they can be dissolved in solutions, modified to contain different functional groups and synthesized to certain lengths. The difficult thing is to imbue mechanical stability into these polymer based printed separators after deposition. We want to be able to print the separator layer but have the separator layer be stable for further processing.

There have been many demonstrations of polymer based separators for use in alkaline batteries. Three common polymers used are polyethylene oxide, polyvinyl alcohol and methylcellulose (Fig. 3.3). Polyethylene oxide based separators have demonstrated ionic conductivities on the order of 10^{-3} S cm^{-1} [85] . Polyvinyl alcohol and poly(epichlorohydrin) films have been prepared for zinc-air batteries with demonstrated conductivities of 4 x10^{-3} S cm^{-1} [86]. Chemically crosslinked films of PVA with aldehyde have also been demonstrated with volume conductivities of 0.1 S cm^{-1}, which compare well to the commercial Celgard separator 3401 which

has a volume conductivity of 0.03 S cm^{-1} [87]. These separator deposition techniques require casting steps followed by temperature steps to remove the solvent used to solubilize the polymer or additional chemicals. For example, the PVA-aldehyde separator is treated with acid to induce the polymerization of polymer chains [88]. These steps are fairly harsh and are not suitable for direct incorporation into a printed battery process flow.

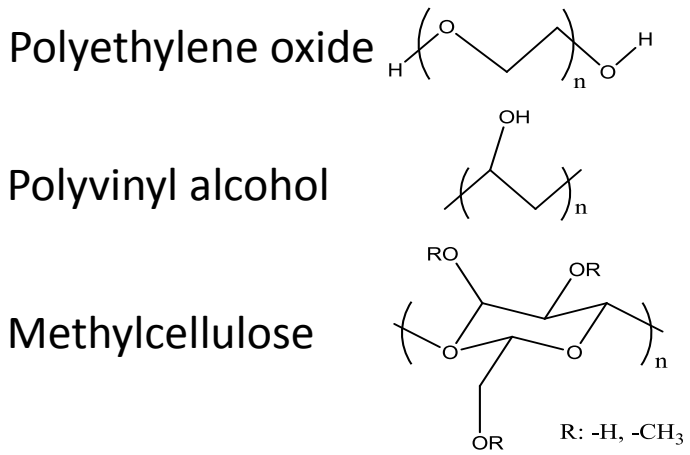

Figure 3.3 Printable water soluble polymers used in alkaline batteries: polyethylene oxide, polyvinyl alcohol and methylcellulose.

Ideally, we would like to be able to print the separator material and then, do a post-deposition step to improve the mechanical stability of the separator. This post-deposition could be a drying step, a chemical reaction or an addition of a second layer. We have chosen to use ionic crosslinking as the post-deposition step. Ionic crosslinking is based on the interaction of the polymer chains with ions introduced to the polymer gel solution. The common ionic crosslinking scheme is the ionic crosslinking of polyvinyl alcohol with sodium tetraborate to make slime (Fig. 3.4) [89]. Ionic crosslinking is reversible and can be broken by pH, solvent, ionic strength and concentration of the cross linker.

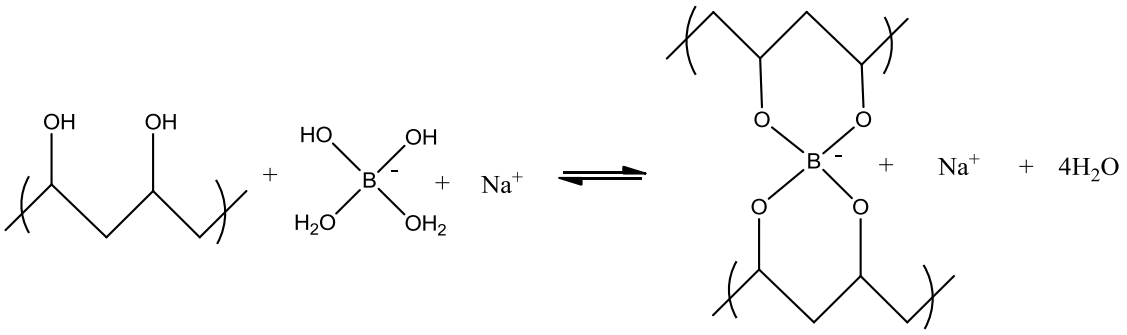

Figure 3.4. Ionic crosslinking of polyvinyl alcohol using sodium tetraborate.

We have used the same principle to form a separator layer for a printed battery. Specifically, we deposit a polymer solution that contains the polymer of interest (polyethylene oxide or methylcellulose), and then, we add an aqueous solution of KOH to crosslink the polymer chains. For example, using polyethylene oxide and KOH, we get an ion-dipole interaction

between the charged potassium ion and the oxygen groups of the PEO polymer chain (Fig. 3.5). This separator layer will have moderate mechanical stability due to the ionic crosslinking and contain the potassium hydroxide salt necessary for ionic conduction in the alkaline battery. The mechanical strength will be sufficient for a planar battery where the electrodes are printed side-by-side.

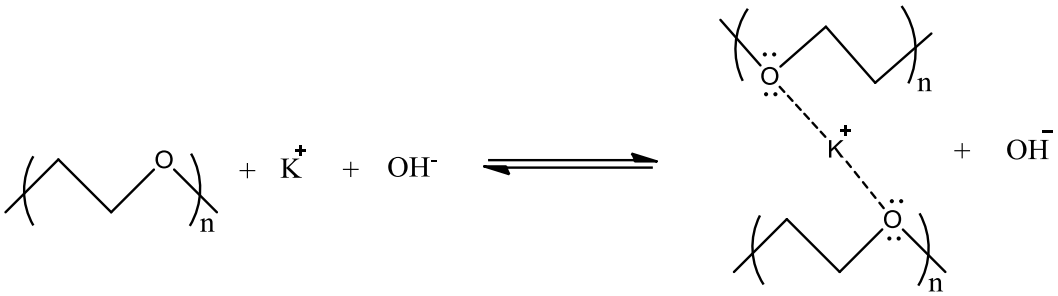

Figure 3.5 Crosslinking scheme using the KOH salt as a crosslinking agent.

Although polyethylene oxide, polyvinyl alcohol and methylcellulose have been demonstrated in alkaline batteries before and are possible candidates for ionic crosslinking, there are additional considerations that need to be taken into account in order for them to be used as a separator material for other alkaline chemistries, such as Zn/Ag_2O. The ideal separator should not react with the alkaline electrolyte or electrode materials. Polymers containing an alcohol group are a potential problem in the presence of oxidizers since they can be oxidized to ketones. This is a problem for silver oxide based chemistries because silver oxide is a mild oxidizing agent.

To examine this effect, we have prepared an aqueous slurry that would produce a 5wt% PVA binder and a 95wt% silver oxide electrode. After extrusion printing and annealing the silver oxide electrode for 5 minutes at 40C, we have placed the electrode in a 1 M NaOH solution for five minutes (Fig. 3.6). In this time frame, the surface of the electrode changes from a black color associated with Ag_2O to a yellowish color associated with the formation of silver. This color change is suggestive of a reduction of the silver oxide to silver.

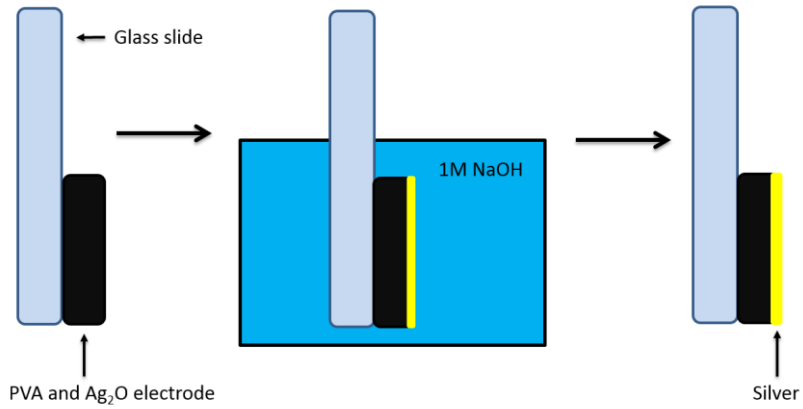

Figure 3.6 Experimental setup to determine stability of polyvinyl alcohol polymer in the presence of silver oxide in an alkaline environment consisting of NaOH.

Further evidence for the electrode change comes from X-ray photoelectron spectroscopy (XPS). If we look at the C_{1s} carbon peak in the before (Fig 3.7 A.) and after (Fig 3.7. B.) test conditions, we see a shift of the C_{1s} peak from 286.0 eV to a higher binding energy of 288.3 eV. This shift corresponds to change of an alcohol group to a more electronegative carbonyl group (Fig 3.7 C). The reaction is likely to occur through the polymer chain and not just at the silver oxide and polymer interface due to the possibility of hydride shifts through the polymer chain.

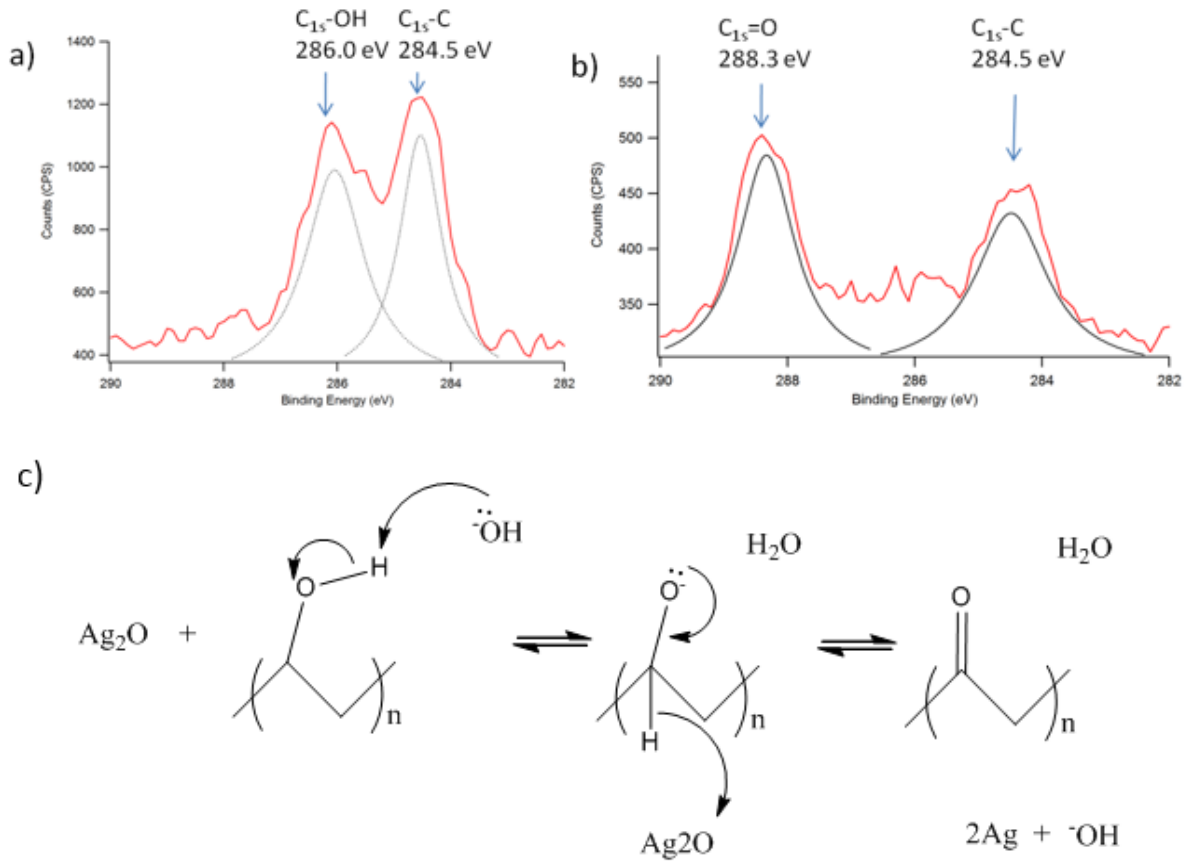

Figure 3.7 A) X-ray photoelectron C1s spectrum of polyvinyl alcohol 5wt% Ag_2O electrode B) X-ray photoelectron C_{1s} spectrum of polyvinyl alcohol Ag_2O electrode after placed in 1 M NaOH for five minutes C) Proposed mechanism for reduction of Ag_2O by a PVA binder.

For the above reason, PVA would not make for a good separator material in silver-zinc systems despite the reports of high hydroxide ion conductivities in PVP/PVA electrolyte [90] and PVA solid electrolytes [91]. A printed separator based on polyethylene oxide was used and polymers that have alcohol groups were avoided. We still examine methylcellulose due to its high conductivity. Methylcellulose could potentially be improved as a separator material if the degree of methylation is high enough. However, this would likely have an adverse effect on water solubility and ionic conductivity due to a reduction in the total hydroxyl groups. Another potential option is to incorporate a mixture of polymers or synthesis a copolymer to gain the benefit of high ionic conductivity and chemical inertness. We have chosen to examine polyethylene and methylcellulose for their use in a battery separator.

The molecular weight of the polymer chain has an influence on the solubility of the polymer in aqueous solutions. The larger the molecular weight, M_w, is, the lower the weight percentage of the polymer in the solution. A high mass loaded system is desirable for the final separator composition. A larger polymer content means a smaller water percentage. The end result of the deposition process should be a stable gel that does not have excess water that would compromise the previously deposited layers or cause spreading of the gel. This would mean using polymers with a lower molecular weight.

To achieve a printed separator system, the final separator was deposited on top of the two printed electrodes (Fig. 3.8). The printed planar electrolyte consisted of a KOH/PEO electrolyte deposition in a two-step process, where, first, the polymer solution was deposited on the electrodes, and second, a 17M KOH solution was deposited on the polymer solution to diffuse through the electrolyte. The KOH solution was deposited using a micropipette to give the appropriated mass ratio of KOH:H_2O:Polymer. Potassium hydroxide is used as the salt for forming the electrolyte rather than sodium hydroxide due to the higher ionic conductivity of aqueous KOH solution [92]. A PDMS encapsulant layer was placed on top of the printed battery to limit the evaporation of water from the battery stack. This layer is not the ideal battery barrier layer, however for the time frame for the battery discharge it is sufficient.

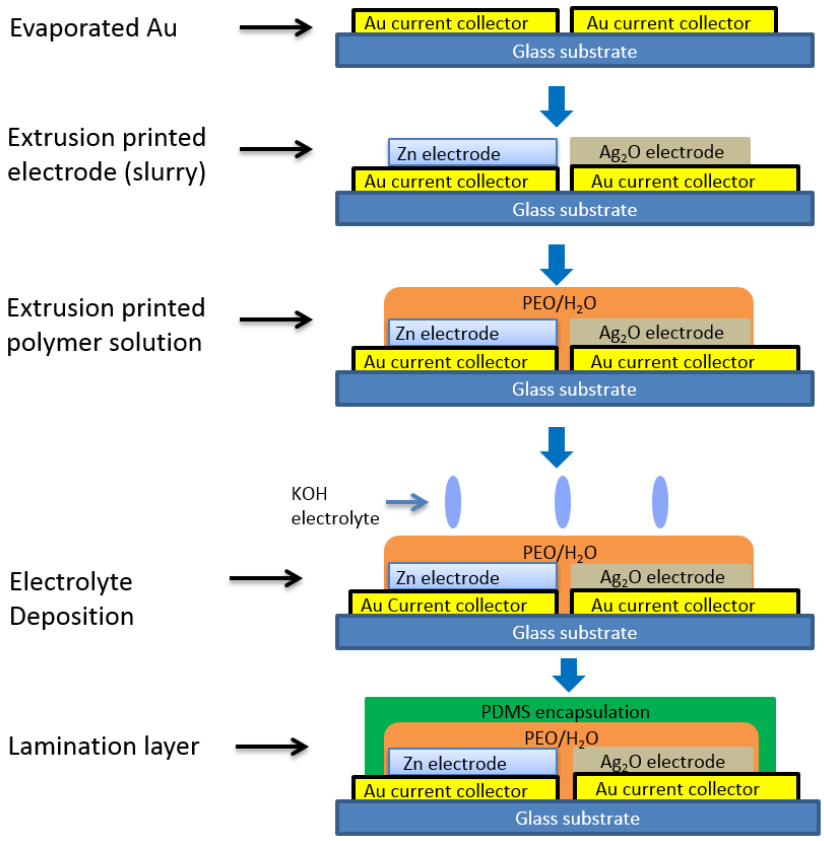

Figure 3.8 Partially printed planar battery process flow (not to scale).

This two-step process is not an ideal fabrication process due to increased complexity and increased variability introduced by the deposition of microliter amounts of electrolyte solution over the electrolyte and the reliance of diffusion of the K^+ and OH^- through the electrolyte layer. This technique also requires the diffusion of the KOH electrolyte through the polymer/KOH separator. The addition of the KOH caused the PEO solution to solidify due to ionic crosslinking of the PEO polymer chains. The separator layer is deposited to give a thickness on the order of 100 µm (Figure 3.9). This is done to ensure enough polymer material is deposited between the electrodes where the thickness of the electrodes is ~100 µm. This thicker layer also allows for a lower resistance of the electrolyte. Further optimization could be done to achieve a thinner layer at the expense of higher resistance.

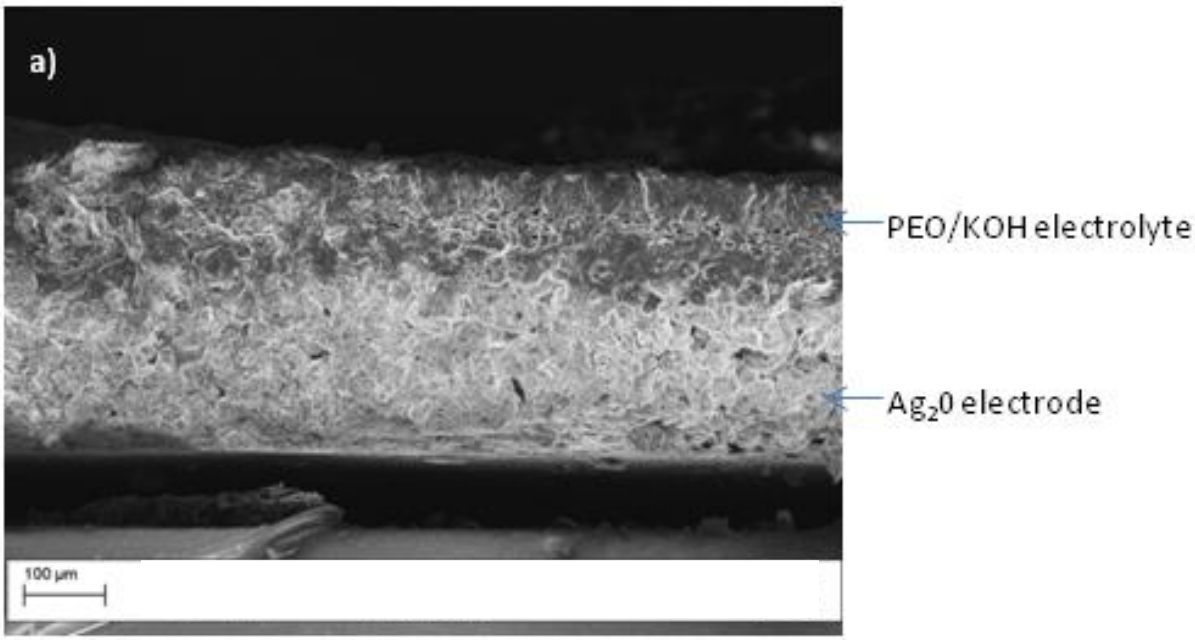

Figure 3.9 Scanning electron micrograph of the printed planar silver oxide electrode with a PEO/KOH electrolyte in the discharged state (discharged at C/2 rate).

3.3 Printed separator for an alkaline silver oxide battery

We have examined the influence of polymer length and the ratio of Polymer/KOH/H_2O on the performance of the cell rate. We specifically look at the polymer length of polyethylene oxide and the ratio of the polymer/KOH. We look at polyethyelene oxide ratio. We also examine the use of methylcellulose as a printed separator even though it will likely suffer from the above mentioned problem of reduction of the silver oxide. The limit of the mass loading of the polymer and KOH solutions is determined by the solubility of the polymer solutions. For the following experiments, we have kept a constant electrode composition using a 1:99 binder:active material ratio. This value was independently optimized as will be described in the following section (sections 3.4 and 3.5).

3.3.1 Separator optimization

The PEO and methyl cellulose electrolyte optimizations were performed with silver limited cells, since most applications of printed batteries will necessarily work in this configuration to minimize silver cost. The electrolyte composition is optimized with respect to polymer material (PEO and methylcellulose), polymer molecular weight and H_2O:KOH:PEO/cellulose ratio.

First, a polymer solution was extrusion printed on top of the electrodes, followed by pipetting the appropriate amount of potassium hydroxide from a 17 M solution using a micropipetter. The aqueous polymer solutions used were 50 wt% M_w=12,000 polyethylene oxide (Sigma-Aldrich), 10 wt% M_v=600,000 polyethylene oxide (Sigma-Aldrich) and 10 wt% methyl cellulose (27.5-32% methyl content, 10-25 mPa.s at 2wt% 20°C). Higher mass loadings were not achievable due to the limit of the solubility of the polymer into the solution. To reduce the water content of the electrolytes with 10 wt% PEO and 10 wt% methylcellulose, the batteries were partially dried at 50°C to give the appropriate electrolyte weight ratio. We have looked at H_2O:KOH:polymer ratios at 50:25:25, 57:29:14 and 66:17:17. Lower water percentage gels are difficult to achieve due to low mass loading of the polymer solutions, and the fact that higher water percentages do not form stable gels due to the excess water.

The fabricated batteries all demonstrated high open circuit voltages of ~1.55 V. All of the polyethylene oxide based separators show high internal resistances in the range of 130-200 Ω. The large resistance value is attributed to the unideal, planar architecture. The resistances also shows a lot of variation, indicating that the electrolyte concentration is not uniformly distributed through the polymer. The lower Ag_2O utilization of 66:17:17 H_2O:KOH:PEO electrolyte is attributed to the reduced hydroxide concentration and the poor hydroxide ion diffusion through the electrolyte. The higher water percentage may also lead to weaker integrity of the polymer binder.

Methyl cellulose as a separator provided the lowest resistance of all the separators examined, indicating good ionic transport properties (Table 3.1). However, the Ag_2O utilization is the lowest and exhibits the most variation. This low utilization is likely due to a capacity loss caused by the combination of the solubility of Ag_2O in KOH [93] and the ability of monovalent silver to oxidize the hydroxyl and terminal aldehyde groups of the cellulose leading to reduced silver [94]. This can be potentially reduced by using methyl cellulose with a methyl content close to 100%. However, this will reduce the solubility of cellulose in water which would require heating to remove the excess water in low wt% solutions. The degree of polymerization of methyl cellulose can reduce the number of aldehyde groups and increase the crystallinity of the cellulose structure, but this will also lower the cellulose concentration that is printable.

	50:25:25 H_2O:KOH:PEO (M_w=12,000)	57:29:14 H2O:KOH:PEO (Mv=600,000)	66:17:17 H2O:KOH:PEO (M_v=600,000)	57:29:14 H2O:KOH:Methyl cellulose
Ag_2O utilization (%)	96±3	94±3	78±20	59±32
Internal resistance (Ohms)	200±58	135±20	168±18	78±20
Open circuit voltage (V)	1.55±0.02	1.56±0.01	1.56±0.01	1.56±0.01
Energy density (mWh/g)	49±9	58±9	40±9	31±9
Areal density (mWh/cm^2)	4.0±1	4.1±0.3	2.4±0.4	2.4±0.6

Table 3.1 Summary of electrolyte optimization for a 1%PVA Ag20 and 1%PVA Zn electrode discharged at a C/2 rate. The internal resistance is calculated as a difference between open circuit potential and discharge potential after five minutes of discharge divided by the C/2 current.

3.3.2 Separator Optimization: Conclusion

Although the methylcellulose separator demonstrates low internal resistance, it suffers from the problem of low silver oxide utilization likely due the oxidation of the alcohol groups of the cellulose polymer. For this reason we have used a polyethylene oxide based separator for our printed, planar batteries. There is no statistical significant experimental difference between the two separators fabrication with a composition of 50:25:25 H_2O:KOH:PEO (M_w=12,000) and 57:29:14 H2O:KOH:PEO (Mv=600,000). Further carefully controlled experiments are required to identify if there is a difference between these two separator layers. The 57:29:14 H2O:KOH:PEO (Mv=600,000) layer appears to have slightly lower internal resistance, however it is not statistical significant.

3.4 Silver oxide electrode optimization

To develop the overall printed planar battery architecture, printed anode and cathode solutions were developed. For the anode and cathode layers, it is necessary to develop suitable printable electrode materials. To this end, it is necessary to develop electrodes containing the active material in a binder, such that the overall formulation is suitable for printing. We have looked at two different binders: the hydrophilic polymer, polyvinyl alcholo (PVA), and the hydrophobic polymer, polyvinylidene difluoride (PVDF). We also look at the addition of a conductive filler, acetylene black to the electrode conductivity to reduce the resistance of the electrode and increase the electrical contact between the silver oxide particles in the electrode. Acetylene black, also known as conductive carbon black, has been used in alkaline batteries to improve the conductivity of the electrodes [95]. This may be especially important for the silver oxide electrode, as silver oxide has a high resistivity of 10^8 ohm cm.

The electrodes were extrusion printed onto the evaporated gold contacts. The separation distance between the gold current collectors was 1 mm, with an individual electrode area of 4.5x10 mm^2. Silver oxide limited batteries were examined with an excess amount of Zn with a 3-4:1 Zn:Ag_2O ratio. The thickness of the silver oxide electrode was 100-110 µm (Fig. 3.10), while the thickness of the zinc electrode was ~100 µm. The analysis of the zinc electrodes was performed with a ratio of ~1.3:1 Ag_2O:Zn and a zinc electrode area of 2x10 mm^2 to maintain a similar thickness for the silver oxide and zinc electrodes. We optimize the Ag_2O and Zn electrode compositions using a 50:25:25 H_2O:KOH:PEO (polyethylene oxide M_w = 12,000) electrolyte deposited in a two-step procedure.

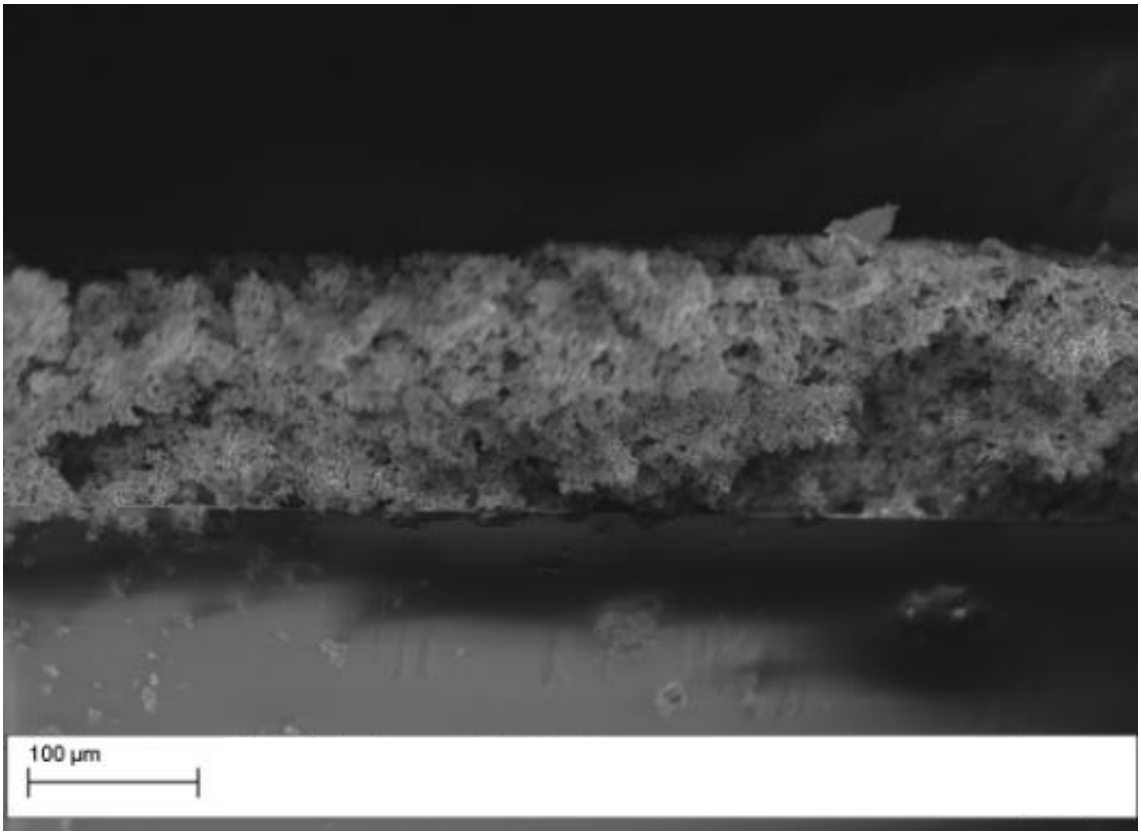

Figure 3.10 Scanning electron micrograph of a printed silver oxide (Ag_2O) cathode with a 1% PVA binder on top a gold evaporated glass slide.

Two different polymers, polyvinylidene fluoride (PVDF) and polyvinyl alcohol (PVA), were examined as polymeric binder materials for both the Ag_2O and Zn electrodes. PVDF was chosen for examination since it is a hydrophobic, inert polymer and is likely to maintain electrode composition with an aqueous electrolyte. It is similar to the other hydrophobic polymers, such as PTFE, that have been previously used in zinc electrodes [96]. PVA was chosen for examination since it contains hydroxyl groups that can facilitate hydroxide ion transport to the electrode surface. The PVA binder provides for mechanical stability by the ionic crosslinking of Na^+ ions with the hydroxyl functional group of the polymer.

Figure 2.6 shows the discharge characteristic of a silver limited battery with a 50:25:25 H_2O: KOH:PEO ratio for a (M_w=12,000) electrolyte and a 2% PVDF binder for the electrodes. After an adjustment period where the potential saturates to equilibrium, we see that the discharge voltage maintains a relatively flat constant discharge voltage until 50% of the deposited silver oxide has been utilized, at which point the potential starts decreasing to 80% utilization of Ag_2O capacity. The extracted performance of these curves are displayed in Table 3.2. Low Ag_2O utilization was realized when PVDF was used as a polymer binder (Table 3.2). The low utilization is attributed to the poor mechanical stability of the polymer in the alkaline environment. PVDF is a hydrophobic polymer and unlike PVA, cannot ionically crosslink with the K^+ ions of the alkaline electrolyte. The hydrophobic polymer may inhibit wetting of the electrodes, thus reducing the available hydroxide ions to precipitate in the chemical reaction.

High Ag_2O utilization is achieved with low percentages of PVA as a binder (Table 3.2). Full silver oxide utilization is not seen. One explanation for the decreased utilization is that the PVA polymer binder is oxidized to a ketone which is caused by a reduction of Ag_2O in the presence of hydroxide ions [93]. This suggests that at small binder percentages, PVA is a decent binder for a silver oxide electrode; however, at higher percentages, the binder may cause too large of a capacity loss.

We also observe that the incorporation of acetylene black does not lead to decreased internal resistance or increased Ag_2O utilization in any of the printed electrode formulations. The silver that forms on the surface of the particles due to the reduction of the silver oxide in the presence of PVA may allow for an increase in electrode conductivity, making the conductive filler, acetylene black, unnecessary. However, the addition of acetylene may increase the columbic efficiency of secondary Ag-Zn batteries where the electrode undergoes charge and discharge cycles. As the battery is charged, we see an increase in the formation of the highly resistive Ag_2O. The presence of acetylene black may improve the conductivity of the electrode, allowing for a greater percentage of conversion of Ag to Ag_2O. Pressing the formed electrodes might improve the contact between the silver oxide particles and conductive filler, acetylene black.

Ag_2O electrode	1% PVA	5% PVA	2% PVA, 3% Acetylene black	2%PVDF	2% PVDF 3%Acetylene black
Zn electrode	1% PVA	1% PVA	1% PVA	2%PVDF	2% PVDF
Ag_2O utilization (%)	96±3	94±4	93±4	80±14	78±11
Internal resistance (Ohms)	200±58	227±30	214±37	246±110	190±51
Open circuit voltage (V)	1.55±0.02	1.56±0.02	1.55±0.01	1.55±0.02	1.56±0.02

Table 3.2 Summary of the effect of the binder on the Ag_2O electrode with a (1:1 KOH:M_w=12,000 PEO electrolyte) discharge at a C/2 cathode current of 3.7 mA/cm^2. Internal resistance is calculated as the difference in open circuit potential and discharge potential after five minutes of discharge divided by the C/2 current.

Based on these studies, therefore, we proceed with an optimized Ag_2O electrode including 1% PVA binder, since this provides maximized silver utilization while providing good internal resistance and open circuit voltage. We do not use acetylene black since this battery is mainly targeted at primary cell applications. The presence of the PVA binder may increase the electrode conductivity by reducing silver oxide to silver, thus forming a conductive path between the silver oxide particles and eliminating the need for a conductive filler. For secondary batteries, however, the use of a conductive filler will likely lead to an improvement in the charge efficiency of the rechargeable battery.

3.5 Zinc electrode optimization

We examine the influence of the binder material, the conductive filler, and the binder percentage on the performance of the zinc electrode. We would like to have high zinc utilizations and low electrode resistance. The zinc electrode undergoes a dissolution mechanism where zinc is converted to the soluble species zincate which can precipitate to zinc oxide in the solution. The binder choice could significantly affect this reaction. We have looked at two different binders: the hydrophilic polymer, PVA, and the hydrophobic polymer, PVDF.

The optimized silver oxide electrode with 1% PVA binder material was tested against a zinc limited cell to determine the optimal anode conditions. Similar to the silver anode, a PVA and PVDF binder with an acetylene black additive were analyzed. The 1% PVA, 2%PVA/3% acetylene black and 2% PVDF binding materials all had similar open circuit voltages and internal resistances in the zinc limited batteries (Table 3.3). The addition of acetylene black as a conductive filler did not have a significant effect on the zinc utilization in the current percentages added.

	1% PVA	2% PVA, 3% Acetylene black	2% PVDF
Zinc utilization (%)	47±9	44±8	38±9
Internal resistance (Ohms)	197±26	196±20	210±15
Open circuit voltage (V)	1.56±0.04	1.56±0.02	1.56±0.02

Table 3.3 Summary of the effect of the binder on the zinc electrode with a (1:1 KOH:M_w=12,000 PEO electrolyte) ratio discharged at a C/4 anodic current of 8.1 mA/cm^2. Internal resistance is calculated as the difference in open circuit potential and discharge potential after five minutes of discharge divided by the C/4 discharge current.

The 1% PVA binder achieves the highest zinc utilization. However, the achieved utilization values are significantly lower than reported zinc utilizations of ~85% in 2% mercury amalgamated zinc electrodes for similar current densities [97]. The low zinc utilization observed in all three cases is likely due to a combination of loss of active material through formation of zincate species in the electrolyte in a corrosion process [98], formation of a passive ion blocking layer of ZnO and $Zn(OH)_2$ [99] and loss of electrical contact in the porous network of zinc particles due to the formation of a ZnO/ZnOH/$Zn(OH)_2$ resistive layer. The results indicate that an approximate 2:1

ratio of Zn:Ag_2O is necessary for full Ag_2O utilization with the current electrode composition and current density. Reducing the amount of electrolyte will decrease the absolute quantity of zincate in the solution, which may increase the zinc utilization. The incorporation of a surfactant, such as cetyltrimethylammonium bromide (CTAB), to the surface of the zinc electrode could reduce the corrosion rate of the zinc anode [100].

Based on these results we have decided to use a zinc electrode with a 1% polymer binder and no conductive additives, as acetylene black did not have a significant effect on the electrode performance. Further optimization could be done to increase the zinc electrode utilization, by examining how the particle shape and sized affects the electrode utilization. For example, zinc flake based systems may exhibit better electrode resistance and higher utilizations due to the better flake to flake contact. Zinc nanoparticles could also be developed and then sintered to form a continuous network of zinc. This would allow for a low resistance zinc electrode.

3.6 Three-electrode measurement

To monitor the discharge phenomena as the battery is discharged, we have incorporated a zinc pseudo-reference electrode into the battery architecture (Fig. 3.11). The reference electrode consists of a zinc wire that is placed in between the 1mm space between the electrodes. This pseudo-reference electrode keeps track of the two electrode potentials. Unlike the reference electrodes which are in thermodynamic equilibrium, pseudo-reference electrodes are typically not at thermodynamic equilibrium. The advantages of pseudo-reference electrodes are their simplicity, lack of liquid junctions and low potential for contamination [101]. Pseudo-reference electrodes have been made with silver, gold and Ag/AgCl wire. In corrosive systems, pseudo-reference electrodes are often made of similar materials as the working electrode. This is done to minimize the effect of corrosion. If a corrosive process occurs at the working electrode and the pseudo-reference electrode, the corrosion rate should be similar, leading to similar potentials in both electrodes and low electrode/electrolyte impedance.

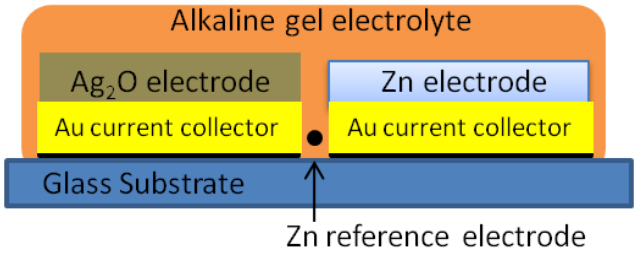

Figure 3.11 Experimental setup of three electrode setup (not to scale). A zinc reference wire is placed between the two electrodes.

The three electrode setup allows for the determination of the individual electrode potential during discharge of the battery. Figure 3.12 shows the typical discharge of a silver oxide limited battery. We see the potential of the silver oxide battery versus the Zn reference wire decrease near the end of the discharge with increasing time. This is what we expect since the battery was fabricated as a silver oxide limiting battery. Noticeably, the potential with respect to

the zinc electrode does not change during the discharge potential, indicating no significant impedance change to the zinc electrode which would change the potential.

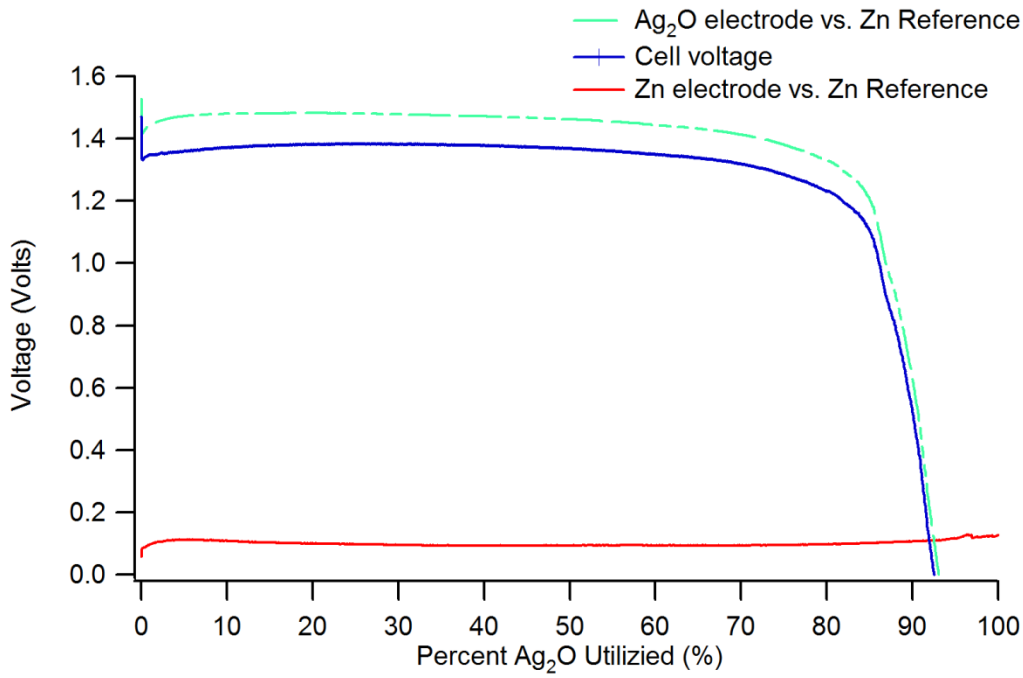

Figure 3.12 Discharge of a silver oxide limited battery with the three electrode setup.

This a minimally invasive technique that can be further used to examine electrode kinetics and electrolyte dependencies. Use of the zinc wire reference electrode will be described in Chapter 5, where electrochemical impedance spectroscopy is used to characterize the printed battery.

3.7 Performance of a planar printed silver oxide battery

We have demonstrated a planar, printed battery using extrusion printing as the deposition technique. An analysis of electrolytes with the polymers, polyethylene oxide and methyl cellulose, found that a dried 57:29:14 H2O:KOH:PEO (M_v=600,000) electrolyte had the highest areal energy density of 4.1±0.3 mWh cm^{-2} and a 94±3% Ag_2O utilization at a C/2 discharge rate of 1.8 mA/cm^2. The highest Ag_2O and Zn active material utilizations were achieved with a 1% PVA binder. The printed battery demonstrated an energy density of 4.1±0.3 mWh $cm^{-2.}$ The areal capacity of this battery is 3.5 mAh cm^{-2} which is comparable to literature capacities (Fig. 3.13). One thing to note is that the capacity can be inflated by printing thicker films to get a larger areal capacity. For this reason, it is also important to look at the volumetric energy density which takes into account the thickness of the battery.

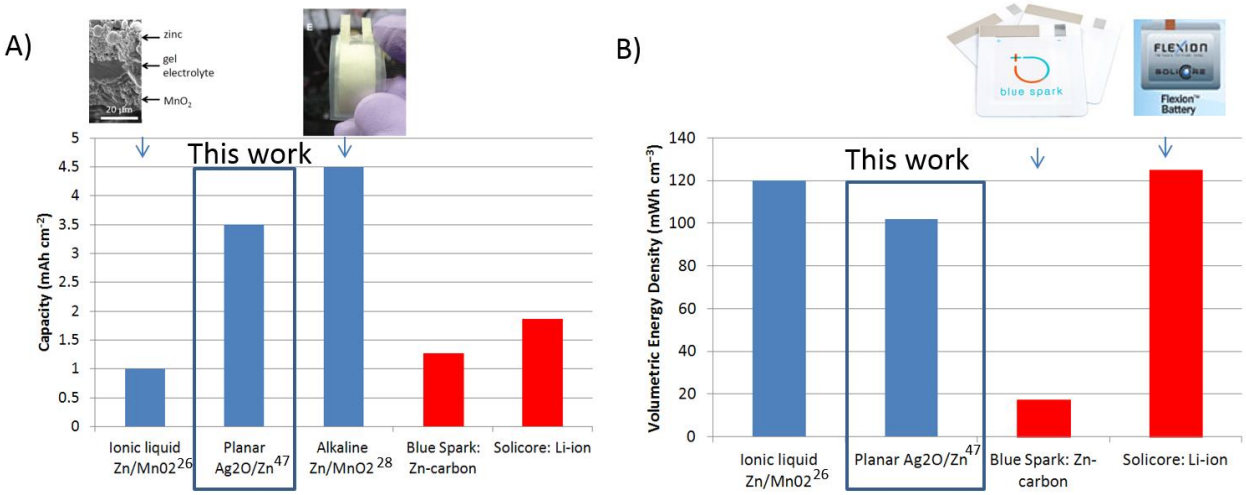

Figure 3.13 A) Areal capacity and B) volumetric energy density comparing literature values [26], [47],[28] and commercial products from Blue Spark and Solicore [102], [25].

This reported capacity is comparable to reported results in the literature and commercial batteries that can be purchased on the market. The highest energy density of 58±9 mWh mg^{-1} or 4.1±0.3 mWh cm^{-2} was achieved with the 57:29:14 H2O:KOH:PEO electrolyte. The energy density is comparable to the 1.2 mWh cm^{-2} achieved for a printable MnO_2-Zn ionic liquid battery [103] and an order of magnitude greater than the demonstrated 0.4 mAh cm^{-2} energy density of silicon-micromachined rechargeable nickel-zinc alkaline microbatteries [31]. The energy density could be further improved by optimizing the zinc content to a lower ratio of Zn:Ag_2O, reducing the amount of electrolyte used, or using the higher capacity, divalent silver oxide, AgO instead of monovalent silver oxide, Ag_2O. This shows promise for this printed battery technology. The planar architecture, although not ideal and introduces a high internal resistance, produces a battery that is still capable of high energy densities at high rates of discharge (C/2 rates, 1.8 mA/cm^2). Further improvements in the planar Zn/Ag_2O could be achieved by printing interdigitated electrodes or developing the printed layers into a vertical cell.

3.8 Conclusion

In this chapter we have demonstrated a planar, printed silver oxide battery. We have optimized the zinc electrode, the silver oxide electrode, and the PEO separator layer to achieve a high utilization and low resistance battery. The printed battery still suffers from relatively high internal resistance (150-200 ohms at a C/2 discharge rate) attributed to the non-ideal planar geometry. Although we used the planar architecture, which consumes more substrate area, the printed battery achieved high areal energy densities of 4.1±0.3 mWh cm^{-2} and capacities of 3.5 mAh cm^{-2}. This printed battery demonstrates the potential of the zinc-silver oxide chemistry for a printed battery capable of power printed electronics applications. Further optimization to enhance areal energy density can be performed by developing the techniques and materials for a vertical printed battery (Chapter 4).

Chapter 4. Printed battery with vertical architecture

The planar silver oxide battery described in chapter 4 suffers from high internal resistance due to the non-ideal planar geometry. Although the H_2O: PEO:KOH separator although capable of hydroxide ion transpoart, lacks sufficient mechanical stability to support a printed electrode. The ionic crosslinking that provides the separator with mechanical stability is weak and can be destroyed by the addition of an aqueous slurry or an ink that can solvate the ions in solution and essentially, dissolve the separator. For this reason, we require the development of a stable, high ionic conductivity separator layer. We have achieved this through the development of a photopolymerizable polyacrylic acid gel that contains a polyethylene oxide filler. This separator demonstrates good ionic conductivities with demonstrated ionic conductivities of 0.4 S cm^{-1}. Using this separator layer, we were able to stencil print the final electrode and current collector (Fig. 4.1). The entire process flow will be described later in this chapter.

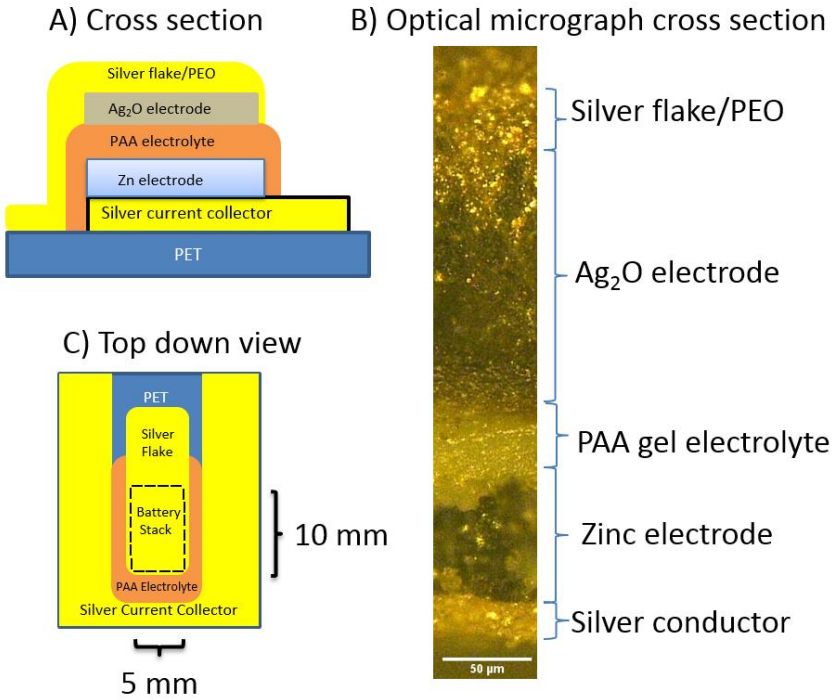

Figure 4.1 A) Cross section of printed battery stack with polyacrylic acid separator. B) Optical micrograph of dehydrated battery cross section. C) Top down view of printed battery.

4.1 Printed current collector

Developing a fully printed battery requires the development of a printed collector that is flexible and capable of withstanding the printing processes. A printed battery requires two printed current collectors: one current collector for the bottom electrode and a current collector for the top electrode. There are many possible ways to deposit a printed current collector.

4.1.1 Bottom printed current collector

One possible scheme is to use the zinc electrode as both the conductor and the negative electrode. This has been demonstrated in commercial Zn-MnO_2 planar batteries from Blue Spark where a laminated zinc foil serves as both the zinc anode and current collector [104]. One concern that needs to be taken into account when designing the electrode/current collector is the possibility for loss of conductivity of the electrode upon discharge, especially, near the leads where contact is made with the electrode. However, a working electrode is achievable by having an excess amount of zinc and the appropriate thickness electrode. This is more difficult to do in a printed porous electrode where electrolyte can diffuse through the electrode, and the conversion of zinc to zincate could occur throughout the electrode. We have therefore, focused on developing a printed current collector to use with the zinc (and silver oxide) electrodes.

A second possibility is to use an electrically conductive adhesive as the bottom current collector. Silver flake conductors in the form of electrically conductive adhesives (ECAs) have demonstrated high conductivities of 0.00035 Ω cm [105]. Conductive adhesives have been widely characterized, and several products are available on the market, such as Dow Corning ® DA 6524 Electrically Conductive Silicone Adhesive. These conductive adhesives typically consist of a conductive filler (silver, copper or graphite) at a concentration near 80wt% and a binder component that holds the conductive filler together. Silver PDMS conductors have been demonstrated to have conductivities between 10^{-2} Sm^{-1} to ~10^4 S m^{-1} depending on the silver to PDMS percentage [106]. When the percentage of silver is increased from 10^{-2} Sm^{-1} to ~10^4 S m^{-1}, the silver particulate (1-2 µm flakes) percentage is increased from 83wt% to 86wt% past the percolation threshold [106]. The increase in conductivity is attributed to increased particle contact. High conductivities result from high silver percentages; however, high percentages of solid material also lead to inflexible material that is prone to breakage. Silver based PDMS conductors require a temperature step of at least 100°C to polymerize the siloxane-based monomers. There are photopolyemerizable PDMS formulations, but these PDMS formulations still require a thermal step (120C°) to complete the polymerization [107]. This high temperature step is incompatible with the aqueous environment of a silver-zinc battery; however, the silver/PDMS composite could be suitable for the bottom current collectors, as it is deposited before the battery stack is deposited.

We have examined the use of a silver/PDMS composite as a potential current collector by preparing a mixture of silver powder, Dow Corning *Sylgard 184* Silicone Elastomer, with micron sized silver particles (Sigma Aldrich). The composite was stencil printed onto a glass substrate from a 300 micron stencil followed by annealing at 80°C for three hrs. We have looked at silver percentages from 60 to 80%. Higher silver percentages resulted in poor polymerization due to the low PDMS content. Figure A shows the resistivity of several low temperature printed current collectors prepared with micron sized silver polymers. The resistivity was determined using the four point probe measurement, and the resistivity was determined using the equation

$$\rho = \frac{\pi}{\ln(2)} t\left(\frac{V}{I}\right) = 4.523t\left(\frac{V}{I}\right)$$

This equation can be applied for the thin film current collectors since the film thickness, t, is less than the probe spacing, s/2.

From Figure 4.2, we see a decrease in resistivity with increasing silver percentage, indicating better particle to particle contact with a higher silver percentage. The conductivity of the PDMS composite could be improved by replacing the silver powder with silver flakes. We see that the resistivity is still two orders of magnitude larger than commercial ECAs, such as Creative Materials conductive ink (Fig. 4.2). This means that the Creative Materials silver ink is a much better conductor. If we use the Creative Materials ink as the current collector in the battery stack we require a thinner current collector, which would lead to an increase in the volumetric energy density.

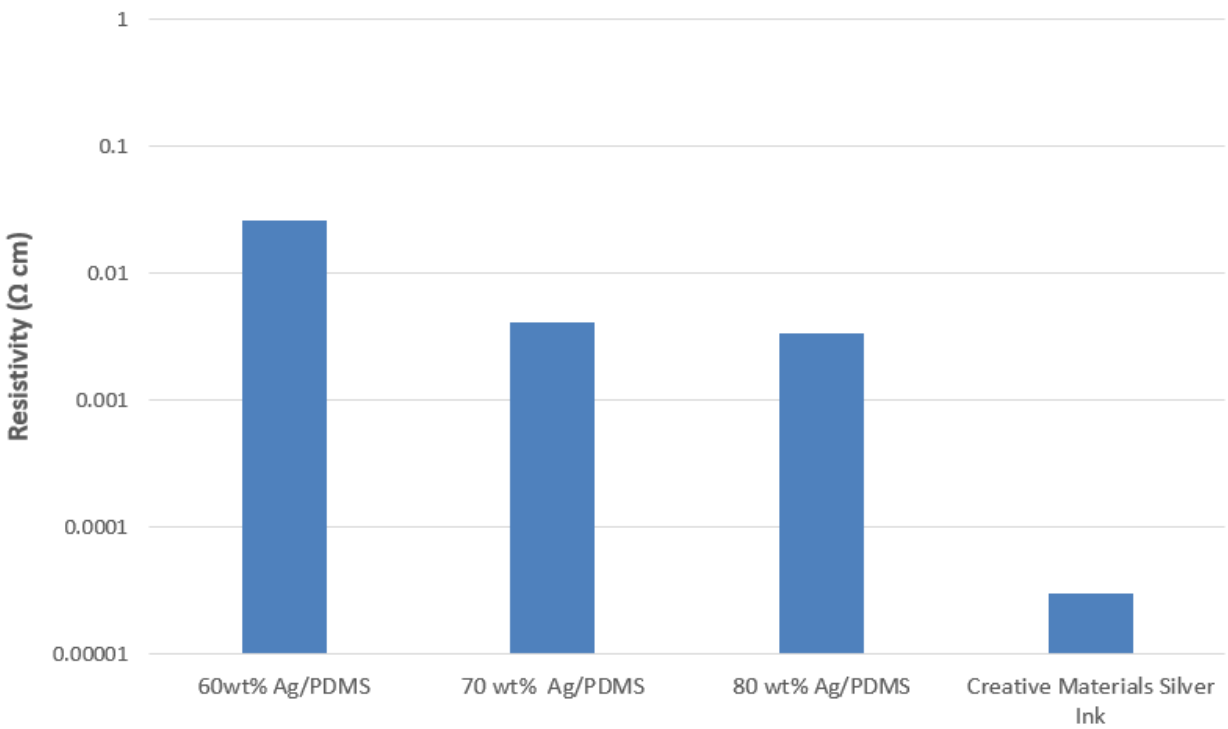

Figure 4.2 Comparison of the resistivities of Ag/PDMS composite ink and a commercial conductive ECA (Creative Materials ink 120-07).

The printed current collector should have a high conductivity, and be flexible and printable. The screen printable ink from Creative Materials satisfies these conditions and has a low resistivity of 0.0004 ohm-cm (Fig. 4.2). For these reasons, we have chosen to use an ECA, a commercial conductive ink from Creative Materials, for the bottom current collector. It is also a commercially available product so it ideally shouldn't suffer from reliability issues. Although the Creative Materials ink requires a high annealing temperature (>100°C), the bottom current collector and substrate can experience a high temperature as long as the substrate can handle the annealing temperature.

We have chosen to use stencil printing to deposit the current collector since we need to deposit the current collector over a large area on the order of 1 mm^2. This ink, Creative Materials 120-07, is a screen-printable conductive ink with a viscosity of 26,000-30,000 cps [108]. The ink requires a curing temperature of 110°C for three to five minutes. The cured ink is specified to have a volume resistance of 0.00003 Ω-cm. We have used this ink for printing the bottom current collector. To demonstrate a flexible battery, we have decided to use PET or polyethylene terephthalate as our substrate. PET is a cheap plastic with a melting point above 260°C but a glass transition temperature between 67 to 81°C [109]. We have used stencil printing to deposit the Creative Materials ink on to the PET substrate. We then do a ten minute cure at 105°C. This temperature is above glass transition temperatures; however, there is not a significant change to the plastic substrate.

4.1.2 Top printed current collector

Another ink is required for the top current collector of the vertical battery. The Creative Materials ink cannot be used due to the high curing temperature. The top current collector ink should ideally be a low processing temperature ink that will be compatible with the entire battery stack. For this reason, we have focused on using a metallic flake as the basis of our conductor. Ideally, we would like to have a metal flake with a binder material that will hold the collector together and be stable in an alkaline environment.

We have used the principle of ionic crosslinking to achieve sufficient mechanical integrity of the current collector. We have developed a silver flake conductor by using a high molecular weight polyethylene (M_v~600,000) oxide polymer as the binder material. Polyethylene oxide is an inert binder that ionically crosslinks at high pH values, imparting mechanical stability to the electrode at high pHs. We have prepared PEO/silver flake (particle size 4-8) solutions with varying PEO/silver flake ratios. The solutions were prepared by adding the appropriate amount of silver flakes to a 5 wt% solutions of polyethylene oxide (M_v~600,000) to give a PEO:silver flake ratio of 10:90, 20:80 and 70:30 (Fig. 4.3). The silver flake slurries were stencil printed with a 300 µm stencil to give dried thicknesses varying from 20 to 50 um depending on the slurry composition.

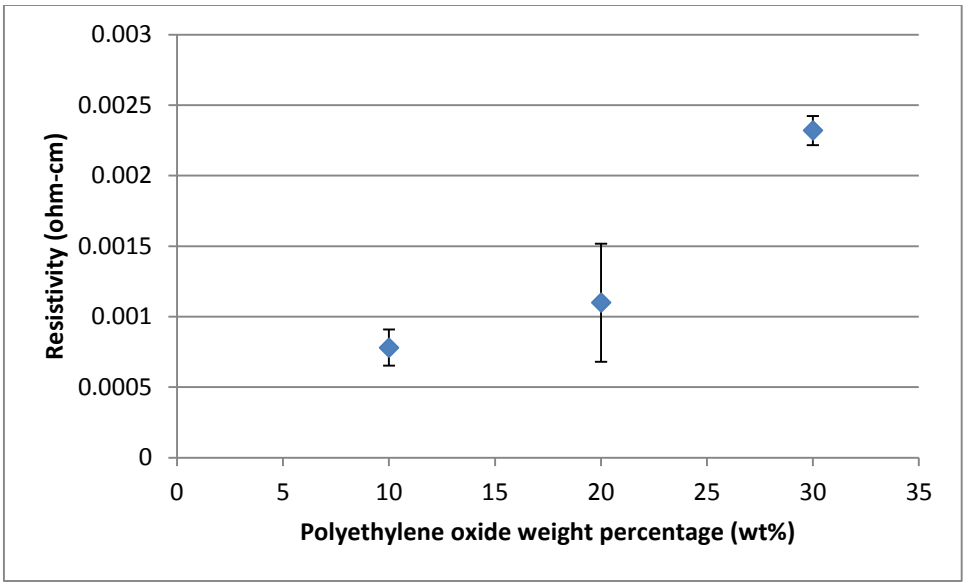

Figure 4.3 Resistivity of PEO/sliver flake based conductors.

We see a general decrease in resistivity as we decrease the PEO content (Figure 4.3). However, the value appears to start to saturate at 20 wt% loading of PEO, at a resistivity of ~0.001 Ω-cm. This value is a factor of five less than the current collector prepared with larger silver particles (Fig. 4.3). Due to the lower resistivity and stability provided by the ionic cross linking of polymer chains, a mass loading of 20 wt% PEO was chosen to be used as the printed current collector for a printed battery.

Using this current collector composition (80:20 Silver:PEO), we can calculate what thickness we will need to deposit for a top current collector. This assumes that the resistivity of the PEO/silver flake current collector maintains its conductivity after exposure to the alkaline electrolyte. We ideally want the current collector resistance to be as low as possible to minimize the ohmic contributions of the cell. To be on the same order of the electrolyte resistance (0.06-1.0 ohms, Chapter 6) we ideally want to have a resistance of 1 ohm or less. Assuming a width of 5mm and a length of 15mm, we need to have a thickness of approximately 30 µm to achieve a resistance of 1 Ω.

$$t = \frac{\rho}{R}\frac{l}{w} = \frac{0.001\ \Omega\ cm}{1\ \Omega}\frac{15\ mm}{5mm} = 30\ \mu m$$

Thicker films could be used to achieve lower current collector resistances at the expense of lower energy densities and a possible decrease in flexibility.

Thus, we have used two different ink formulations for the two current collectors. A conductive adhesive from creative materials was used for the bottom current collector, and a printed Ag flake/PEO ink was used for the top current collector.

4.2 Printed PAA separator

The vertical printed battery requires the development of a new separator that is capable of being integrated into the printing process flow. We have achieved this separator by using a polyacrylic acid separator. Polyacrylic acid is an excellent water absorbing polymer because of the ability of the carboxylic acid functional group to solvate water molecules. The carboxylic acid molecule is also in a fully oxidized state, i.e. the functional group cannot be oxidized like the alcohol functional group can be oxidized to a ketone (Chapter 3). As a result, it is chemically inert to the oxidizing agent silver oxide. Furthermore, polyacrylic acid based separators have reported to have high ionic conductivities, on par with KOH solutions [28], [110].

Previously, a polyacrylic gel electrolyte has been demonstrated in a mesh based printed PAA electrolyte Zn–MnO_2 battery [28]. In this mesh based battery, the PAA (M_w~1,250,000) was dissolved in a 8M KOH solution at concentrations ranging from 1.1% to 1.9%. The electrolyte layer was subsequently dropcast on a 200-mesh size (holes per inch) nylon mesh. The overall thickness of the separator and PGE layer was 80 µm. This electrolyte layer was then assembled with a printed MnO_2 mesh electrode and a printed Zn mesh electrode. This method of fabrication and use of a mesh is not ideal for a printed battery. In addition, the mesh takes up extra volume which will decrease the volumetric energy density. The long term stability of the separator may also be of concern due to the slow hydrolysis of the amide bond of nylon [111].

Separator films made by esterification of PVA and PAA have also been reported for use in alkaline Zn–MnO_2 batteries [112]. However, the PAA separator formed by esterification is not stable in basic solutions and can hydrolyze in alkaline solutions over time, limiting its long term use in a battery. To improve upon the mechanical stability of the separator layer, we have developed a polymerized PAA gel separator based on a base stable crosslinker.

Polymerizations of acrylic acids have been previously reported before using peroxide radical initiators such as ammonium persulfate [113], [114]. An alkaline separator based on a polyacrylic acid gel has been synthesized from the constitute acrylic acid monomers and a *N*,*N*_methylene-bisacrylamide crosslinker in the presence of a KOH electrolyte [110]. The resulting gel electrolyte with the MBA crosslinker has been proposed for use as a separator layer for in Zn/MnO2, zinc-air batteries. The separator chemistry has two main disadvantages that make it a poor separator for a printed battery. Firstly, the gel synthesis is a free radical polymerization using thermal degradation of sodium persulfate to form a free radical. A disadvantage of using a peroxide radical initiator is that the polymerization would start when the peroxide radical initiator was added to the gel solution. A second potential problem with this polymerization is the crosslinker, *N*,*N*_methylene-bisacrylamide (MBA), has two amide bonds which can be hydrolyzed in highly basic solutions. The rate of hydrolysis is dependent on the pH of saturated gel, but in the pH regime of 14, the hydrolysis is likely to occur quickly as the half-life of an amide bond (amide bond of *N*-(phenylacetyl)glycyl-d-valine) in a pH=14 environment is 2.7 days ($k_1 = 3.2 \times 10^{-6}$) [115]. Based on the work of this paper, we have developed a high ionic conductivity, photopolymerizable PAA gel separator with a couple of variations. We have changed the free radical initiator and the crosslinker and added a PEO filler polymer. These modifications allow for a printed, mechanically stable alkaline separator.

We synthesize a gel network using a base stable crosslinker, acrylic acid monomer, a photoinitiator and a PEO filler polymer (Fig. 4.4). To control when the polymerization occurs, we have decided to use a photoinitiator as the molecule that generates the free radical. This effectively allows for a separation of the printing and polymerization process.

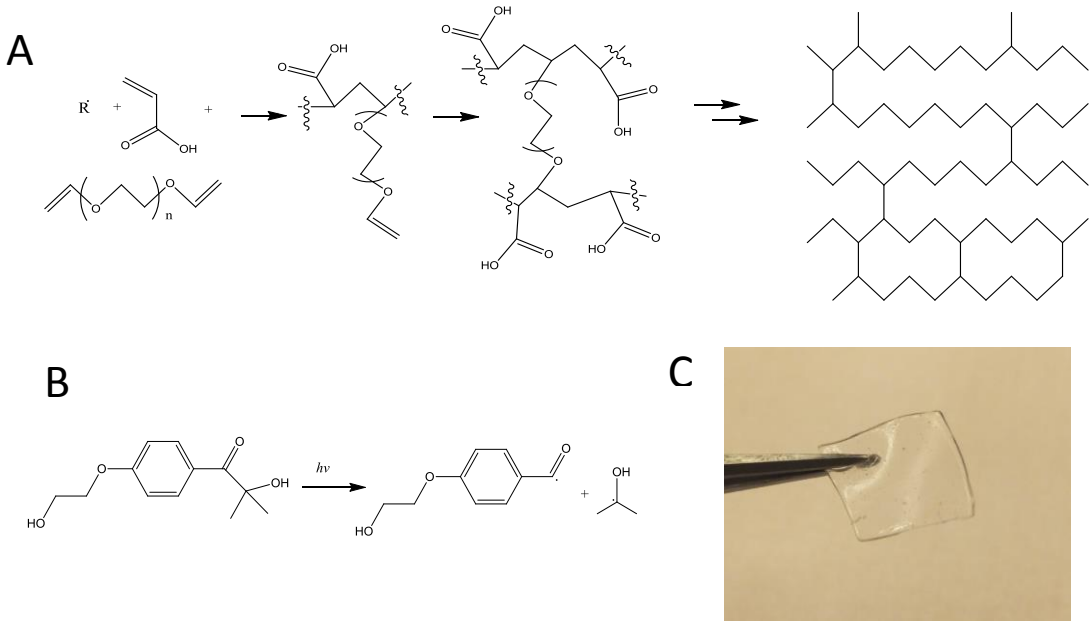

Figure 4.4. A) Polymerization scheme of polyacrylic gel electrolyte where R is the water soluble photoinitiator, 4-(2-hydroxyethoxy)phenyl-(2-hydroxy-2-propyl)ketone B) Photolysis of the photoinitiator after exposure to UV light C) Polymerized PAA gel separator.

We have selected the water soluble photoinitiator 2-hydroxy-4-(2-hydroxyethoxy)-2-methyl-propiophenone (also known as IRGACURE 2959) (Fig. 4.4B) as our photointitiator. This molecule has an absorption maximum near 275-280 nm (Fig. 4.5) and a solubility of ~1% (g/100 g) in water. For our acrylic acid solutions, we have used a photoinitiator percentage of 0.5wt%. By illuminating the printed gel solution with UV light (Spectroline UV lamp), we can form the free radical to initiate the polymerization. The UV light intensity (peak at 365 nm) doesn't exactly match the absorption spectrum of IRGACURE 2959, but enough initiator undergoes photolysis to form the free radical.

To impart mechanical stability to the polyacrylic acid polymers, we have used a base stable, water soluble crosslinker. We have used poly(ethylene glycol) divinyl ether (PEGDE) (M_n~250) for the crosslinker (Fig. 4.4 A). This polymer is water soluble in small concentrations due to the extended poly(ethylene glycol) backbone. A crosslinker concentration of 1wt% was used in the PAA gel as this was found to give optimal performance. Lower concentrations resulted in incomplete gel formation with insufficient mechanical strength. Higher concentrations (5-6 wt%) had poor solubility, degrading ink properties during printing.

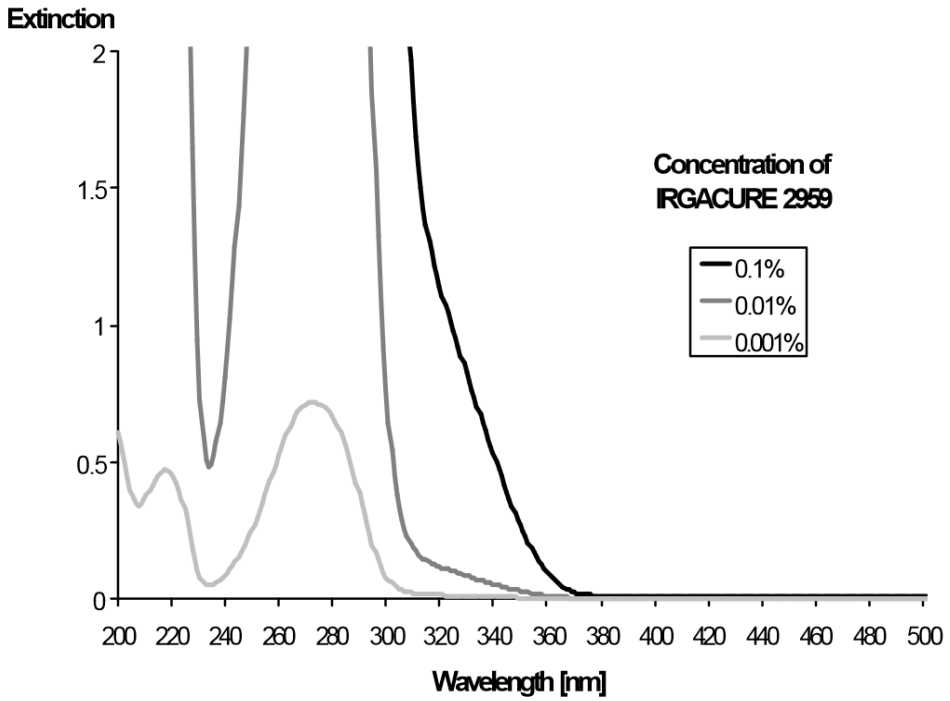

Figure 4.5 UV-Vis absorption spectrum of IRGACURE 2959 (Source: Ciba IRGACURE 2959 [116]).

To increase the mechanical strength of the polymerized separator, we have incorporated a high molecular weight polyethylene oxide polymer (M_v~ 600,000) to the solution. This filler material allows for ionic crosslinking with potassium hydroxide electrolyte and sterically hinders the polyacrylic acid chains during hydration with the KOH electrolyte. Another advantage of this filler polymer is that it allows for tuning of the viscosity of the acrylic acid solution. The molecular weight could also be modified to tune the viscosity, but for this work, we have kept the molecular weight constant at M_v~600,000.

4.2.1 Photopolymerization of the PAA gel separator

The gel solution was prepared by mixing 0.5 ml of acrylic acid (7 wt%) with 6.25 ml of H_2O that contained 1 molar equivalent of KOH (0.4092 g). This is done to neutralize the acrylic acid and bring the pH to 7. The salt form, sodium acrylate, could also be used to prepare the separator gel solution. A 7 wt% percent solution was chosen as increased percentages of acrylic acid lead to unwanted swelling when exposed to the KOH electrolyte.

For the above dissolved solution, the appropriate amount of PEO (M_v ~600,000) was dissolved into the solution by stirring at 300 RPM at room temperature. For example, for a 2.5 wt% PEO concentration, 0.1930 grams of PEO was added to the solution. After the PEO dissolved, the water soluble photo-initiator 4-(2-hydroxyethoxy) phenyl-(2-hydroxy-2-propyl)ketone 0.5wt% (0.0354 g) and crosslinker poly(ethylene glycol) divinyl ether (PEGDE) (M_n~250) 1.0wt% (0.0723g) were added to the solution. Once dissolved, the solution was sparged by lightly bubbling nitrogen gas through the solution for ten minutes to remove oxygen.

The deposited gel will determine the shape of the polymerized separator. The gel solution was then stencil printed inside a 300 µm thick stencil to give a polymerized thickness of ~200 µm above the Zn electrode after polymerization. The PDMS stencils were prepared by spincasting PDMS on a FOTS treated silicon wafer. By controlling the spin rate and spin time, we can control the thickness of the PDMS layer. A calibration curve for different RPMs (90 second spin) is demonstrated in Figure 4.6. Using this curve, we can select the desired stencil thickness from the spin rate. After spinning the PDMS film, the PDMS was cured at 150°C for ten minutes. The desired area to be exposed was removed by cutting the PDMS to leave an exposed area the size of 15x10 mm^2.

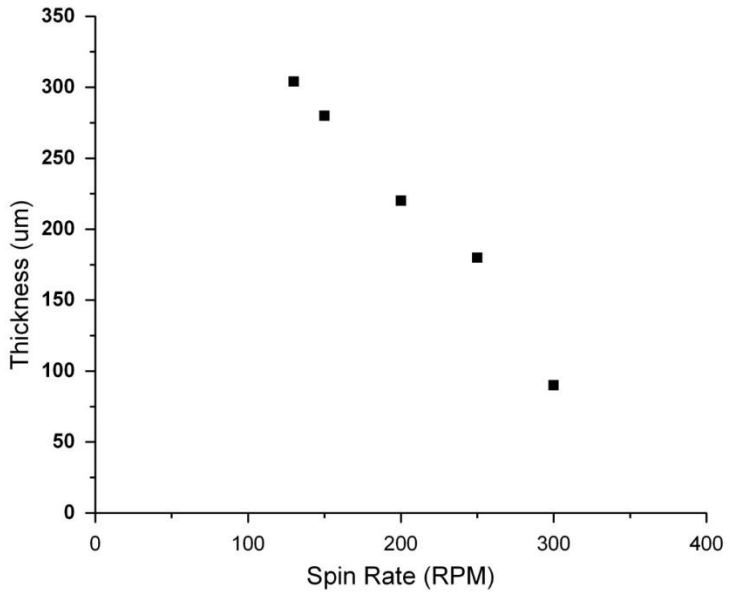

Figure 4.6 Dependence of cured Sylgard 184 PDMS thickness after spinning for 90 seconds at the listed spin rate and annealing at 150°C for 10 minutes.

Termination of the free radical also represents a problem during the gel synthesis and crosslinking. Termination can result from coupling (two radicals joining to form a single bond), disproportion (radical attack on hydrogen at the second-to-last carbon in the second chain), or interaction with an impurity or an inhibitor. Oxygen is a common inhibitor and can slow the polymerization reaction. Specifically, the growing polymer chain or free radical can react with oxygen to form an oxygen radical, thus slowing down polymerization. Oxygen inhibition can be avoided by bubbling nitrogen through the liquid precursor and performing the polymerization in an inert environment.

In the current polymerization scheme, inhibition is a problem for the creation of thin separator layers. Depositing and cross-linking a 100 µm thick film is not possible with the current electrolyte solution due to exposure of the electrolyte to oxygen in the atmosphere. However, the electrolyte can be photocrosslinked after the deposition of the electrolyte, after the placement of a UV-transparent oxygen barrier layer, such as glass or piece of polyethylene *terephthalate.* The PET barrier layer removes the oxygen exposure from the atmosphere, which can inhibit polymerization by termination.

The curing time depends on the energy of the radiant dose. We illuminate the PAA gel for 10 minutes to insure complete photolysis and polymerization. We turned on the UV lamp 10 minutes before the start of polymerization to insure that the light intensity from the UV lamp had reached a saturation value of ~6 mJ cm^{-2} (at 365 nm), before illuminating the printed gel solution. After the polymerization is complete, the stencil is removed and the silver oxide electrode is deposited on the polymerized separator layer followed by the Ag/PEO flake current collector.

4.2.2 Mechanical properties of PAA separator

In general, the polymerized crosslinked gel should not only be a good ion conductor but also be mechanically robust. The separator layer should be flexible, able to withstand the preceding deposition techniques, and resist puncture. For rechargeable lithium batteries, there have been studies that have shown if a polymeric separator has a high enough shear modulus, it can stop lithium dendrite growth [117]. We are not considering rechargeable batteries in this work. We care about developing a separator layer that is mechanically stable for the printing process flow. To achieve this goal, we have increased the mechanical stability of the hydrogel gel electrolytes by the addition of a filler molecule, polyethylene oxide.

The mechanical strength of a polymer gel can be modified by many different gel parameters, such as a crosslink density and crosslinker choice. An increase in the crosslink density results in an increase in the strength of the gel at the expense of the time it takes to saturate the gel [118]. The mechanical strength of the PAA separator can be drastically improved with the addition of the polyethylene oxide filler (M_v~600,000) (Fig. 4.7). The polyethylene oxide filler can ionic crosslink with the positively charged ions of the electrolyte and also impede the swelling by sterically hindering the swelling of the polymer chains in the gel network.

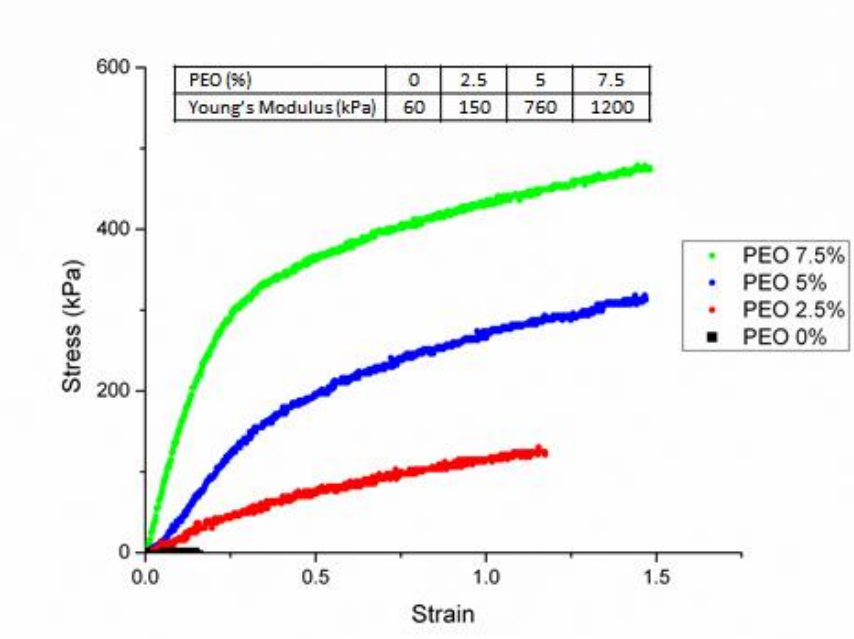

Figure 4.7 Stress-strain curves of polymerized separator (saturated with 8.4 M KOH) with various amounts of PEO filler (M_v~600,000). Inset extracted young's modulus from the elastic region.

Tensile measurements were performed using a Bose Electroforce 3200. The measurement was performed with 8.4 M KOH saturated PAA gels that had a polymerized dimension of 10mm x 5mm x 0.3mm. Stress (σ)-strain(ε) curves were calculated by taking into account the cross-sectional area and the strain of the PAA gels. The gels were placed between the two clamps of the Electroforce with a separation distance of 5-6 mm. Extensions were done until a distance of 7 mm was reached. During the extension of the polymer, there is a cross-sectional area difference that will change the actual stress, but for low extensions, the stress-strain measurement should be accurate. The addition of a PEO filler results in an increase in the Young's modulus of the resulting gel as seen in Figure 4.8. The increased stability is proposed to be a result of the polymer strands ionically crosslinking with each other and the steric hindrance introduced by the long chain polymer [119].

4.2.3 Printability of the PAA separator

The alkaline separator should be printable and have good mechanical stability. These are usually opposing goals, as something that is mechanically stable is often not easily printable unless it goes through some sort of phase or compositional change after printing. We have separated these two aspects of the separator by using a photopolymerizable solution that becomes crosslinked under UV illumination. To further increase the stability we have added a polyethylene oxide filler molecule (M_v~600,000). This addition has improved the mechanical strength of the separator as seen by the previous chapter. However, the addition of the long chained polymer filler drastically changes the solution properties.

The most significant change in the solution is the change in viscosity of the prepolymerized solution. At higher PEO polymer concentrations, the viscosity of the solution increases drastically (Fig. 4.8). The increased viscosity traps nitrogen bubbles during degassing, which remain in the pre-polymerized solution and introduce holes in the final polymerized film. These holes allow for shorting during the silver oxide electrode deposition. By using a PEO filler of 2.5 wt%, we are able to achieve good mechanical stability without bubble inclusion.

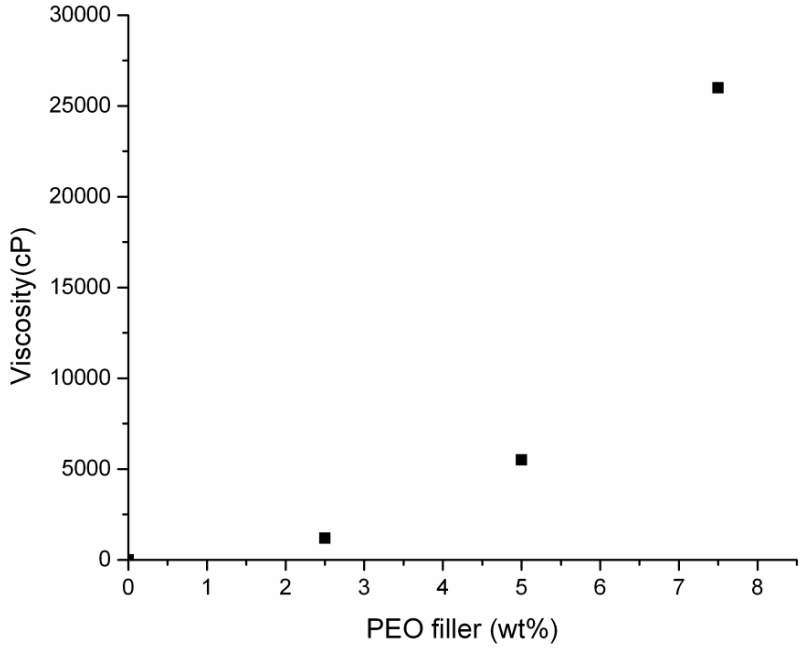

Figure 4.8 Dependence of viscosity of the prepolymerized gel solution on a PEO filler (M_v~600,000).

Other methods to remove the bubbles from the solution could be used, such as vacuum purging of the bubble filled solution. This would possibly allow for the fabrication of an even more robust separator layer with higher mass loading of the PEO filler molecule. Other molecular weights of polyethylene oxide could also be used to reduce the viscosity and increase the filler content. However, the properties of the currently achieved separator are more than adequate for the application herein.

4.2.4 Swelling properties of PAA separator

Polyacrylic acid gels are hydrogels that are capable of absorbing large amounts of water due to the ability of the carboxylic acid functional groups to associate with water [120]. The amount of water absorbed can be modified by controlling the crosslink density or the ratio of the crosslinker to monomer, adding fillers to the gel, or by changing the amount of cyclization [121]. The prepared crosslinked polyacrylic acid gel electrolyte acts as a hydrogel that can absorb water. The anionic carboxylic acid side chains of the crosslinked polymer are capable of associating with a large number of water molecules. The absorption of water by the separator is going to depend on the pH of the saturating solution, temperature, percentage of carboxylic acid functional groups, crosslinking density and the extent of polymerization of the gel.

Some common metrics for characterizing hydrogels are the mass and volume swelling ratios. These values are typically defined as:

$$Q_m = \frac{mass\ of\ swollen\ gel}{mass\ of\ dry\ gel}$$
$$Q_V = \frac{volume\ of\ swollen\ gel}{volume\ of\ dry\ gel}$$

The hydrogels swell due to the ability of side chains to associate with water. During swelling, water molecules are driven into the gel by an osmotic pressure created by the charge-charge repulsion of the ionic side chains [122]. The osmotic pressure is counterbalanced by the elastic force of the polymer sections between the crosslinking points. Essentially, each polymer chain wants to be solvated by the solvent molecules; however, the elastic restoring force prevents complete solvation. Equilibrium is reached once the forces balance each other.

The elastic force for a single Gaussian chain is given as [123]:

$$F_{elas} = \frac{3kT}{Nb^2}h$$

where *h* is the length of the extended chain, *N* is the number of unit lengths in the chain, and *b* is the unit length. In a gel network, N, the number of unit lengths in a polymer chain between two crosslinks, is inversely proportional to the crosslink density. More crosslinking in a gel results in shorted chain length. The shorter chain length corresponds to a stronger elastic force and thus, a greater swelling of the gel network. The larger elastic force should allow for a larger osmotic pressure and shorter time to equilibrium. We see this trend in Figure 4.9. We vary the crosslinker percentage. Lower crosslinker percentages correspond to a lower crosslink density. At lower cross linking percentages, we see a shorter time to reach equilibrium and an increase in the swelling ratio.

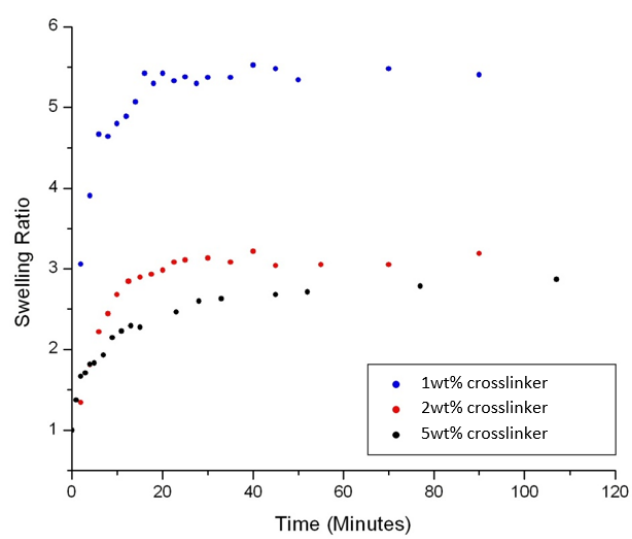

Figure 4.9 Swelling ratio (Q_m) time dependence for various crosslinker percentages without polyethylene oxide filler.

To measure how the polymerized gel responds to different solution conditions, we have prepared a PAA gel separator with the 2.5% PEO filler. The gel was polymerized using a PDMS stencil that had dimensions of 10x10x0.5 mm^3. The polymerized gel was dried and saturated in KOH electrolyte solutions at different pH solutions. We observed a decrease in the swelling ratio with increasing KOH concentration (Fig 4.10). At high salt concentrations, the salt can compete with the polar side chains of the polyacrylic acid hydrogel. In this case, the free water concentration drops. As a result, the carboxylic acid functional groups are solvated by fewer water molecules. This effectively reduces the swelling ratio.

For developing a printed separator, we want to minimize the swelling of the polymerized gel separator. Large swelling ratios create instability in the battery, leading to rupture of the battery stack. However, some swelling is necessary to introduce the electrolyte into the separator and activate the layer with the KOH electrolyte. Figure 4.10 indicates that we want to use higher molarities of KOH to saturate the PAA separator.

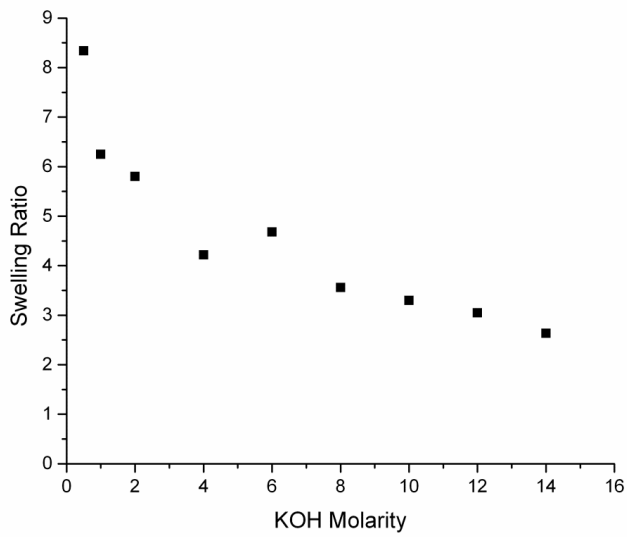

Figure 4.10 Swelling ratio (Q_m) of polymerized gel (2.5wt% PEO) with various KOH solution molarities.

4.2.5 Conductivity of the PAA separator

The ideal separator should have high ionic conductivity to minimize the ohmic resistance of the battery. We have characterized the conductivity of the polymerized gel as a function of KOH molarities. The ionic conductivity of the gel electrolyte was measured by electrochemical impedance spectroscopy (EIS). EIS was performed with a Gamry 3000 potentiostat. Impedance measurements were taken by placing the KOH saturated separator gel between two 403 stainless steel sheets. Impedance measurements were performed from 1 MHz to 100 Hz with a 4 mV RMS sine wave. Samples were prepared by polymerizing the gel solution with a PDMS mold with the desired thickness (0.3mm to 2mm) and gel area of 5x5 mm^2. The gels were swelled with the appropriate electrolyte for at least 30 minutes before performing impedance spectroscopy. The

ionic conductivity, σ, of the electrolyte is extracted from the equation, $\sigma = \frac{l}{RA}$, where l is the thickness of the electrolyte, A is the surface area, and R is the corrected resistance of the saturated separator taken from the impedance spectrum. The resistance of the gel is extracted from the intersection of the impedance spectrum with the real axis at high frequencies (100 kHz – 1MHz) on the Nyquist plot (Fig. 4.11). The resistance from the stainless steel electrodes is subtracted from the real impedance.

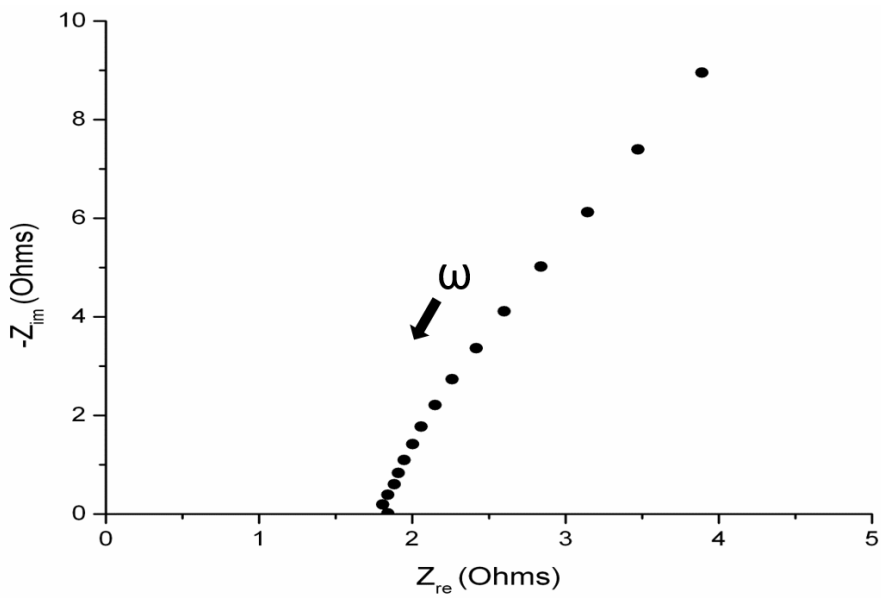

Figure 4.11. Typical Nyquist plot of the KOH saturated PAA electrolyte.

Figure 4.12 shows the conductivity as a function of KOH molarity used to saturate the PAA gel. A maximum conductivity is reached near 4-8M. The conductivity of the PAA gels is >60% of aqueous KOH solutions, which has a maximum reported ionic conductivity of ~0.6 S/cm at a room temperature. Furthermore, the conductivity of the saturated PAA separators is comparable to previously reported values for separators based on polyacrylic acid [28], [110]. Considering the excellent mechanical properties, this high conductivity shows that the PAA separator with PEO filler is able to achieve the high ionic conductivity required for an alkaline battery. A KOH molarity in the range of 5-8 M is optimal as this range attains the maximum conductivity.

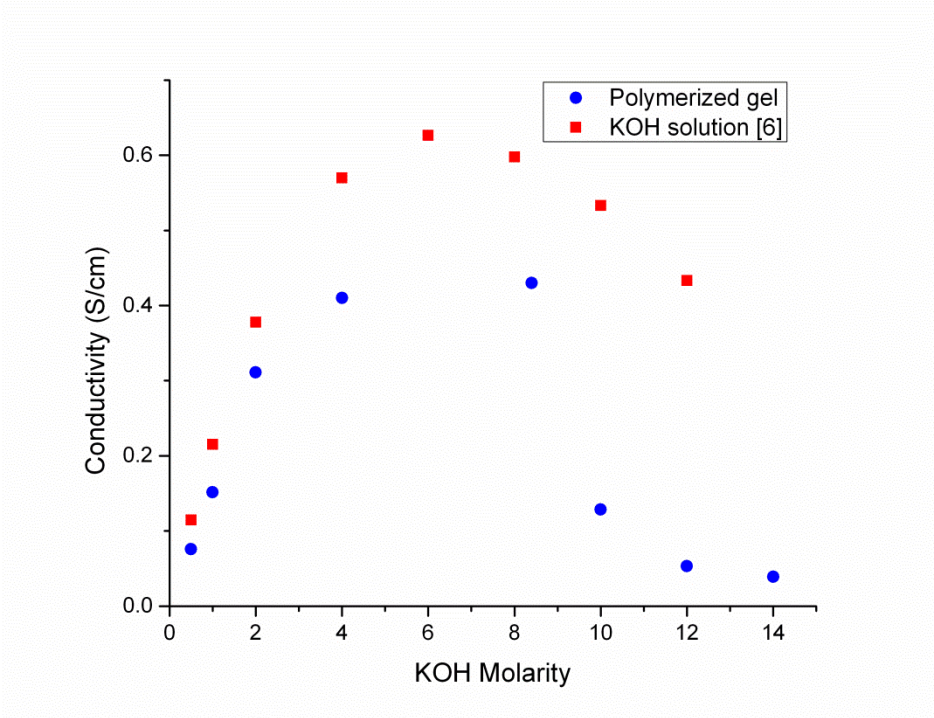

Figure 4.12 Ionic conductivity of polymerized PAA gel electrolyte saturated with the listed molarity KOH solution and the ionic conductivity of KOH solutions from literature.

4.2.6 Optimized alkaline separator

The developed PAA separator demonstrates high ionic conductivity and good mechanical stability (Table 4.1). The photoinitiator was added to give a mass loading of 0.5%. This value was chosen because the solubility of the photoinitiator, IRGACURE 2959, is limited to ~1% in water. We have fixed the crosslinker percentage to 1 wt% as lower concentrations did not lead to stable gel formulations, while higher crosslinking percentages (5-6 wt%) had solubility issues. Crosslinker concentrations between 2-4 wt% formed gels that contracted upon dehydration limiting their use in a printed battery stack. Acrylic acid was added to compose 7 wt% of the gel, as at higher percentages, the polymerized separator underwent massive swelling upon exposure to the KOH electrolyte. To increase the mechanical stability of the gel, a 2.5 wt% PEO filler was added to the solution. This imparts sufficient mechanical stability to the gel and while ensuring that the separator is still printable with a viscosity of 1,000 cP.

Material	Percentage
KOH solution (1 molar equivalent)	89 wt%
Acrylic acid	7.0 wt%
PEO filler	2.5 wt%
Crosslinker	1.0 wt%
Photoinitiator (IRGACURE 2959)	0.5 wt%

Table 4.1. Optimized PAA separator components.

The 2.5wt% PEO gel with the 7 wt% acrylic acid and 1 wt% crosslinker demonstrated that the PAA separator with PEO filler is able to achieve the high ionic conductivity required for an alkaline battery. For saturating the silver oxide batteries, we have chosen to use 8.4M KOH to maximize the ionic conductivity (Fig. 4.13) and minimize the swelling of the PAA gel (Fig. 4.11). Using this separator configuration, we have incorporated the PAA polymerized gel into the printed silver oxide battery. The PAA gel was polymerized directly on top of the printed zinc electrode with a stencil height of 300 µm. This gives a separator thickness of 200 µm as the printed zinc electrode has a thickness of ~100 µm.

4.3 Printed electrodes

In a vertically printed, silver oxide battery, there are two possible electrode configurations. One configuration is the zinc electrode as the bottom electrode and the silver oxide electrode as the top electrode. The reverse is to have the silver oxide electrode as the bottom electrode and the zinc electrode as the top electrode. Using the current PAA separator polymerization scheme, we polymerize the gel solution directly on to the bottom electrode. In order to do the polymerization, we need compatibility between the gel solution and the bottom electrode. The prepolymerized gel solution contains a photoinitiator that forms a free radical upon illumination. This free radical can interact with the electrode at the electrode/electrolyte interface. If the silver oxide electrode is the bottom electrode, the free radical formed (or growing polymer chain) is capable of reducing the silver oxide, causing a termination of the growing polymer chain or the free radical. PAA gel polymerized on top of the printed electrode leads to incomplete gel polymerizations. We have thus chosen to use the zinc electrode for the bottom electrode.

4.3.1 Printed zinc electrode

The stencil printed zinc electrodes were prepared by stencil printing a zinc slurry that consisted of a methylcellulose binder and zinc micron-sized particles (10 µm). The 5wt% binder solution was prepared by dissolving low viscosity methylcellulose in deionized water for at least 12 hours. Zinc metal was added to the slurry solution to give a ratio of 98:2 zinc to methylcellulose. The zinc electrode (and silver oxide electrode) were deposited to form silver oxide limited cells and gave a capacity ratio of 1:3-4 for Ag_2O:Zn. The zinc slurry was stencil printed using a stencil height of 300 µm (open area of 5x10 mm^2) on top of the Creative Materials silver current collector. The stencil was removed, and the electrodes were dried by placing them on a hot plate set at 40°C to remove the residual water. The dried, printed zinc electrodes had an average height of 100 µm.

The zinc electrodes were fabricated with a methylcellulose binder instead of the PVA binder used in Chapter 3 because of the increased stability of the zinc electrodes (with a methylcellulose binder) in neutral pH solutions. During the prepoymized gel separator deposition, the bottom electrode is directly exposed to the separator solution. This solution has a neutral pH. As the gel is deposited over the bottom electrode, it can fully dissolve the binder polymer if it is soluble in the gel solution. This is the case for the PVA binder. However, using a relatively high viscosity methylcellulose binder, we can minimize the amount of dissolution into the gel solution, as the binder dissolves slowly in neutral pH solutions. Although there may be

some dissolution of the zinc/binder into the electrolyte, the zinc electrode is deposited with excess capacity so the zinc electrode should not be the limiting capacity in the printed cell. The use of the methylcellulose binder allows for the gel separator solution to be printed and polymerized with minimal disturbance to the zinc electrode.

4.3.2 Printed silver oxide electrode

To deposit the top electrode, we have kept the same PVA binder to zinc electrode percentage, as these conditions gave high silver oxide utilizations in the planar printed batteries (Chapter 3).The silver oxide slurry was made by dissolving 0.025 grams of 99% hydrolyzed, M_w~89-98K PVA in 1 gram of DI H_2O. Then, the silver oxide was added to make the 98:2 weight ratio of Ag_2O to PVA slurry. This slurry was stirred for a minute to insure a uniform composition. The silver oxide slurry was stencil printed (300um stencil) upon the electrode followed by the silver flake/PEO slurry (400 um stencil). The final architecture allows for contact to be made to the bottom conductive adhesive and to the top silver flake adhesive (Fig. 4.13)

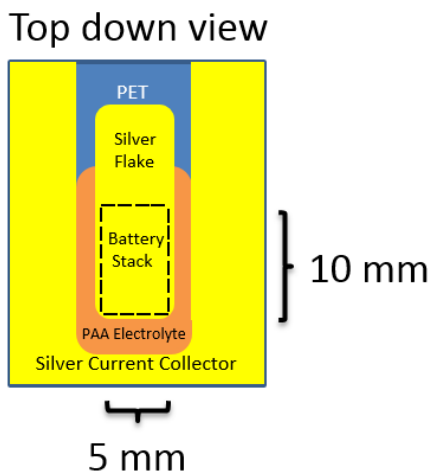

Figure 4.13 Top down view of the battery stack with a printed silver current collector deposited on top of the battery stack.

After printing all the layers, the battery was dehydrated for 30 minutes at 50°C. The dehydration step is required to remove the excess water from the battery and improve the electrode to current collector contact. The battery was rehydrated by placing the battery in zinc oxide saturated at 8.4 M KOH for 25 minutes. The saturation time was chosen based on the swelling experiments performed with PAA gel separator and the measured time to reach a stable open circuit voltage. Incomplete battery saturation results in an unstable open circuit voltage or discharge potential and a drop in percent utilization.

The entire process flow for the fabrication process is illustrated in Figure 4.14 illustrating the different procedures mentioned in this chapter. The fabricated batteries were laminated in PVC pouches for testing after saturation in 8.4M KOH. The batteries were discharged using custom built galvanostat [124] or characterized with Gamry Reference 600.

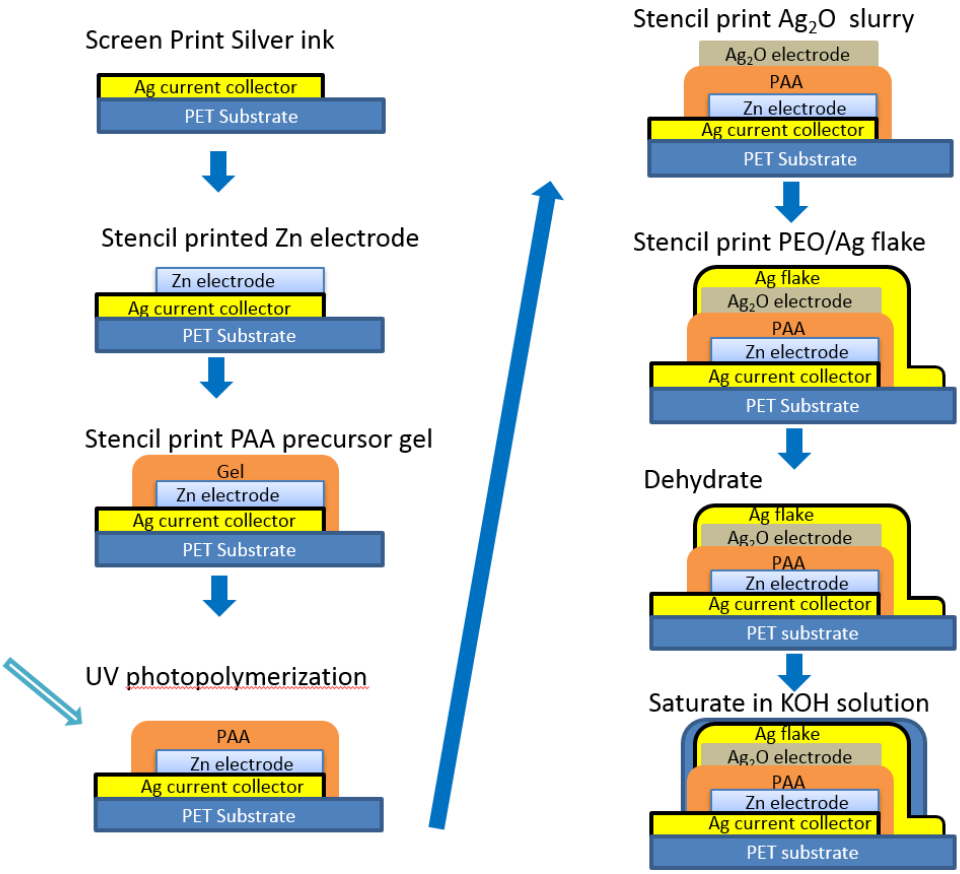

Figure 4.14 Printed battery process flow for vertical architecture.

4.4 Discharge performance

The fabricated batteries, upon saturation with 8.4 M KOH, demonstrate an open circuit potential of ~1.54-1.55 V. The batteries were discharged at 2C, C and C/2 rates with respect to the silver oxide capacity. The printed, silver oxide battery exhibits high discharge capacity even at high rates of discharge (2C rates) (Fig. 4.15). At higher discharge rates, we see a decrease in potential likely due to an increase in over potential at the electrode interface and a greater contribution of the voltage drop due to the ohmic resistance of the battery. Further studies with electrochemical impedance spectroscopy are required in the future to examine the reactions at the electrode interface and to quantify the discharge phenomena (Chapter 6). The batteries achieve high silver oxide utilization with utilizations between 90 and 100 percent of the deposited silver oxide. Complete silver oxide reduction is unlikely for two reasons. First, there is some reduction of the silver oxide by a polyvinyl alcohol binder in basic solutions. Second, during discharge, there is likely a loss of electrical contact to some of the particles of silver oxide due to the shape change of the electrode during discharge.

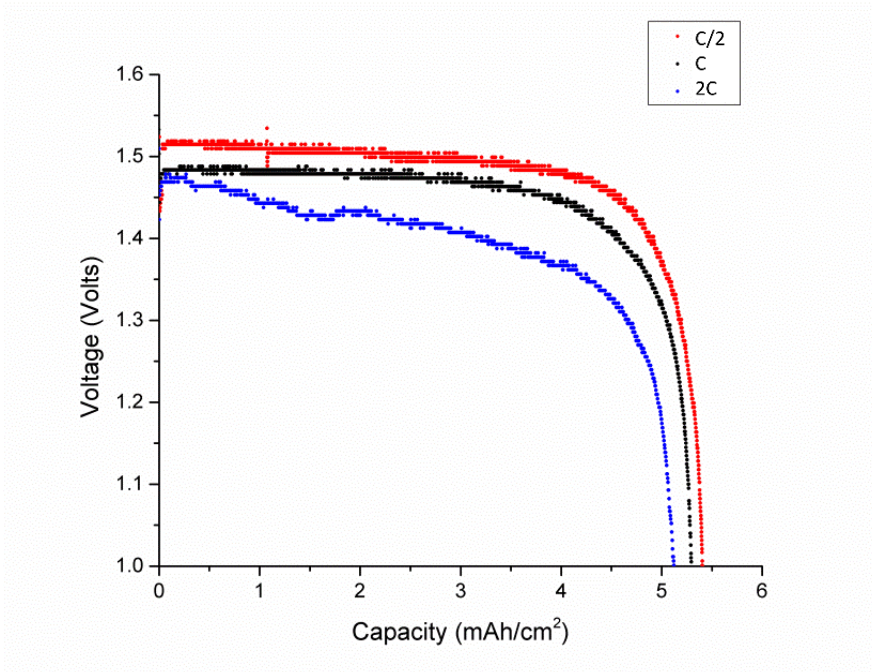

Figure 4.15 Printed silver oxide battery discharge curves at different discharge rates with respect to the limiting silver oxide capacity (C/2, C and 2C rates).

The printed batteries also demonstrate good performance under flexing, attesting to their viability for use in flexible electronics applications (Fig. 4.16). The fabricated batteries were tested under flexion by placing the batteries under curvatures of 1.0 cm and 1.5 cm. The percentage of silver oxide utilized is greater than 90%, and the variability is within the experimental uncertainty of the measurement. Noticeably, the discharge potential remains constant with increasing bend radius, indicating the tested bend radius does not disturb battery performance. Previously, it has been shown that printed batteries under flexion demonstrate increased performance due to interfacial contact [28]. The high performance of our printed batteries demonstrates good interfacial contact.

The capacity of the demonstrated printed silver oxide battery is ~5.4 mAhr cm^{-2} at a C/2 discharge rate of 2.75 mA cm^{-2}. This value is comparable or better than the reported areal capacities of other printed batteries in the literature [28]. Another important figure of merit to take into consideration is the energy density. For example, the areal capacity specifications of a printed battery could be increased arbitrarily by depositing thicker layers, though this will obviously detract from flexibility and deployability in real thin film system applications. This will result in a greatly increased areal capacity, while volumetric energy density will stay largely unchanged. For the developed printed silver oxide battery, we report a volumetric capacity of 7.1 mAhr cm^{-3} and volumetric energy density of 10 mWhr cm^{-3} while maintaining an overall thin battery stack and good mechanical flexibility; note that volumetric energy densities are not reported for many of the aforementioned literature cells, so a direct comparison is not possible. These values are important to quantify and compare across different chemistries and battery geometries.

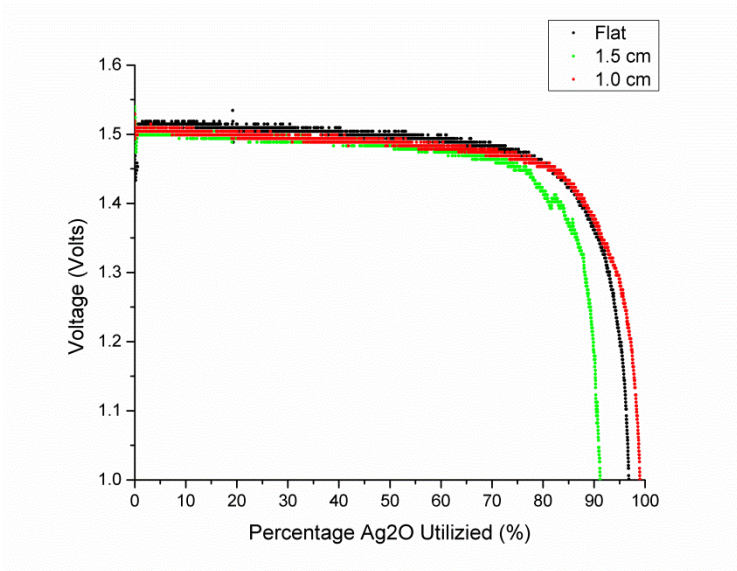

Figure 4.16 Discharge performance of printed silver oxide battery under flexing (discharge at C/2 rate).

Even higher densities are certainly achievable in the future. The active material consisting of the silver oxide and zinc electrodes contributes a small fraction (28 wt%) of the material components of the printed battery (Figure 4.17). Optimizing the cell design, for example, by decreasing the separator thickness and reducing the zinc to silver oxide ratio could further increase the energy density. The electrode composition could also be modified by utilizing divalent silver oxide (AgO) which has a theoretical capacity of 432 mAh g^{-1} instead of monovalent silver oxide (Ag_2O) which has a capacity of 231 mAh g^{-1}. This will not only increase the capacity, but also increase the open circuit voltage to 1.8V due to the higher reduction potential of AgO, resulting in a further increase in energy density.

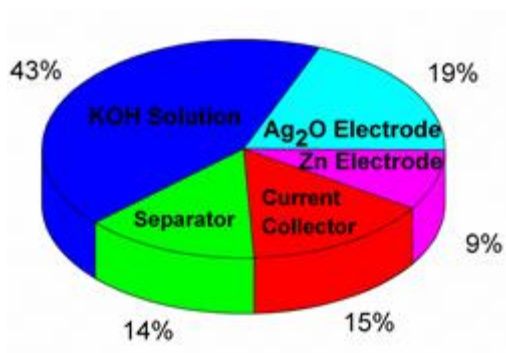

Figure 4.17 Distribution of battery components by weight for the printed silver oxide battery.

4.5 Conclusion

We have demonstrated the development of a high ionic conductivity, photopolymerizable alkaline separator based on polyacrylic acid. This separator demonstrates good mechanical

stability and ionic conductivities on the order of 0.4 S/cm. The polyacrylic acid separator may be used with other alkaline chemistries beyond that demonstrated herein, and indeed, may also be useful in any application requiring hydrogels, such as tissue engineering [21], [22]. Using the synthesized PAA separator, we have demonstrated a stencil printed silver oxide battery with areal capacities of 5.4 mAhr/cm^2 and volumetric capacities of 7.1 mAhr cm^{-3}. The batteries show no difference in discharge upon flexing at a bend radius of 1.0 cm, indicating their potential in flexible applications. The processes developed are scalable to large scale manufacturing and allow for customization to the application. The demonstrated flexible, high energy density, stencil printed battery has the potential to be useful in many flexible and printed devices and applications.

Chapter 5. Battery Characterization

Understanding the phenomena that occur in a battery is important to designing a high utilization battery with low internal resistance. This will enable a high energy density battery capable of meeting the demands of printed electronics. Characterization of the printed silver oxide battery developed herein was performed by measuring the polarization curve. Additionally, electrochemical impedance spectroscopy (EIS) of the printed battery was conducted in the two electrode configuration and the three electrode configuration with a pseudo-reference electrode. Using the Randles circuit model to model the electrode phenomena at the silver oxide and zinc electrode, we extracted parameters from the EIS spectra. These values are then applied to the polarization curve to explain the observed discharge voltage.

5.1 Polarization curve

We characterized the performance of our printed battery by performing a polarization curve measurement to determine the discharge potential at different current densities (Fig. 5.1). The polarization curve measurement was performed with a Gamry 600 potentiostat. A range of current values of up to 30 mA were used, and the discharge potential was recorded for 5 seconds. The potential was allowed to recover for 15 seconds before the next discharge current was applied. This allows the concentration of the zincate and hydroxide ions to equilibrate. The average voltage value during the discharge period was used to provide points for the polarization curve.

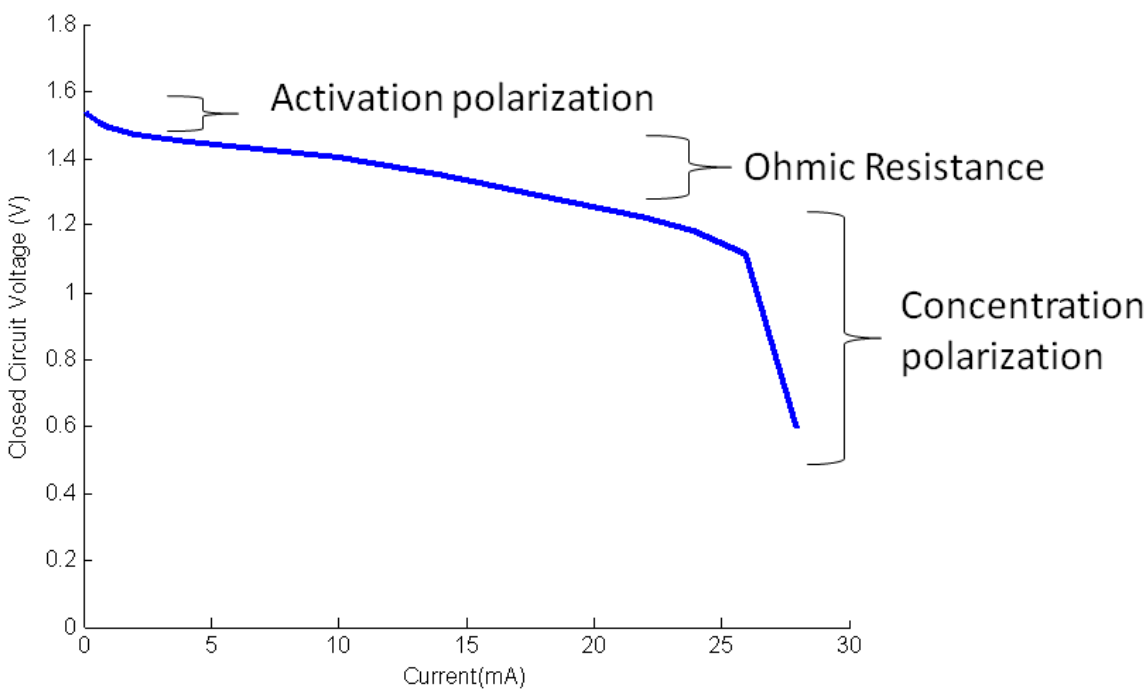

Figure 5.1 Polarization curve of a printed silver oxide battery.

Using this curve, we can predict the expected voltage for a given discharge current. The potential may change for an extended discharge period, especially for larger current densities; however, the polarization curve allows us to estimate the expected voltage. Furthermore, we see different regimes in the polarization curve: activation polarization, ohmic resistance and concentration polarization. During discharge all three phenomena are occurring in the cell, however at different current densities, one phenomena may be more dominate. The different regimes listed in Figure 5.1 are general descriptions for the phenomena that are occurring during discharge. The activation polarization and ohmic resistance will be quantified in this chapter.

The initial drop low current densities are attributed to the activation polarization or the overpotential for the chemical reaction to occur [29]. Both electrodes will have an overpotential term associated with them, and the combination of these two overpotential terms give the initial potential drop. The overpotential is given by the Butler-Volmer equation, which relates the electrical current on an electrode to the electrode/electrolyte potential:

$$j = j_0 \left(exp\left[\frac{\propto_a nF\eta}{RT}\right] - exp\left[-\frac{\propto_c nF\eta}{RT}\right]\right)$$

where j_0 is the exchange current density, α_a and α_c are the anodic and cathodic charge transfer coefficients, respectively, η is the activation overpotential, R is the universal gas constant, F is the Faraday constant, and n is the number of electrons in the reaction.

For small voltage perturbations, we can use the Tayler expansion series to rewrite the above equation as:

$$j = j_0 \frac{(\propto_a + \propto_c)nF}{RT}\eta = j_0 \frac{nF}{RT}\eta$$

We can now rewrite this equation in terms of the defined variable, R_{ct}, the charge transfer resistance:

$$R_{ct} = \frac{\eta}{j} = \frac{RT}{j_0 nF}$$

This resistance value is a measure of the activation overpotential at low current densities. Ideally, for a high energy density battery, we would like to have as low of a charge transfer resistance as possible. Equivalently, this means we would have as high of an exchange current density as possible. However, this will be limited by the chemistry as the exchange current density is given by:

$$j_0 = nF\ k_0 C_{ox}^{1-\beta} C_{red}^{\beta}$$

where n is the number of electrons in the reaction, F is the Faraday constant, k_0 is the reaction constant, C_{ox} is the concentration of the oxidized species, and C_{red} is the concentration of the reduced species.

The ohmic potential drop is due to the resistance of the electrolyte, current collector, leads and clips and electrode material. This impedance should be independent of the frequency in the frequency range we are considering (10 mHz to 1 MHz). The Ohmic resistance may change over time as the electrode composition changes. For example, the resistance of the silver oxide electrode may drop as the electrode is converted from silver oxide to silver.

The concentration overpotential is due to mass transport issues in the cell. In this case, the electrolyte cannot supply hydroxide ions quick enough to the silver oxide battery for discharge to occur. The concentration potential can be written as [29]:

$$\eta = (1 - t_{+})\frac{RT}{F}\ln\frac{c_I}{c_{II}} + \int_0^{bulk}\left(\frac{1}{k} - \frac{1}{k_{bulk}}\right) i_y dy$$

This overpotential term includes the two effects associated with a concentration difference: a potential term related to the concentration gradient and an Ohmic term related to the difference in concentration. If the current is reduced to zero, the Ohmic term becomes zero , leaving only the potential term due the concentration gradient.

We would like to be able to measure these various potential drops during the discharge of the printed battery. Once we know what the different potential drops correspond to, we can then use this information to design a better battery. We use a technique called electrochemical impedance spectroscopy (EIS) to measure the impedance of the battery as a function of frequency. We then fit the data with physically based models that represent the structure and reactions occurring at the electrode surface. Using EIS, we are able to extract charge transfer resistance and the ohmic resistance of the battery stack. These values can then be used to explain the potential drops observed in the polarization curve.

5.2 Electrochemical impedance spectroscopy (EIS)

Electrochemical impedance spectroscopy (EIS) is a powerful technique that is used to characterize electrode interferences. Determining the chemical reactions at the electrodes as a function of discharge is important to understanding the reactions at the electrode surface. Two electrode measurements are convoluted from the fact that both interfaces of the electrodes are being measured. However, the addition of a third reference electrode is one way to separate the two electrodes and characterize what is happening at each electrode interface. Ideally, the third electrode is a non-polarizable reference electrode that has a stable potential [101]. The typical setup is demonstrated in Figure 6.1. The experimental setup consists of three electrodes, a working electrode, a counter electrode and a reference electrode.

The reference electrode should be as close to the surface as possible to minimize the electrolyte resistance. To achieve this, the reference electrode is placed near the electrode surface by the use of a Luggin capillary. Luggin capillaries are narrow tips of plastic or glass that bring the reference electrode in close contact with the solution near the working electrode (Fig. 5.2). However, using a Luggin capillary to get an accurate measurement of the phenomena occurring in a thin film battery is difficult to accomplish. Instead of using a bulky reference

electrode, we decided to use a pseudo-reference electrode instead. We demonstrated a zinc wire pseudo-reference electrode placed in between two PAA separator layers.

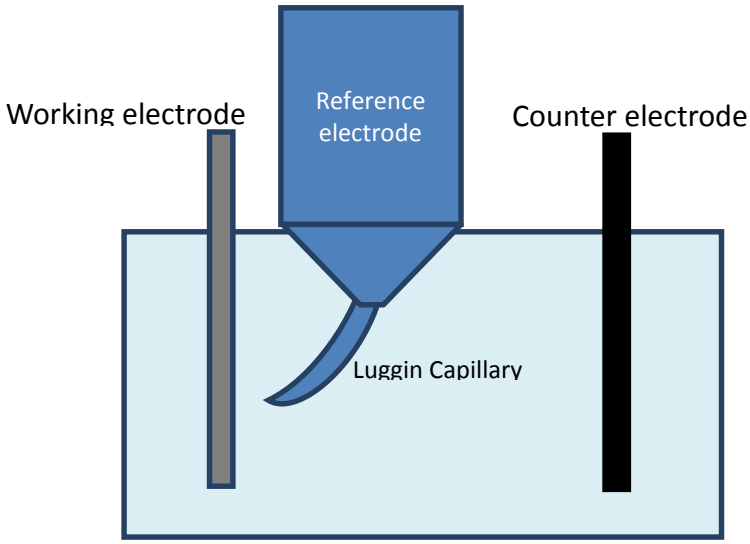

Figure 5.2 Electrochemical impedance spectroscopy (EIS) setup to monitor the working phenomena at the electrode/electrolyte interface.

The ideal reference electrode should have zero impedance, be in thermodynamic equilibrium, have a reversible reaction and have a standard well defined potential. There are numerous reference electrodes that fulfill these qualifications, such as the standard hydrogen electrode (SHE), the standard calomel electrode (SCE) and the Ag/AgCl electrode [125]. The reference electrode used depends on the experimental setup conditions, such as solution species and pH. However, for a small battery, it is difficult to work with large commercial reference electrodes. Pseudo-reference electrodes are one way of being able to measure the potential of the battery electrodes in situ.

Unlike reference electrodes which are in thermodynamic equilibrium, pseudo-reference electrodes are typically not at thermodynamic equilibrium. The advantages of pseudo-reference electrodes are their simplicity, lack of liquid junctions and low potential for contamination [101]. Pseudo-reference electrodes have been made with silver, gold and Ag/AgCl wire. In corrosive systems, pseudo-reference electrodes are often made of similar materials to the working electrode. This minimizes the effect of corrosion. If a corrosive process occurs at the working electrode and pseudo-reference electrode, the corrosion rate should be similar, leading to similar potentials in both electrodes and low electrode/electrolyte impedance.

Pseudo-reference electrodes have been used in various systems to measure cathode and anode voltage potentials and their electrode impedances and to determine capacity fading in lithium-ion cells. [126] We used a zinc wire pseudo-reference electrode to monitor discharge potentials, open circuit potentials and reactions at each individual electrode.

We performed EIS with a two electrode configuration to examine the whole battery impedance and a three electrode EIS using a zinc pseudo-reference wire electrode. We analyzed

the gel electrolyte between two printed Creative Materials current collectors. This allows us to analyze the system without the presence of the zinc and silver oxide electrodes.

5.3 EIS modeling

A proper model is needed to extract accurate measurement of the battery properties. To provide an accurate model, we look at various cases related to the silver oxide battery in question. First, we looked at the simple systems consisting of conductive electrodes and partially polarizable electrodes.

5.3.1 Conductive electrodes

In Figure 5.3A, we have the simple case of an electrolyte medium between two flat electrodes. In the simple case where faradic reactions are fast, or if we have non-polarizable, conductive electrodes, then, we can assume that the charge transfer resistance is small. The overall impedance of this system can be represented as the parallel contribution of a resistor with a resistance corresponding to the electrolyte ionic conductivity and a capacitance related to the geometric capacitance of the parallel plate system (Fig. 5.4B). The impedance of this configuration is given by:

$$Z = \frac{R\frac{1}{j\omega C}}{R + \frac{1}{j\omega C}}$$

The Nyquist plot of $-Z_{im}$ vs Z_{re} is shown in Figure 5.3C which shows a semicircle that crosses the real axis at the impedance value of Z_{re} = R for very low frequencies ($\omega \rightarrow 0$) and Z_{re} = 0 for high frequencies ($\omega \rightarrow \infty$).

The capacitance per area, C, is defined by ε/L, where ε is the permittivity of the electrolyte, and L is the separation distance between the two plates. The permittivity of an alkaline solution is going to have a dependence on the ions in the solution due to change in the dipole interactions with the KOH. For a KOH molar concentrations of 3.22 mol/kg, the permittivity of the solution is 46.6. This is much lower compared to a permittivity of ~80 for water. Assuming a dielectric permittivity of 46 and a 5x10 mm^2 area capacitor with separation distance of 120 µm, we calculated a capacitance of 0.34 nF/cm^2 or 0.17 nF for the specific area. The conductivity of the PAA gel electrolyte was measured to be approximately 0.4 S/cm (Chapter 4). The calculated resistance of the 120 µm PAA gel should be 0.06 Ω. The time constant for the system of a resistor and a capacitor in parallel is given by:

$$\tau = RC$$

For the PAA gel electrolyte system, we calculated a time constant of 10 femtoseconds, which corresponds to a frequency of 100 GHz. This frequency is well beyond the instrumentation frequency (1mHz to 1MHz). Thus, the semicircle in the ideal representation of the Nyquist plot is not seen (Fig. 5.3)

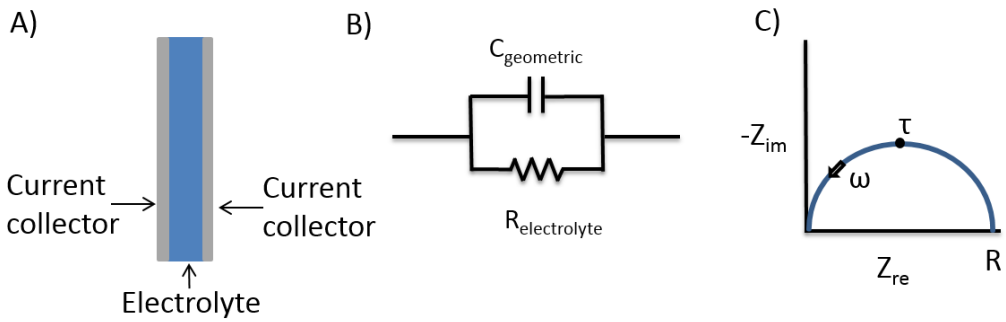

Figure 5.3 A) EIS cell consisting of an electrolyte between two Creative Materials silver current collectors. B) Equivalent circuit representation. C) Nyquist plot of an ideal circuit representation of a capacitor and resistor in series.

5.3.2 Partially polarizable electrodes

Now, we consider what happens if we have partially polarizable electrodes. If we place a conductive sheet in an electrolyte, ions are going to stick to the surface of the electrode. The ions at the surface are going to induce the opposite charge in the electrode interface. This layer of absorbed ions and solvent molecules forms what is known as the inner Helmholtz plane (IHP) which is defined as the position of the centers of ions or molecules that have absorbed at the surface of the electrode (Fig. 5.4). This separation distance is on the order of Angstroms [127]. In addition to the IHP, there is also the outer Helmholtz plane (OHP) which consists of the plane of the centers of the solvated ions that are closest to the surface of the electrode. Next to the outer Helmholtz plane is a diffuse layer that consists of anions and cations distributed in the electrode. The summation of the total charge in the electrode: the IHP, OHP and the diffuse layer is zero. By applying a bias, we are effectively charging a capacitor. The formation of ions on the electrode leads to what is known as the double layer capacitance.

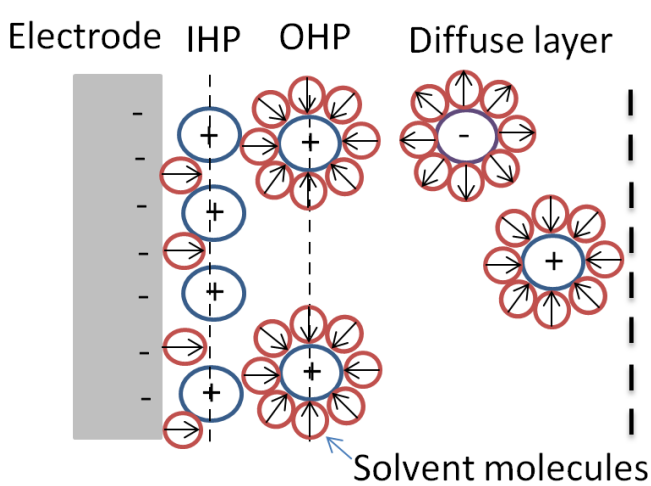

Figure 5.4 Electrochemical double layer that forms when a negative potential is applied to an electrode immersed in an electrolyte solution.

The double layer capacitance associated with this layer is given by:

$$C = \left(\frac{dq}{dU}\right)_{\mu,T}$$

The capacitance can be measured directly by application of a rectangular current form or a small sinusoidally varying potential [128], [129]. It can also be extracted by using electrochemical impedance spectroscopy and fitting the data with a model that contains a double layer capacitance.

For zinc and silver oxide electrodes, the double layer capacitance has been measured directly. There are slight variations in the value of the double layer capacitance as it depends on the electrolyte concentration, additives to the solution, the potential of the electrode and surface species on the electrode [29]. The measurement of a double layer capacitance can also change the electrode surface, resulting in a change in the double layer capacitance. Despite these problems, zinc and silver oxide electrodes have had reliable measurements of the double layer capacitance. Zinc electrodes have demonstrated a double layer capacitance of 50-400 μF cm^{-2} depending on the electrode material and electrolyte concentration [129]. Silver oxide electrodes have demonstrated double layer capacitances of 40-80 μF cm^{-2} depending on the electrolyte concentration and the electrode preparation [130].

In addition to the electrode polarization, we can also have a faradic reaction occurring at the surface of the electrode. This reaction can be written generally as:

$$Ox + ne^- \Leftrightarrow Red$$

This charge transfer reaction utilizes electrons that are supplied by or donated to the electrode. The speed of the reaction depends on the temperature, the concentration of the reaction products, the electrode potential and the reaction rate [127]. The relation between the current and the potential is given by the Butler-Volmer equation:

$$j = j_0\left(exp\left[\frac{\propto_a nF\eta}{RT}\right] - exp\left[-\frac{\propto_c nF\eta}{RT}\right]\right)$$

This equation can be simplified for small overpotentials to:

$$R_{ct} = \frac{\eta}{j} = \frac{RT}{j_0 nF}$$

The combination of these two phenomena is represented by a capacitance and resistance in parallel (Fig. 5.5B). This element combines with the previously mentioned circuit element to give a Nyquist plot with two time constants (Fig. 5.5C). Typically, the first time constant is not seen do the limitation in frequency range.

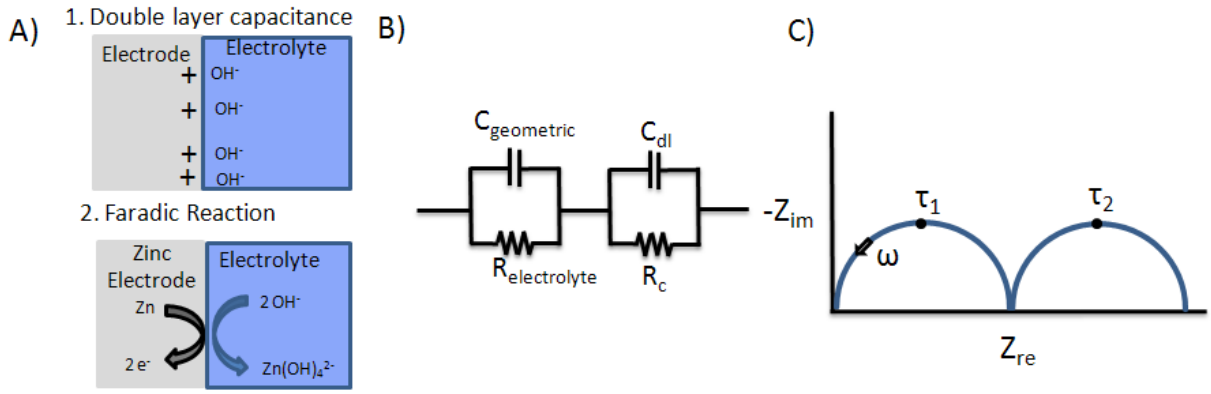

Figure 5.5 A) Diagram illustrating two electrode phenomena occurring at the zinc electrode/electrolyte interface. B) Equivalent circuit showing the parallel contribution of the double layer capacitance and charge transfer resistance. C) Nyquist plot for the two time constant equivalent circuit shown in B).

5.4 Impedance spectroscopy of a PAA electrolyte

We would like to use EIS to understand the reaction phenomena associated with the two electrodes of the zinc-silver oxide battery. However, to simplify our system, we first characterized a cell that consisted of a KOH saturated PAA separator between two current collectors. This configuration lacks the silver oxide and zinc electrodes, so ideally, no faradic reactions should be involved. This allows us to observe the interaction of the PAA electrolyte with the printed silver current collectors. In this case, the charge transfer resistance would be infinite or a very large value. We looked at three different current collectors: a printed Creative Materials current collector, a stainless steel collector and an evaporated gold current collector. The current collector was changed to identify the effect that the printed current collector has on the impedance spectra.

5.4.1 Experimental setup

The electrochemical cell was made by placing a KOH saturated PAA gel between two printed Creative Materials silver ink current collectors (Fig. 5.3A). The polymerized gel had a thickness of 300 µm and an area of 10x10 mm^2. The polymerized PAA gel was saturated with 8.4 M KOH before measurement. Electrochemical impedance spectroscopy was performed with a Gamry 600 potentiostat. An AC voltage stimulus was used with a 4 mV RMS signal. The frequency of measurement was scanned from 1 MHz to 10 mHz.

5.4.2 Measurement results and discussion

We see a significant difference in the impedance spectrum of the printed Creative Materials current collector and the evaporated gold and stainless steel current collectors (Fig. 5.6). The evaporated gold and evaporated stainless steel current collectors behaved as expected with an electrolyte resistance in series with a parallel contribution of a double layer capacitance and large charge transfer resistance, i.e. equivalent to a 1 time constant system. The printed

electrode showed an interesting impendence spectrum with a slowly increasing magnitude from the frequency 10 kHz to 10 Hz. This effect has been observed before in electrochemical capacitors and is attributed to porous electrodes that do not behave as a flat surface [131].

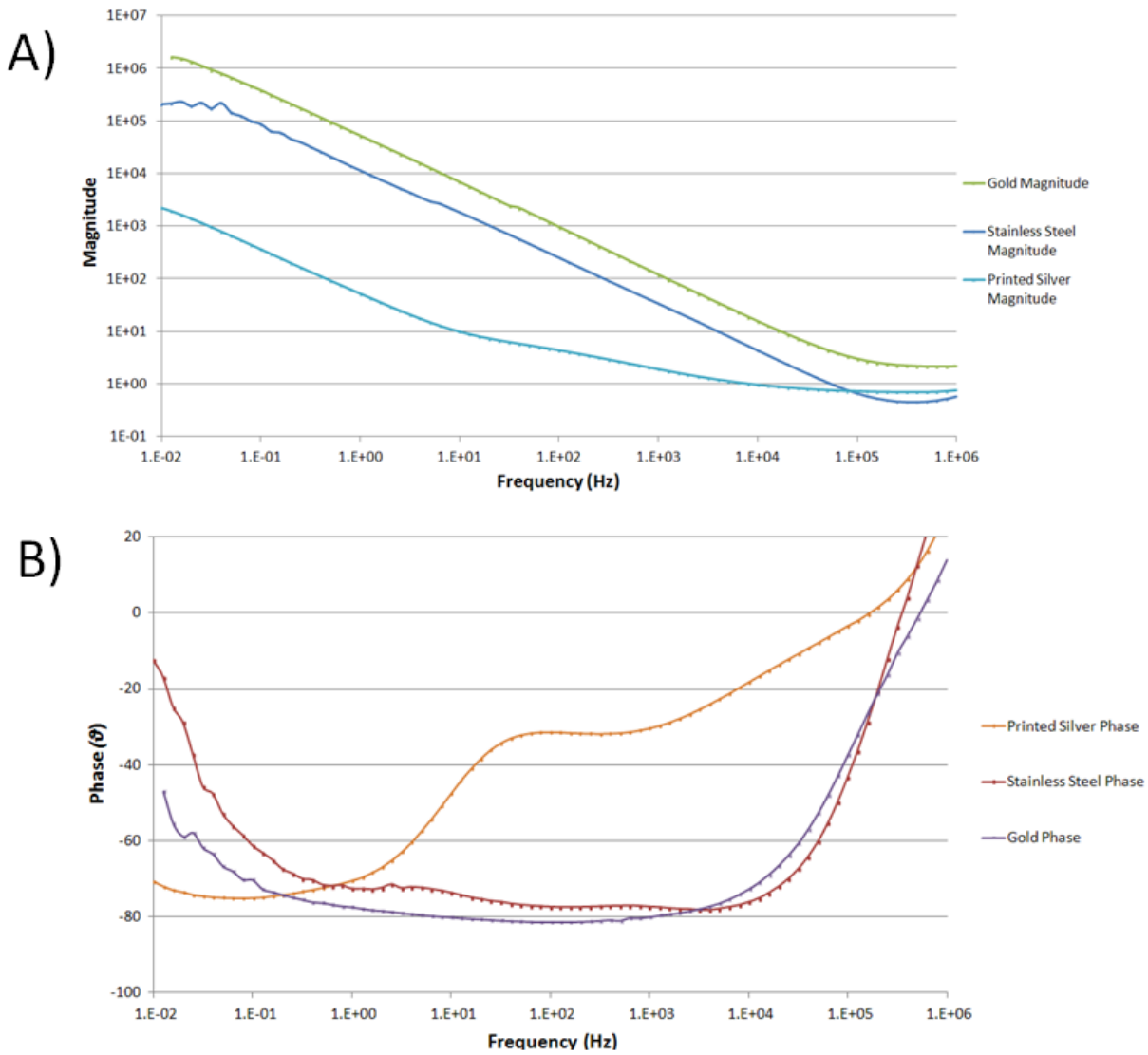

Fig 5.6 Bode plot information showing the A) magnitude and B) phase information of the impedance spectrum for a PAA gel electrolyte with different current collectors.

The physical structure of the printed Creative Materials current collector does exhibit a porous structure. The printed electrode does not behave as a flat conductor; rather, it is a relatively thick (30 µm) porous conductor that consists of silver flakes held together with a polymer binder. The SEM micrograph of the surface of the printed Creative Materials current collector shows a rough surface with pores throughout the material (Fig. 5.7). This structure gives support for the porous electrode explanation above.

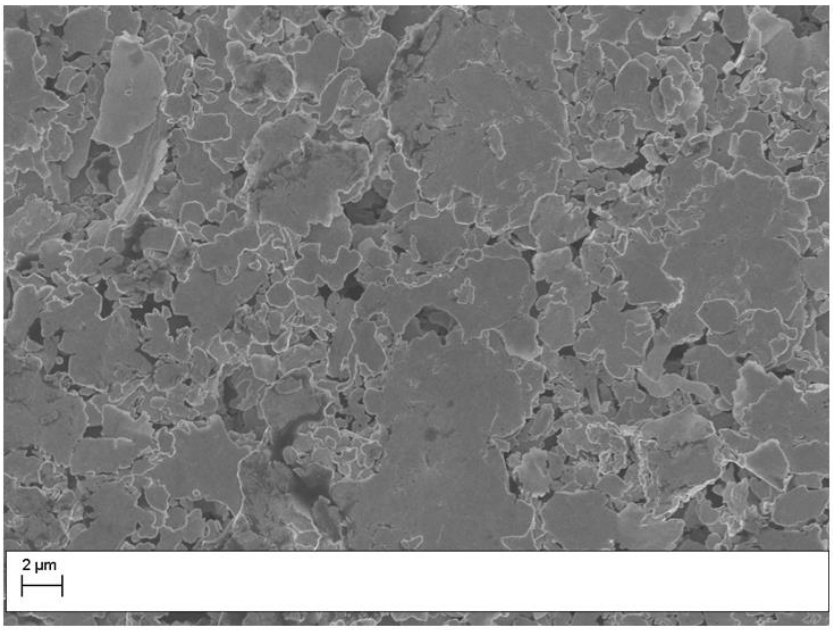

Figure 5.7 SEM micrograph of a printed Creative Materials silver current collector.

If the electrodes are not smooth, but rather rough or porous, we can improve the model for the measured impedance and not use the model consisting of a resistor and capacitor in parallel. Specifically, we can treat the impedance as a transmission line of parallel circuit elements of charge transfer resistances and a double layer capacitance (Fig. 5.8). This transmission line model is also known as the Bisquert open model [132].

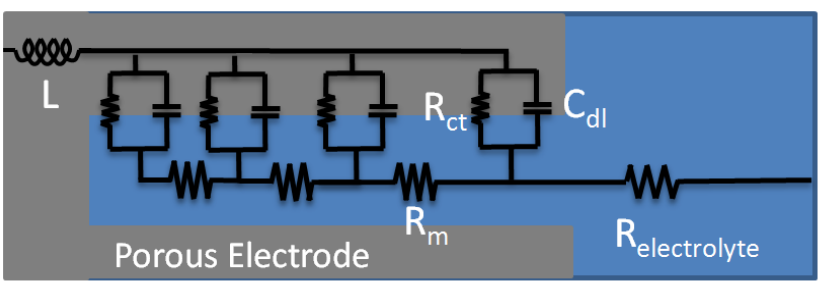

Fig 5.8 Diagram of the Bisquert open model applied to a porous electrode.

It can be shown that the impedance of a porous electrode can be written as [127]:

$$Z = \sqrt{(\zeta \times R_m)} \coth\left(L\sqrt{\frac{R_m}{\zeta}}\right) + R_{electrolyte} + i\omega L_{in}$$

where ζ is the parallel combination of R_{ct} and C_{dl}, R_m is the solution pore resistance, $R_{electrolyte}$ is the electrolyte resistance, L_{in} is the parasitic inductance, and L is the length of the pore. L essentially represents the length of the transmission line. We model the double layer capacitance

as a complex phase element that has the impedance Z= 1/((i ω)^a Y). We are neglecting the resistance of the electrode because we assume that the conductivity is higher than the solution resistance in the pore. Once the fitting is done, the characteristic impedance of the sample can be found, i.e. the values ζ/L and R_m/L .

Fitting the data with the Bisquert open model gives a good fit with the experimental data. Fitting of the experimental data was done using the Simplex method provided by the Gamry Echem Analyst software using a maximum of 300 iterations. An improved fit could be accomplished by measuring the cell impedance at lower frequencies. The large inductance at high frequencies also masks the phenomena associated with cell structure. Reducing the electrode size and optimizing the cell contact to the potentiostat would improve the data and potentially allow for a more accurate fit.

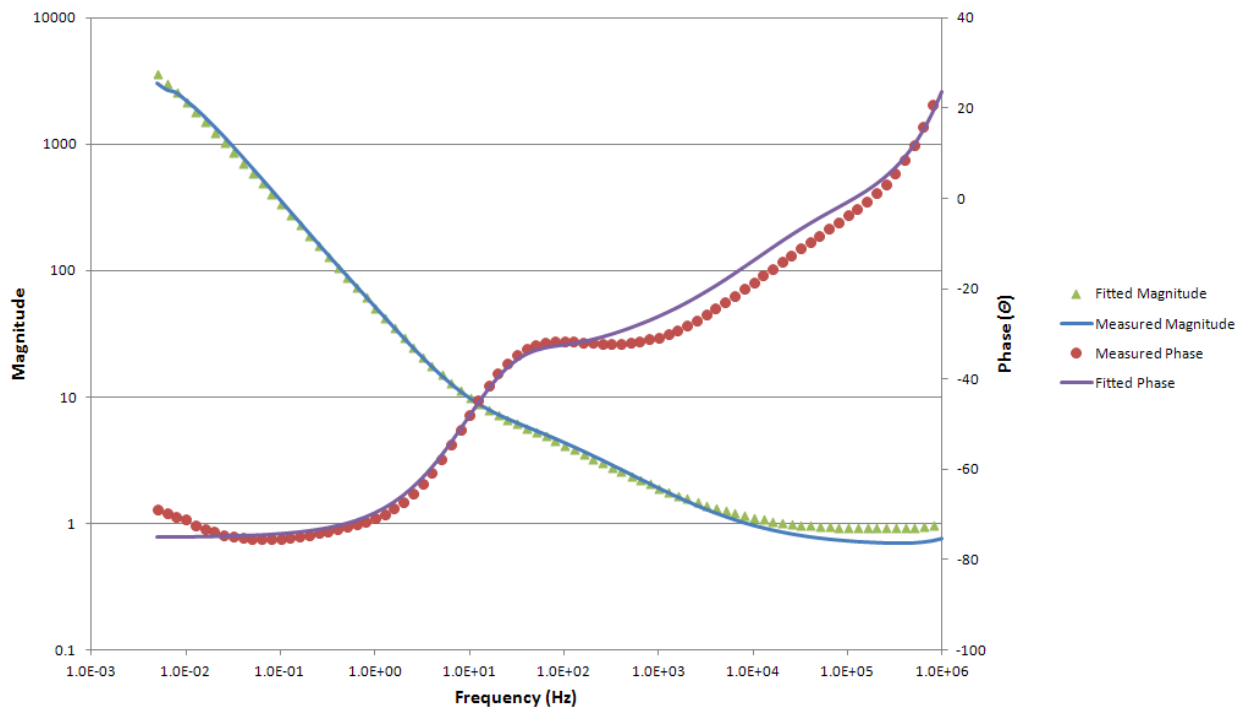

Figure 5.9 Nyquist plot for the printed PAA gel electrolyte with the Creative Materials printed conductor. The fitting was done using the Bisquert open model developed in Figure 5.8.

From the extracted parameters, we can calculate what the double layer capacitance is for the printed Creative Materials silver current collector. Using the admittance value calculated from the data, we calculate that the double layer capacitance is 22 µm cm^{-2} (Table 1). This falls in the range of literature values reported for silver electrodes [130]. From the impedance data, we see that the electrolyte resistance is 0.5 ohm (Table 5.1). This low resistance is ideal for a printed battery. We would like to have this resistance value to be small as possible to minimize the voltage drop during discharge.

Parameter	Extracted Value
L	0.070
R_m (ohm)	193
R_{ct} (ohm)	1390
Y_m (S*s^a)	0.062
A	0.840
$R_{electrolyte}$ (ohm)	0.56
L_{in} (H)	66e-9

Table 5.1. Extracted values for the electrode fit.

Now that we have characterized the PAA gel electrolyte between the two printed silver oxide electrodes, we can look at the case with the zinc electrode and silver oxide electrode. The structure will not be exactly the same as we will replace one of the printed Creative Materials printed electrodes with a silver/PEO flake current collector. The addition of the zinc electrodes will cause a significant change in the impedance because now we will have a faradic reaction occurring at the electrode/electrolyte interface. The porous nature of the printed current collector may also influence the impedance measurements of the zinc and silver oxide electrodes, since the zinc or silver oxide electrode will be in series with the current collector. The measured impedance should be dominated by the impedance of the electrode, but to get a more accurate model for the impedance, it may be desirable to include the possible contribution from the current collector into the model.

5.5 EIS: Three-electrode measurement

The three-electrode measurement is more complex than the two electrode impedance measurements with the PAA gel separator. Now, we have introduced two active electrodes to the printed silver current collectors: the silver oxide electrode and the zinc electrode. To measure the electrode properties, we used a zinc reference electrode placed between the two electrodes. This allows for the independent measurement of the impedance of each electrode. Using this technique, we extracted the charge transfer resistance associated with each electrode. This provides important information regarding the battery performance and provides insight into optimization strategies for the overall battery structure.

5.5.1 Experimental setup

The three electrode setup is fabricated by placing a zinc wire (150 µm) on top of the polymerized PAA gel electrolyte that has been polymerized on top of a zinc electrode using the standard fabrication process (Chapter 4). Then, a second polymerized gel electrolyte layer (thickness 200 µm) is placed on top of the reference electrode (Fig. 5.10). A thick PAA separator layer was used to minimize the possibility of shorting in the battery. The silver oxide electrode and silver PEO current collector are printed on this second layer. The separator in this experimental setup is effectively twice as thick as the standard electrolyte. However, since the conductivity of the separator layer is high, doubling the thickness of this layer should not have a major effect on the impedance of the battery.

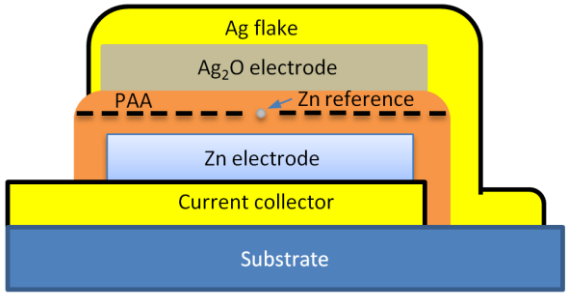

Figure 5.10 Cross-section of a printed battery with a zinc pseudo-reference electrode (not to scale).

Electrochemical impedance spectroscopy was performed with a Gamry 600 potentiostat. An AC voltage stimulus was used with a 4 mV RMS signal. The frequency of measurement was scanned from 1 MHz to 10 mHz. The measurement was done with 5 data points per magnitude of frequency.

5.5.2 Measurement results and discussion

The EIS spectra from the three electrode setup shows that the pseudo-reference electrode is a stable pseudo-reference electrode. It is stable in the sense that the sum of the two individual electrodes is approximately equal to the whole cell impedance within the uncertainty of the measurement (Fig 5.11) The potential of the reference electrode may change over time due to corrosion of the zinc electrode. However, for the period of the measurement, the electrode potential appears to be constant as evident from the Nyquist plot. To get an accurate measurement of the electrode potential requires a calibration with a known reference electrode such as a Hg/HgO reference electrode; however, the consistency in the data is clear indication that the chosen electrode herein is stable over the course of the measurements performed. There are slight deviations in the curves that could be attributed to differences in how the clips are contacted to the current collectors or due to settling of the electrolyte concentrations to equilibrium over time.

We see a significant difference in the Bode plot for the silver oxide and zinc electrodes (Fig. 5.12). At high frequencies, the magnitude is roughly half of the total impedance. This is what is expected as the zinc pseudo-reference electrode is placed between the two electrodes (Fig. 10). There is also a difference in the phase plots. The zinc electrode has a larger inductive effective effect at low frequency. This could possibly be due to the larger current collector area of the silver electrode which forms the base for the entire battery stack.

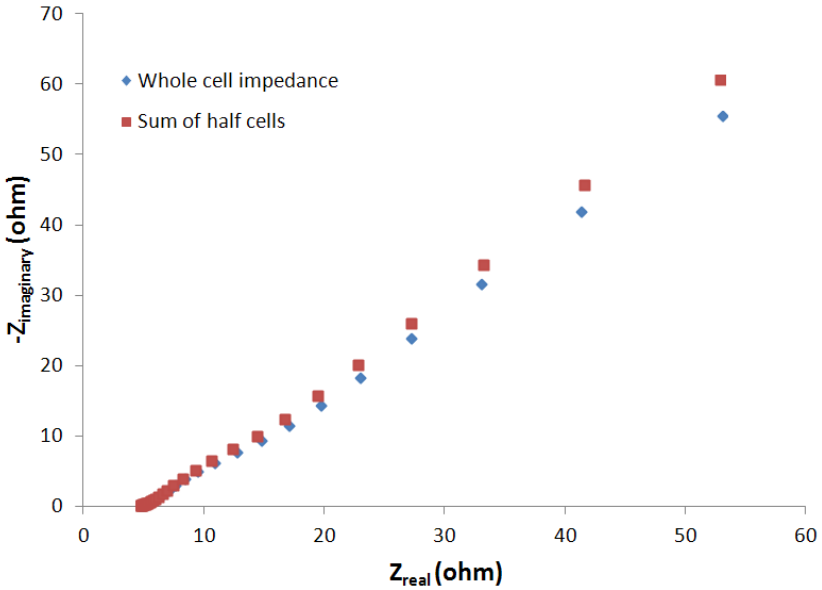

Figure 5.11 Nyquist plot of a printed battery with the three electrode configuration using a zinc pseudo-reference electrode.

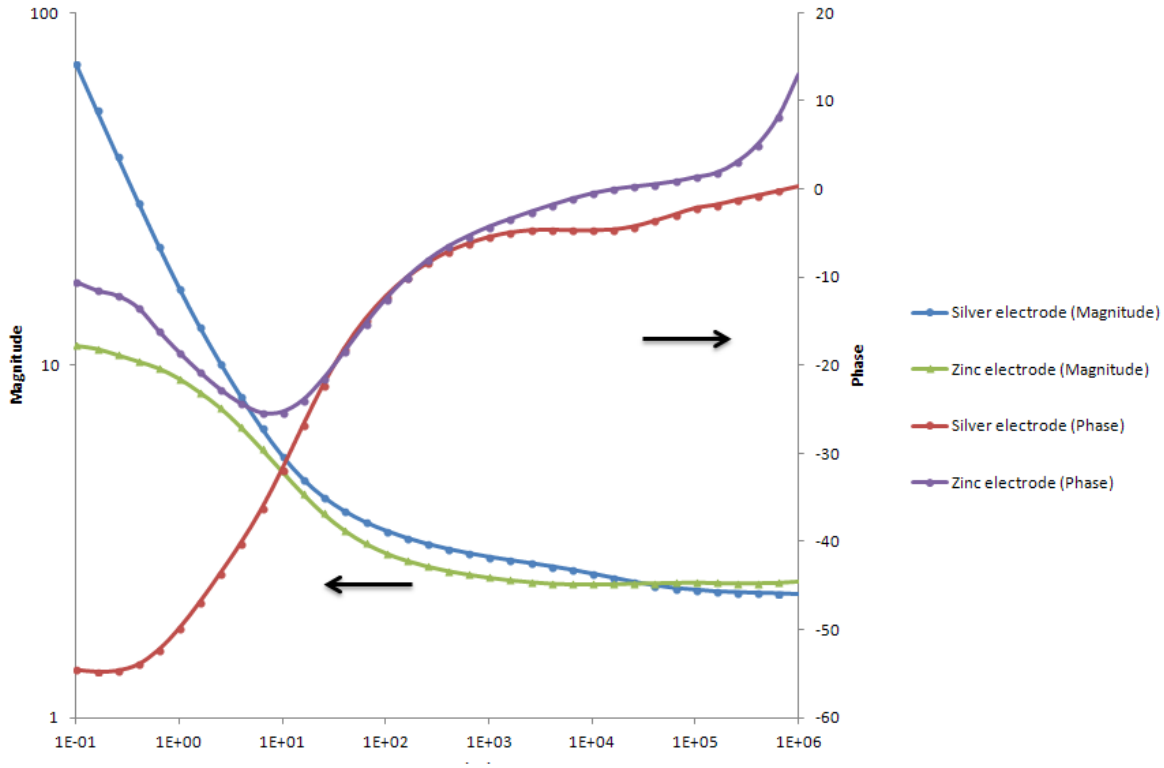

Figure 5.12 Bode plot of the zinc and silver oxide electrodes.

We extracted the relevant electrochemical phenomena from the Nyquist plot by fitting the curves with a Randles circuit element. This element consists of the electrolyte resistance in series with a parallel combination of a charge transfer resistance and a double layer capacitance (Fig. 13). This model is typically used to examine battery electrodes[133], [134]. We used this model and fitted the measured data using the Simplex method (Table 5.2).

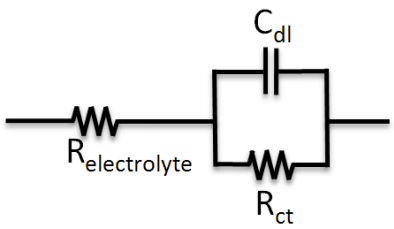

Figure 5.13 Randles circuit to model the charge transfer process and double layer formation at the electrode/electrolyte interface.

	Silver oxide electrode	Zinc electrode
$R_{electrolyte}$ (ohms)	2.71	2.53
C_{dl} (F)	0.011	0.004
R_{ct} (ohms)	67	7.13

Table 5.2. Extracted EIS parameters from the Bode plot in Figure 5.12.

From the fit to the data, we can calculate what the exchange current density of the electrodes is. The extracted charge transfer resistances correspond to exchange current densities for the silver oxide and zinc electrodes by the following formula:

$$R_{ct} = \frac{RT}{nFi_0}$$

From the charge transfer resistances, we find that the current exchange densities should be 0.77 mA cm^{-2} for the silver oxide electrode and 7.2 mA cm^{-2} for the zinc electrode. These current densities are significantly lower that the reported values in the literature. Exchange current densities for the cathodic reduction of silver oxide have been measured to be 50.9 mA cm^{-2} at 24°C (31% aq KOH) [135]. Exchange current densities of the zinc electrode have been measured to be 93 mA cm^{-2} for 1M KOH and 209 mA cm^{-2} for 7M KOH [136]. The values could be low due to an unoptimized printed electrode and/or a KOH saturated PAA separator. However, the low exchange current densities would explain the large potential drop observed in the polarization curve (Fig. 5.1).

To corroborate the EIS measurement, an independent measurement of the exchange current density should be conducted. An accurate measurement of the exchange current density requires the measurement of current density dependence on overpotential of the half-cell electrode [137]. The current density is related to the overpotential by the following equation:

$$\Delta V = A \times \ln\left(\frac{i}{i_0}\right),$$

where A is the Tafel slope, i_0 is the exchange current density (A m^{-2}), ΔV is the overpotential (V), and i is the current density (A m^{-2}). This information will allow us to construct what is known as the Tafel plot. By analyzing each electrode against a Hg/HgO reference electrode in a KOH electrolyte solution, we can extract the exchange current density. This measurement would allow us to verify the EIS results and confirm the EIS model we have used is correct. The model could also be improved upon by using a complex phase element (CPE) for the double layer capacitance. This circuit element would incorporate electrode non-idealities, such as surface roughness.

5.6 Application of the EIS data to the polarization curve

From the EIS data of the whole cell, we found that the high frequency resistance was 4.6 ohms. This was determined by calculating the resistance at the intersection of the impedance spectrum with the real axis at high frequencies (1 MHz) on the Nyquist plot (Fig. 5.11). This measured value (6.2 Ω) corresponds to the ohmic contributions in the battery, such as the current collector resistance, the electrode resistance and the bulk electrolyte resistance. This resistance value will be independent of the discharge current. We can thus plot the contribution of the ohmic resistance to the discharge potential of the polarization curve (Fig. 5.14).

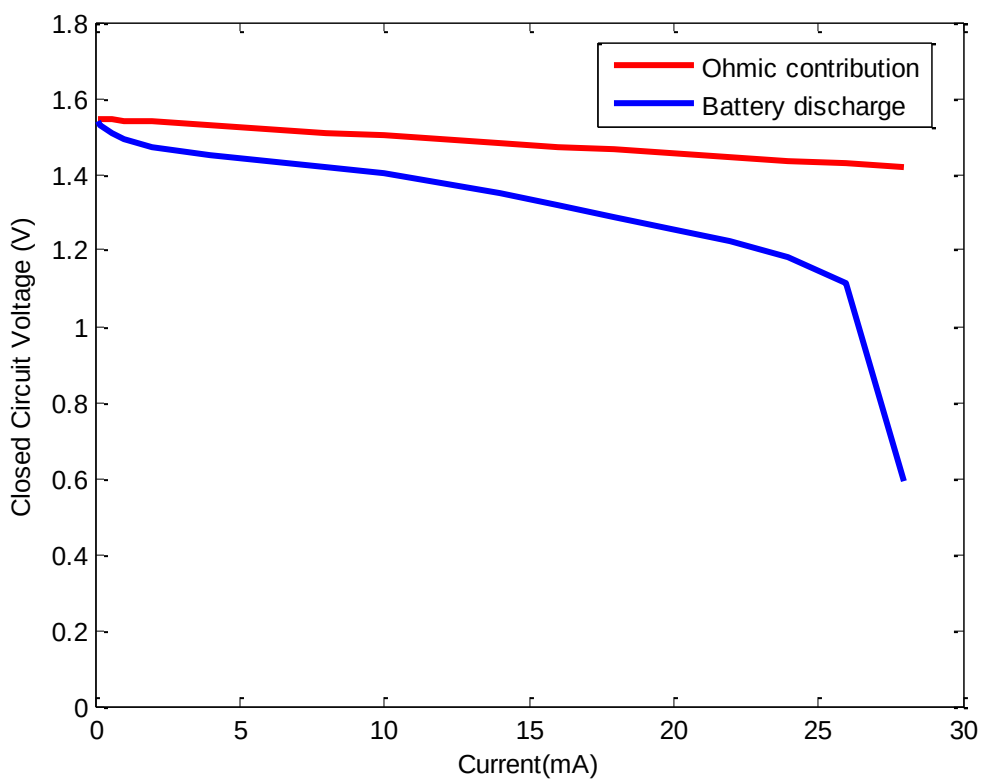

Figure 5.14 Polarization curve with voltage loss due to the ohmic contribution.

The slope of the polarization curve follows the voltage drop due to the ohmic potential drop for medium current ranges (3-15 mA). At lower currents, we are dominated by the

activation polarization, while at higher currents, the concentration overpotential dominates. To design a better battery, ideally, we would like to minimize the potential drops in the cell. From the polarization curve, we see that if we reduce the ohmic contribution, we get an overall increase in the battery potential. This could be achieved by decreasing the resistance of the current collectors, decreasing the separator thickness and decreasing the resistance of the electrode.

The largest potential drop occurs at low discharge currents. At these points, the resistance is dominated by the charge transfer resistance or the activation polarization. If we add the two extracted charge transfer resistances corresponding to each electrode, we calculate that the activation polarization should have a resistance value of 67+7=74 ohms for low discharge currents. This value is approximately what we observed (Fig. 5.15). The ohmic contribution to the resistance also needs to be included (74+4.6≈ 79 ohms) which brings the expected resistance closer to the measured value at low current densities (Fig. 5.15).

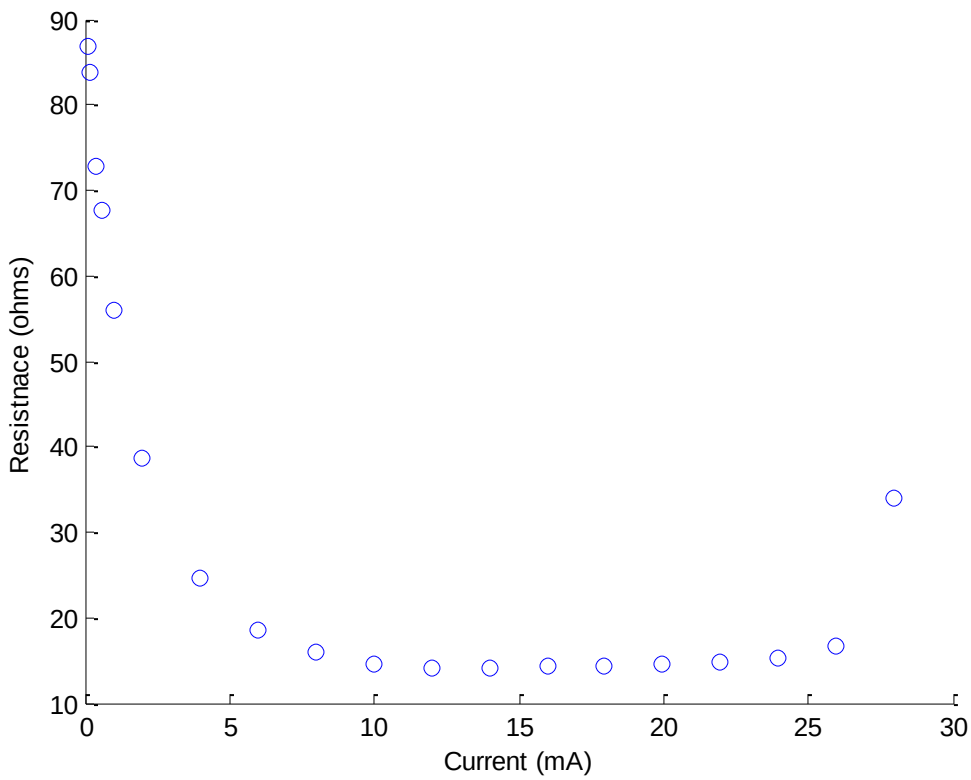

Fig. 5.15 Measured resistance at a given discharge current. Resistances were calculated from the polarization curve values and the open circuit voltages.

5.7 Conclusion

We characterized the discharge potential of the printed silver oxide battery in depth, by measuring the polarization curve and performing electrochemical impedance spectroscopy on the printed silver oxide battery. Three-electrode EIS was done using a zinc pseudo-reference electrode. From the EIS data, we were able to extract the ohmic resistance and the charge transfer resistance of a printed silver oxide battery.

Using these values, we explained the observed potential drops in the polarization curve. From the high frequency impedance, we measured a resistance value of 4.6 ohms. This consists of the ohmic components of the battery, such as the current collector resistance, the electrode resistance and the bulk electrolyte resistance. The charge transfer resistance was estimated to be 74 ohms for low current densities. This corresponds to activation polarization in the discharge potential. The concentration overpotential is still unmeasured and requires further experimentation in order to analyze the contribution of concentration gradients to the discharge potential.

From the EIS data, we see that we are largely dominated by the activation polarization. This contributes to the large potential drop for low current densities. To improve the battery performance, we would like to reduce the activation polarization. The extracted charge transfer resistances indicate that the silver oxide electrode is the dominating component in contributing to the activation polarization. To improve the battery performance, we would want to optimize the silver oxide electrode to increase the exchange current density. This will require a multi-factor experiment that examines how the electrode composition, binder choice, electrode deposition, electrolyte and electrode/electrolyte interface affect the exchange current density. This then provides useful directions for future research.

In addition to the silver oxide improvement, other improvements can be made by decreasing the ohmic resistance of the cell and increasing the exchange current density of the zinc electrode. The three-electrode technique developed here will be useful in characterizing the performance of these optimized cells. Using these techniques will lead to better silver oxide batteries with higher energy densities and larger capacities.

Chapter 6. Printed alkaline battery encapsulation

Battery packaging is required to protect the environment from exposure of the electrolyte and also to protect the electrolyte from contamination by oxygen, water, or other contaminants in the environment. In general, the battery encapsulation layer should have good chemical resistance, puncture resistance, and temperature stability. The battery chemistry will dictate the sealing requirements and properties. For example, lithium ion chemistry needs a barrier material that has resistance to hydrofluoric acid, an acid that is formed in many lithium batteries, especially when water comes into contact with fluoride containing electrolytes [138].

There is great desire to improve the packaging of batteries, including alkaline and lithium ion batteries. The replacement of a metal container with a flexible encapsulant will reduce cost, introduce enhanced functionality, and reduce the mass and volume taken by encapsulation. A low-temperature printed encapsulation layer is necessary for the production of a low cost, printed alkaline battery. Several technologies have been proposed including pouches [139], lamination, and multilayer laminates [140]. However, a fully printed encapsulation layer for alkaline batteries has not been demonstrated. We examine the use of epoxy and silicone as printed encapsulants for alkaline batteries. We do this by using the metric of resistance change of a printed alkaline PAA separator (Section 6.4.1).

6.1 Alkaline battery requirements

An alkaline, aqueous based chemistry requires a robust packaging scheme that prevents loss of the corrosive KOH electrolyte, evaporation of water from the electrolyte, and prevents exposure of carbon dioxide and oxygen to the electrolyte. An encapsulation layer needs to be robust enough to hand the high pH found in an alkaline battery (pH>14, molarities 1M-10M). These strict requirements limit the materials that can be used as an encapsulant. For example, the hydroxide ion of the electrolyte is a nucleophile that can participate in a number of reactions. The high pH can accelerate the corrosive processes of materials. Indeed, corrosion of the metal container remains an issue for commercial batteries. The corrosion of zinc produces hydrogen gas, which at high enough pressures can rupture through the metal case or insulating gasket allowing the KOH electrolyte to seep out, forming crystals of KOH (Figure 6.1). A printed encapsulation layer should be inert to the alkaline electrolyte and be able to withstand the pressure buildup due to the formation of hydrogen gas.

Another package requirement is to limit the exposure of the battery cell to oxygen. Zinc is capable of being oxidized in the presence of oxygen with the following reaction:

$$2Zn + O_2 \rightarrow 2ZnO$$

This reaction is essentially the same reaction that occurs in a zinc-air battery. In a zinc-air battery, the reduction of oxygen is performed at the porous air electrode that contains a catalyst to accelerate the reaction. The zinc electrode of a silver oxide battery, however, can also be the site of the oxygen reduction reaction. Oxygen is capable of being reduced at the zinc surface forming hydroxide ions. Studies have shown that the bubbling of air through a KOH electrolyte results in

an increase in the formation of zinc oxide at the electrode surface [141]. The oxide reduction in alkaline solutions is given by the following equations [142]:

$$O_2 + 2H_2O + 4e^- \rightarrow 4OH^- \quad E_0 = 0.401\ V_{SHE}$$

$$O_2 + 2H_2O + 2e^- \rightarrow O_2H^- + OH^- \quad E_0 = -0.076\ V_{SHE}$$

The zinc is then correspondingly oxidized forming zinc hydroxide and eventually zinc oxide. To limit the formation of zinc oxide, a printed encapsulation layer should ideally limit the diffusion of oxygen to electrolyte.

Figure 6.1. Leaked alkaline battery illustrating the formation of KOH crystals[143].

The exposure of an alkaline electrolyte to carbon dioxide in the atmosphere results in the formation of potassium carbonates. The formation of potassium carbonate results in a decrease in hydroxyl ions through the following reaction:

$$2OH^- + CO_2 \rightarrow CO_3^{2-} + 2H_2O$$

Specifically, this is a problem in zinc-air batteries where the air electrode is continually exposed to the atmosphere. This results in an increased resistance over time due to the reduction in hydroxide ion concentration. Furthermore, exposure to CO_2 limits lifespan of the battery by decreasing the porosity of the electrode and conductivity of the electrolyte due to the precipitation of K_2CO_3 [144]. The contamination is, in part, limited by the low atmospheric concentration (390 ppm) of CO_2. [145] However, over a long period time the exposure of carbon dioxide and its effect can become a limiting factor in alkaline zinc-air batteries. A poorly encapsulated silver oxide battery will also suffer from the adverse effects of CO_2. Therefore, any printed encapsulation layer should be a robust barrier to carbon dioxide and limit the diffusion of carbon dioxide molecule through the encapsulation layer.

6.2 Packaging in commercial alkaline batteries

In a typical commercial silver zinc battery, such as the silver-zinc button cell (Fig. 6.2), the metal cups form the encapsulation layer that prevents the electrolyte from leaking or evaporating from the battery. The metal caps provide an excellent barrier to gas molecules. A

downside to the packaging is that at smaller sizes these batteries have lower energy densities due to the fact that the casing takes a significant fraction of mass of the battery.

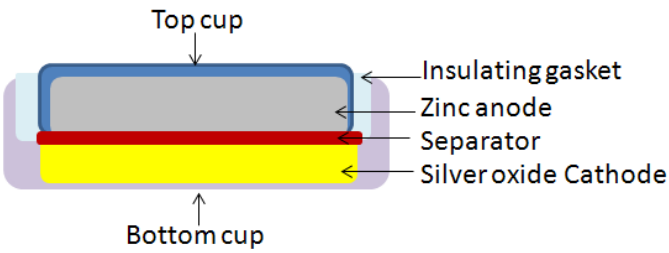

Figure 6.2 Cross section of silver-zinc button cell.

Lamination is a common technique to provide protection from the environment and has been used to encapsulate lithium-ion cells in pouches [146]. There exist two general methods of lamination: cold lamination and hot lamination. Hot lamination materials contain a plastic layer with a temperature sensitive adhesive layer attached to a plastic or metal layer. The laminate layer is pressed on the substrate and heated to a high temperatures (>100°C) that is above the melting temperature of the adhesive layer. This causes the adhesive layer to adhere to the substrate, or the others side of the adhesive layer of the laminate. This is in contrast to cold lamination which contains a pressure sensitive adhesive layer. Hot lamination is not typically acceptable for alkaline chemistry where the lamination temperature exceeds the boiling point of the alkaline electrolyte. Another concern is that laminated encapsulation layers would increase the thickness of the battery stack. For example, cold lamination layers have an adhesive layer that varies from 20-50 µm in addition to the plastic lamination layer.

Another potential low temperature encapsulation scheme is to laminate a dry photoresist layer. Such layers have been demonstrated in microfluidic applications. For example, dry film photo resists such as TMMF S2030/S2050 have been used to laminate microfludic channels that contain water [147]. In this case, the photoresist film (30 µm) was deposited, prebaked at 45˚C followed by UV cross linking and a 24 room temperature anneal.

The current schemes that exist for alkaline batteries such as metal button cells and laminated films and pouches are inconvenient for printed, small form factor batteries. What we would like to have is a low temperature, printable, flexible material that can deposited on the battery during the printing process. To achieve this goal, we have looked a several different potentially low processing temperature options that could be used for in a printed silver oxide battery.

6.3 Printed encapsulation schemes

Encapsulation with polymers is a potentially low cost and printable method of encapsulation. The polymer choice will affect the gas molecule permeability (Table 6.1). Highly polar polymers, such as polyvinyl alcohol act as excellent gas barriers, but are poor water barriers. Nonpolar polymers tend to be good water barriers, but poor gas barriers [148]. This indicates multilayer plastic may be required to act as a good water and gas (CO_2) barrier for an alkaline battery, with each layer designed to act as a barrier for a specific molecule. The encapsulation

requirements will depend on diffusion of the molecule through the free volume of the barrier layer. A problem with plastic layers are their current method of production. These polymers are heated to a high temperature and extruded or injected molded into the desired shape [149]. These high temperatures are not compatible with the processing temperatures required for an alkaline battery.

	O_2, cc-mil/m^2day	H_2O, g-mil/m^2day
HDPE	1560-3000	4-6.4
LDPE	2600-7600	12-24
Nylon 6	12-80	60-360
Polyether ester	48000-56000	8000-36000

Table 6.1 Vapor permeability through different polymer barrier layers [148].

There are other encapsulation schemes that are printable that could be used as an encapsulation layer for a printed battery. These options are listed below in Table 6.2. These material components are printable and require relatively low processing temperatures. The first option is based on long chain alkane polymers (paraffin wax). The long chain alkane polymers are solid until the melting temperature of the polymer is reached. The melting temperature is dependent on the chain length of the polymers. The disadvantage of using paraffin wax is that it requires high temperatures during deposition to melt the polymer and the encapsulant is only stable to the melting temperature of the polymer.

Printed Encapsulation Scheme	Mechanism	Barrier properties	Potential Problems
Long chain alkane (paraffin wax) $(CH_2)x$	Melting of polymer at high temperature	Good	-Stable until T_m of alkane
Negative photoresist	Photolysis of azide	Moderate	-Removal of solvent - Oxygen contamination of radical
SU-8	Crosslinking of epoxy groups of SU-8 molecules by acid catalyst	Moderate	-Removal of solvent -Reactivity with hydroxide ions of electrolyte
Epoxy	Epoxide ring opening	Moderate	-Reactivity with hydroxide ions of electrolyte
Silicone	Condensation reaction with water	Good	-Reactivity with hydroxide ions and water of electrolyte

Table 6.2 Printed encapsulation schemes for a printed encapsulation layer for a printed battery.

The next two encapsulation schemes are negative photoresist and SU-8. Negative photoresist is based on the photolysis of azide molecule that converts to nitrene intermediate that reacts with cyclized polyisoprene compounds [150]. SU-8 is also a negative photoresist that contains a SU-8 monomer, an organic solvent, and a photo-acid generator [151]. The photo acid molecule generates an acid which can catalyze cationic polymerization by opening of the epoxy rings (Fig. 6.3). A disadvantage shared by both of these encapsulation techniques is that both use solvents that have to be removed before the polymerization can occur. The removal of the

solvent typically require high temperature steps (>100C) for a brief amount of time. These process steps although potentially manageable for a battery stack are not ideal.

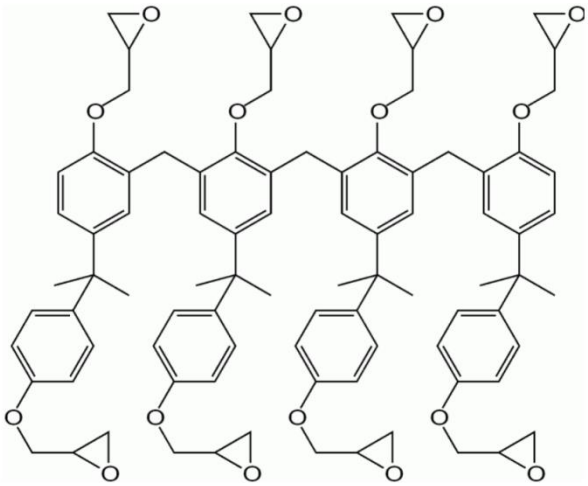

Figure 6.3 SU-8 molecule used in negative SU-8 photoresists.

The two most promising candidates in the above list are silicone caulk and epoxide. Both of these systems are commercially available, so reproducibility of the encapsulant material should not be an issue. They both provide moderate processing temperature. Epoxides and silicone caulk are cured at room temperature. The epoxy adhesive is a two part adhesive consisting of an epoxy containing molecule (resin) with a hardener or curing agent. Common hardeners are primary and secondary amines that undergo a nucleophilic addition reaction with the epoxide [152]. The combination of these two components initiates the reaction, resulting in a crosslinker structure (Fig. 6.4).

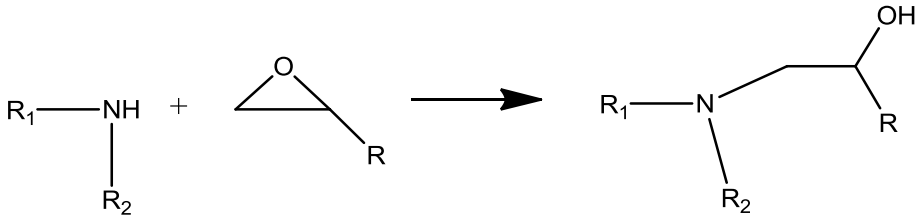

Figure 6.4 Crosslinking reaction of a secondary amine with an epoxide functional group.

Silicone caulks are room temperature vulcanizing (RTV) silicone rubbers that undergo condensation when in the presence of water [153]. The reaction is usually catalyzed by zinc or tin organometallic compounds. In the condensation reaction water reactions with functionalized silane polymers or functionalized silane crosslinkers, such as methyltriacetoxysilane, to form silanol compounds. These silanol compounds can further react, forming crosslinked structures (Fig. 6.5). The different functional groups commonly found in silicones are listed in Figure 6.5. As a product of the reaction, these volatile compounds are released. These volatile organic compounds are a small percentage of the total mass, around 1% of the total mass. The volatile compound is typically evaporated; however it can interact with the substrate/silicone interface.

For example, in silicone caulk based on acetate function groups, the acetic acid produced can corrode a metal surface.

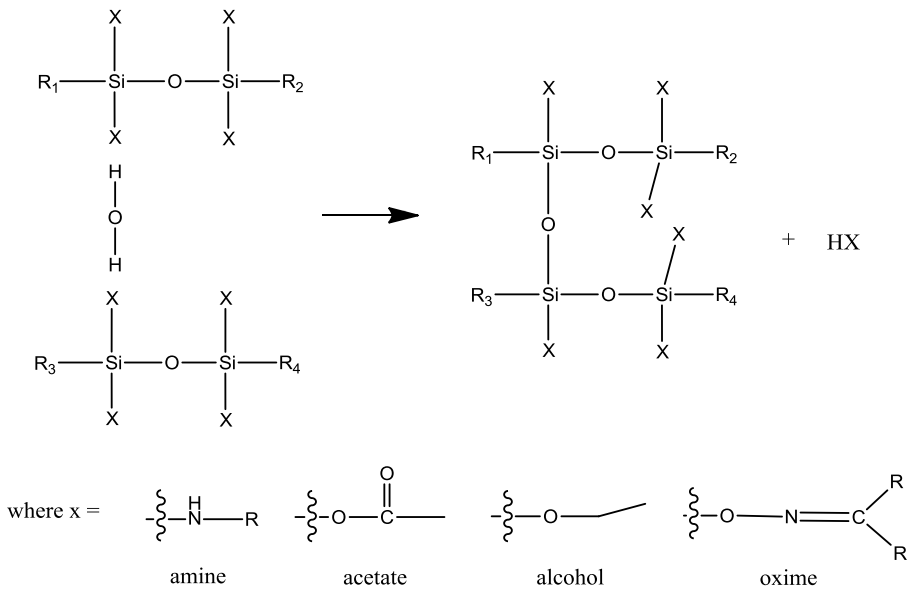

Figure 6.5 Crosslinking reaction of silicone caulk. The condensation reaction requires water from the atmosphere.

Although these systems may adversely react with KOH electrolyte of the battery stack, the interaction will ideally be only at the electrolyte/encapsulant interface. By depositing a thick enough encapsulation layer we can achieve enough polymerization to achieve significant barrier properties. These barriers may not be excellent water barriers, for example the polar epoxide based encapsulant may not be as effective as a water barrier compared to more hydrophobic polymers (such as alkane polymers), but these barrier layers can act as a substrate to deposit a second barrier layer, such as a printed metal ink or a more hydrophobic layer. The initial deposited encapsulation layer may allow for increased thermal budget so that another encapsulant layer that requires a higher processing temperature may be deposited.

6.4 Encapsulation metrics

To evaluate the barrier properties of the above encapsulation schemes we have used the metrics of conductivity change of the separator layer, and open circuit voltage measurements over time. These screening metrics will allow us to quantify the quality of encapsulation layer and what kind of performance the printed silver oxide batteries can achieve. There other metrics that can be used to quantify barrier properties such as, water vapor transmission rate (WVTR) [154], tensile strength, and rupture strength. Although measuring WVTR and mechanical strength are important metrics for quantifying barrier properties, for alkaline batteries we focus on metrics that relate to battery performance such as conductivity and OCV. Further experiments to characterize these properties will be done once a suitable encapsulant has been identified.

6.4.1 Conductivity change measurements

To measure the impedance change of the PAA electrolyte electrochemical impedance measurements were done with a parallel plate configuration where the PAA electrolyte is in between a printed Creative Materials (ink 120-07) bottom electrode and a printed PEO/silver flake top current collector (Fig. 6.6). A parallel strip of Creative Materials ink was printed a distance of 1 mm away from the larger current collector to provide a larger contact to make a connection with Gamry potentiostat clips. The standard PAA separator was prepared (Chapter 4) using a stencil with an area of 10x10 mm^2 and a height of 0.3 mm. Briefly, the PAA separator consisted of standard gel composition of 1% crosslinker, 7wt% acrylic acid, 0.5 wt% photoinitiator, 2.5% PEO filler, and 89 wt% H_2O with 1 molar equivalent KOH (Chapter 4). The gel was polymerized by UV exposure for 10 minutes. A 80/20 silver flake/PEO conductor was stencil printed on PAA separator to have a 5x5 mm^2 overlap with the bottom electrode. The structure was dehydrated for 30 minutes at 40°C, followed by saturation with 8.4 M KOH for 20 minutes.

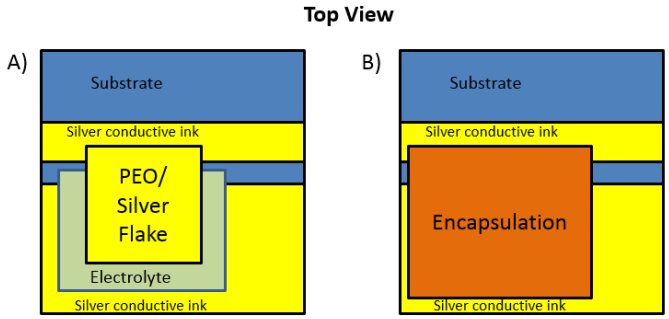

Figure 6.6 Top view of conductivity measurement A) after swelling with KOH electrolyte B) after stencil printing encapsulation layer.

Electrochemical impedance spectroscopy measurements were performed from 1 MHz to 100 Hz with a 4 mV RMS sine wave on a Gamry 3000 potentiostat. The real resistance was extracted from the Nyquist plot by extrapolating the high frequency impedance to the point where the imaginary impedance was 0. This resistance corresponds to the electrolyte resistance, the resistance of the current collectors, and the resistance of the cables and clips. We examine how the extracted resistance varies over time at different temperatures. We have chosen three temperature points of 65°C, 75°C, and 95°C to perform the temperature testing with epoxy encapsulant. The silicone based encapsulant is a better encapsulant and higher temperatures had to be used to perform the temperature measurement.

6.4.2 Open circuit measurements

The ideal way to characterize the encapsulation layer is to incorporate the encapsulation layer directly on the battery stack. This captures the interaction of the encapsulation layer and the battery stack. Open circuit measurements at room temperature and elevated temperatures allow for a characterization of the potential change with time and temperature. This will allow for the measurement of a decrease in potential due to a reduction in the hydroxy ion concentration or shortening of the cell. There is a difficulty with performing this measurement in the current printed silver oxide battery as the zinc electrode suffers from corrosion in the alkaline

environment of the printed battery. This is not a limitation of the encapsulation itself, and therefore presents an overly pessimistic estimation of encapsulation performance.

The effect of the corrosion of the zinc electrode is exhibited in Figure 6.7, which shows the open circuit voltages of an electrochemical cell consisting of printed zinc and silver oxide electrodes on printed Creative Materials silver current collectors placed into a zincate saturated solution of 8.4 M KOH. In this cell, there is no direct contact of the electrodes, so there is no possibility of shorting between the electrodes. We see the formation of bubbles at the zinc electrode/electrolyte interface throughout the open circuit measurement, indicative of the hydrogen evolution during the corrosion process. The potential also decreases dramatically after 6.5 hours. This sudden drop is due to the loss of the zinc capacity in the zinc electrode. The potential can be recovered by placing a fresh zinc electrode into the KOH electrolyte.

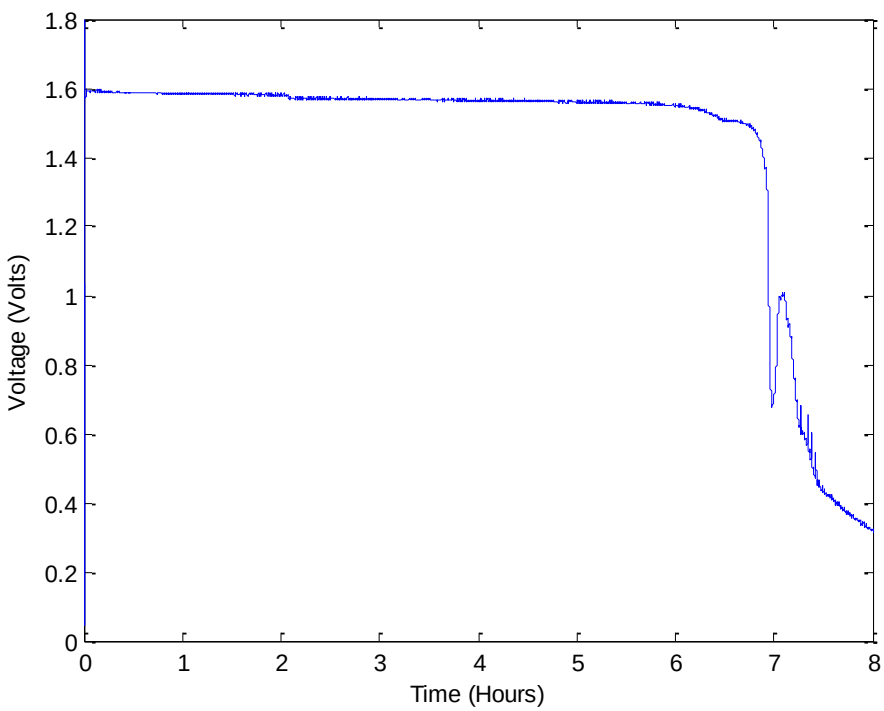

Figure 6.7 Open circuit potential of electrochemical cell consisting of a printed silver oxide and a printed zinc electrode in zincate saturated 8.4 M KOH electrolyte. The separation distance between the two planar electrodes is 1mm.

This lifetime is not acceptable for a printed battery. We ideally would like to obtain a lifetime of several months to a couple of years. The reason for low shelf is claimed to be a result of corrosion of the zinc electrode. The corrosion oxidation and reduction reactions are given by:

$$Zn + 4OH^- \rightarrow Zn(OH)_4^{2-} + 2e^-$$

$$2H_2O + 2e^- \rightarrow H_2 + 2OH^-$$

The corrosion of the zinc electrode makes quantifying the performance of the encapsulant layer difficult. To do an accurate test of the shelf life of the battery and how the encapsulating layer protects the battery requires the development of a new zinc electrode and current collector that minimizes corrosion of the zinc electrode. We do take some measures to slow the corrosion rate; for example, we have dissolved zinc oxide into our KOH solutions to saturate our solutions with zincate thus slowing the dissolution rate of the zinc electrode. This method is not sufficient to completely eliminate the corrosion of the zinc electrode. Other methods to achieve this will be discussed in the section 6.7. Once the zinc electrode has been improved, encapsulated open circuit measurements can be performed to characterize the printed encapsulation schemes.

6.5 Epoxy encapsulation

The epoxy encapsulation was done with LOCTITE® Epoxy Instant Mix 5 Minute. This commercial epoxy is a two part adhesive containing an epoxy resin and a hardener. The epoxy is mixed in equal parts to form a hardened bond. The setting time is 5 minutes with full strength reached in 24 hours. The epoxy is said to be water resistant and shrink proof. The epoxy uses a polymercaptan and amine hardener. The VOC content is 0.1% by weight.

The Loctite Instant Mix Epoxy was mixed for a minute to insure mixing of the epoxy and harder components. The epoxy was then stencil printed on the conductivity test structure with a stencil height of 650 µm. A cure time of 15 minutes was used to insure the epoxy layer had polymerized. Afterwards, the EIS measurement was performed.

6.5.1 Conductivity change measurements

Figure 6.8 shows the resistance change at different temperatures over a time range of 5 to 30 minutes. The resistance is normalized to the resistance before depositing the epoxy on the test structure and letting it cure for 10 minutes. We see an increase in resistance over time. Furthermore, the slope increases with temperature. The explanation for the increased resistance is the loss of water in the electrolyte leading to a lower ionic conductivity.

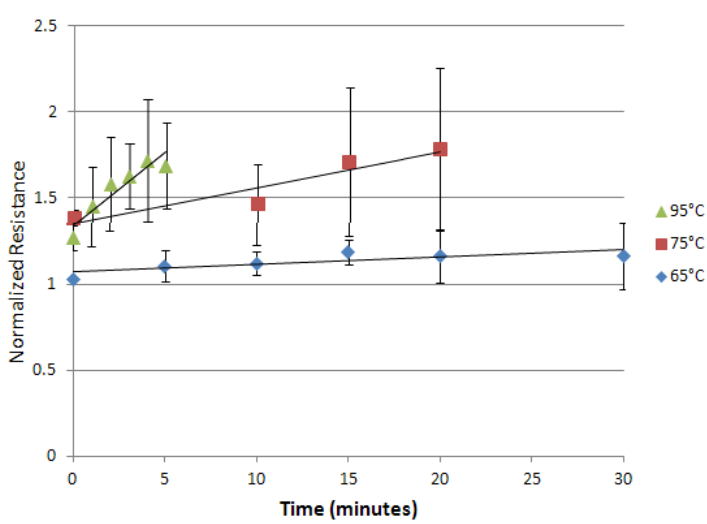

	Slope	Intercept
95 °C	0.0842	1.346
75°C	0.0211	1.3494
65°C	0.00042	1.0716

Figure 6.8 Resistance change of separator encapsulated with epoxy as a function of time at different temperatures.

Using the slopes from the measured resistances we can extract an activation energy corresponding to the resistance change with time (Fig. 6.9). We model this change as the rate, *k*, resistance/ time. We assume the resistance change follows an Arrhenius relationship of the form:

$$k = A\, e^{-E_a/RT}$$

where E_a is the activation energy, *A* is the prefactor, and *R* is the universal gas constant. We assume that *A* and E_a have no dependence on temperature. Using this equation, we calculate the activation energy and prefactor for the resistance change (Figure 6.8). From this plot we calculate that the resistance change has an activation energy of 99.8 J/mol and a prefactor value of 1.34×10^{13} Ω/minute. The Arrhenius relationship fits the resistance change well, suggesting there is some temperature dependence of reaction rate occurring in the encapsulated battery structure. That resistance change could be due a loss of water or possibly a reaction occurring between the electrolyte and the encapsulation layer.

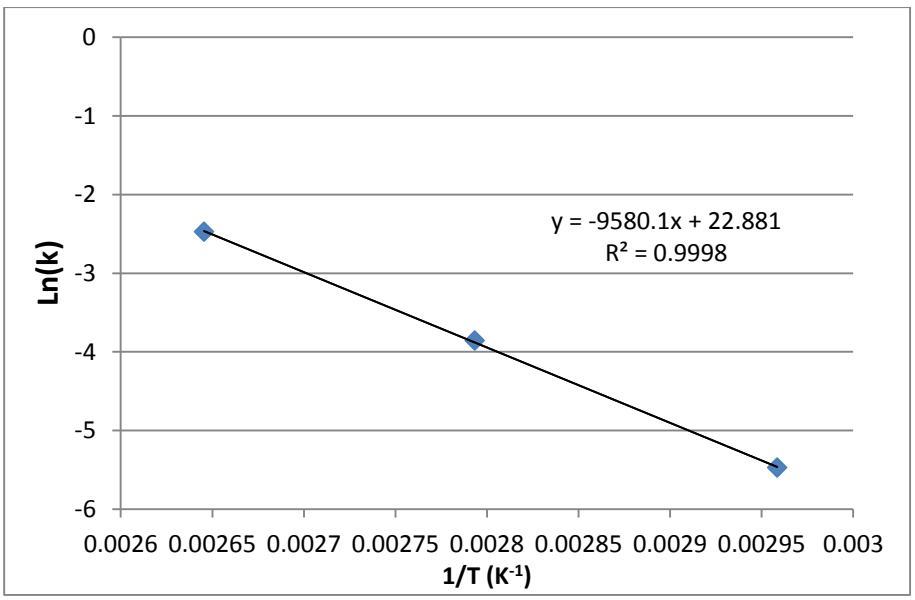

Figure 6.9 Extraction of activation energy from resistance change at different temperatures for the epoxy encapsulant.

Assuming the Arrhenius relationship holds at room temperature, we can calculate how long it will take the resistance to double, say from 0.8 Ω to 1.6 Ω. Using the extracted E_a and *A* values and a temperature of 25°C, we calculate that it will take 3.7 hours for the resistance to double. This calculated value is not sufficient for a printed battery. This indicates that current epoxy encapsulation scheme is a poor alkaline encapsulant.

6.6 Silicone encapsulation

We have looked at the use of GE Silicone II Paintable silicone caulk as encapsulation layer. This silicone is non-acrylic based and doesn't break down in water. This formulation sets in 3 hours rather than the 24 hours required by most acrylic silicone caulk. We have deposited this

caulk using stencil printing on the substrate of interest. We deposit thick layers to ensure complete coverage over the electrolyte layer.

Deposition of the silicone layer results in an encapsulated cell where the silicone caulk undergoes solidification. There is likely a side chemical reaction that is occurring at the silicon/separator interface as evident by the color change at that interface (Fig. 6.10B). The reaction is the result of the KOH electrolyte, as the PAA gel saturated in water doesn't produce the same result (Fig. 6.10A). The exact chemical reaction is not known as the silicone caulk ingredients are proprietary, but the reaction likely results in a decrease in the hydroxide ion concentration as the hydroxyl ion can act as a nucleophile causing hydrolysis of some ingredient of the silicone caulk.

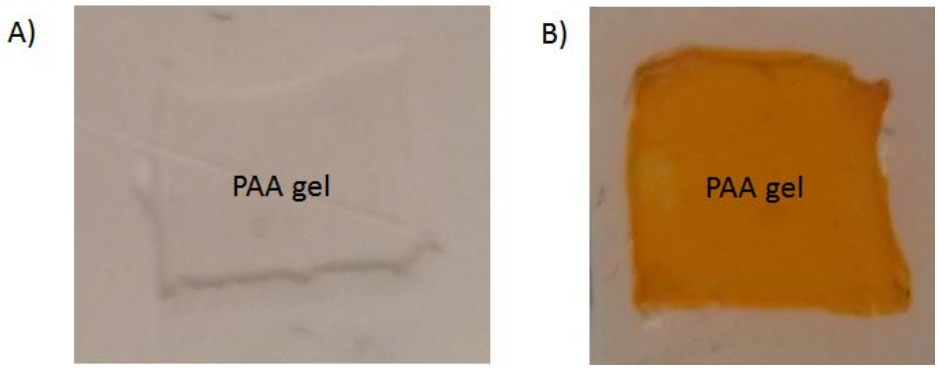

Figure 6.10 Encapsulation of PAA electrolyte with silicone caulk. A) a water saturated PAA gel and B) a 8.4 M KOH saturated PAA gel. The color change in B) is associated with a chemical reaction between the hydroxide ions in the electrolyte and a chemical in the silicone caulk.

6.6.1 Conductivity change measurements

The silicone caulk conductivity measurements were performed in a similar fashion to the epoxy encapsulated PAA gel separators (Section 6.5.1) (Fig. 6.6). The silicone caulk was stencil printed over the PAA separator test structure with a stencil height of 650 µm. Temperature testing was done at 95°C, 105°C, and 120°C. EIS measurements were performed every 5 minutes after the test structure had cooled back to room temperature.

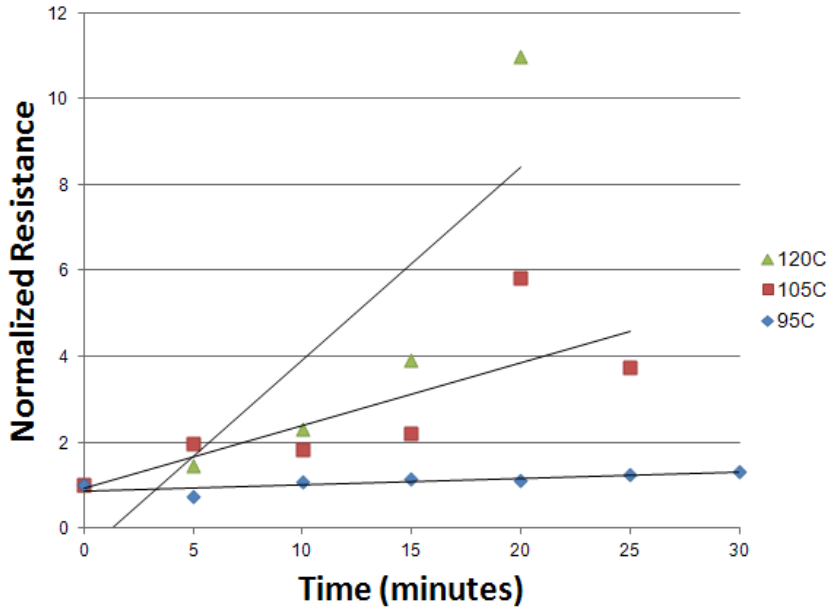

	Slope	Intercept
95 °C	0.013	0.93
105 °C	0.14	0.010
120 °C	0.45	-0.15

Figure 6.11 Resistance change of a separator encapsulated with silicone caulk as a function of time at different temperatures.

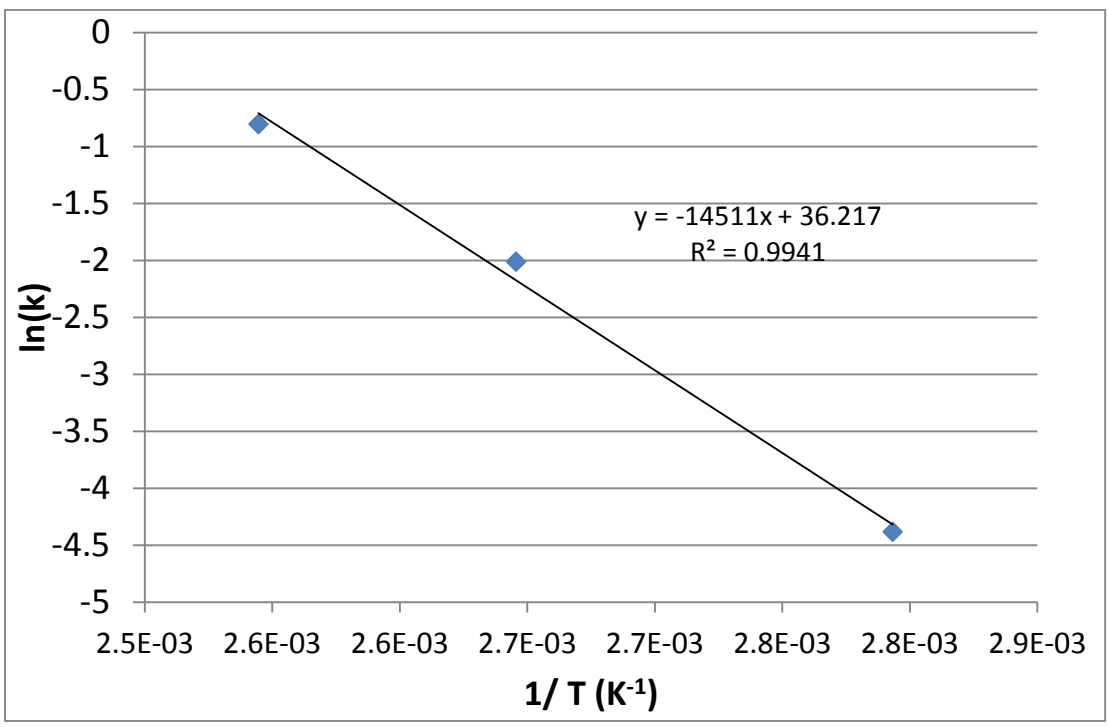

Figure 6.12 Extraction of activation energy from resistance change at different temperatures for the silicone encapsulation.

In figures 6.9 and 6.11, we see that higher temperatures are required for the silicon caulk encapsulation layer to observe a resistance change, suggesting that the silicone caulk is a better encapsulant compared to the epoxy. We can use the extracted activation energies and prefactors

to calculate the resistance change at room temperature for the printed PAA/electrode test structure. Using the extracted values (Table 6.3), we calculate the time it takes for the epoxy and silicone caulk cell's resistance to double (i.e. from a resistance of 0.8 Ω to 1.6 Ω). We see that silicone caulk is a much better encapsulant compared to epoxy with expected doubling times of 101.3 and 3.7 hours, respectively. This resistance change should be comparable to the resistance change we would observe for an encapsulated battery. This resistance change allows us to estimate the lifetime on the encapsulated cell.

Encapsulant	Activation Energy ($J\ mol^{-1}$)	Prefactor ($Ohm\ s^{-1}$)	*k* ($ohm\ s^{-1}$)	Time for resistance to double at room temperature (hours)
Epoxy	$7.9x10^5$	$8.7x10^9$	$7.6x10^{-5}$	3.7
Silicone Caulk	$1.2x10^5$	$5.4x10^{15}$	$2.7x10^{-6}$	101.3

Table 6.3 Extracted activation energy and prefactors for the epoxy and silicone caulk encapsulated test structures calculated from Figures 6.10 and 6.12.

The measured resistance change indicates that silicone caulk and epoxy will not be sufficient encapsulants for a printed alkaline battery. Doubling of the resistance in 4-101 hours will not be acceptable for most commercial applications. We would like to have minimal resistance change in a printed battery. To improve the encapsulation layer we could deposit a multilayer stack where we use the printed silicone caulk or epoxy layer as a substrate layer for further encapsulation layers, such as a metal layer or a perfluorooctyltrichlorosilane (FOTS) layer. The silicone caulk or epoxy encapsulant would allow for the deposition of a material that required a higher processing temperature or a dry surface. By moving to a multilayer structure we are able to limit the loss of water, or exposure to oxygen or carbon dioxide, by increasing the mean free path and changing the barrier properties of each layer.

The Arrhenius relationship is a good fit for the resistance change, with high R^2 values (Fig. 6.9 and Fig. 6.12). The exact mechanism for the resistance change is not known and requires further study. The Arrhenius behavior could be due to the diffusion of water molecules from the PAA electrolyte through the encapsulant layer to the atmosphere. It could also be due to the diffusion of CO_2 to the PAA electrolyte, thus leading to increase of the electrolyte resistance. Characterization of the encapsulant by performing MVTR and mass loss measurements will help identify the mechanism for the resistance change observed in the PAA electrolyte test structure. We could also calculated diffusion rates and activation energies for gas molecules through the encapsulation layer and see how they correlate with the measured resistance change activation energies.

We can also apply the same electrochemical impedance spectroscopy technique to the encapsulated, printed battery to monitor how the impedance changes over time with encapsulation. If we have appropriate EIS models, we could also begin to characterize the effect of the encapsulation on the electrodes and see whether the encapsulation layer affects the charge transfer resistance or other aspects of the battery cell. The models developed in Chapter 5 provide a good starting point to begin characterizing the encapsulated, printed silver oxide battery.

6.7 Corrosion of the zinc electrode

One problem with alkaline zinc based chemistries is the high rate of corrosion of the zinc electrode in alkaline environments (pH> 14). For a printed battery formed in the charged state, the current collector will be in electrical contact with the electrode and exposed to the electrolyte, so galvanic corrosion needs to be considered. In a zinc-manganese battery printed silver current collectors were used [84]. Gold current collectors and graphite based collectors were considered, but not used due to the low conductivity of graphite and the assumption that gold may promote galvanic corrosion of the zinc electrode. Silver current collectors have used been used in a zinc electrodes, but they also may promote galvanic corrosion of the zinc electrode

A disadvantage of using a noble metal is the potential for an increase in corrosion of the zinc electrode through galvanic corrosion [155]. Galvanic corrosion is the increase in corrosion of one metal, when two dissimilar metals are brought into contact with each other and an electrolyte solution. This process is separate for the normal corrosion process of an electrode in the presence of an electrolyte solution. In galvanic corrosion, the potential difference between the two metals drives an electric current to supply the corrosion process. The metal with the higher potential becomes the cathode while the metal with the lower potential becomes the anode, i.e. the metal that undergoes corrosion. The cathode is protected from corrosion by the fact that the anode is preferentially corroded. The corrosion depends on the geometry of the metals, the surface conditions of the metals, as well as the electrolyte content and pH. However, we can predict whether corrosion will occur from the anodic index of the metals at interest. Table 6.4 shows a list of common metals and their respective anodic index. From the plot, we see there is acceleration of zinc corrosion when zinc is in contact with a metal that has a more positive value for the anodic index.

Metal	**Index (V)**
Gold	-0.00
Silver	-0.15
Nickel	-0.30
Copper	-0.35
Lead	-0.70
Zinc	-1.25
Magnesium	-1.75

Table 6.4 Anodic index of several common metals

In the current battery setup, we have a noble metal, silver, in contact with the zinc electrode. In this configuration galvanic corrosion can occur. Indeed, zinc in contact with silver has been observed to have a an accelerated corrosion rate in alkaline environments with vigorous hydrogen evolution [141]. The silver likely promotes hydrogen evolution allowing for the dissolution of zinc to zincate. Support for this process is evident in the printed silver oxide batteries, where we see the production of hydrogen gas which produces bubbles in the encapsulant layer as it is curing.

The corrosion reaction can be minimized by using a current collector that has a higher overpotential for the hydrogen evolution reaction. On such metal is nickel. An electronically

conductive adhesive layer or flake ink based on nickel or tin could replace the current silver current collector [75]. Another option is to remove exposure to the current collector by electroplating zinc onto the current collector [78]. This would remove contact of the electrolyte to the current collector and stop the galvanic corrosion process.

Other methods to reduce the corrosion of the zinc electrode could be done. One technique to reduce corrosion of zinc electrode is to form a zinc amalgam with mercury [77]. Use of mercury in alkaline batteries is no longer attractive, so researchers have developed other environmentally friendly methods of reducing the corrosion rate. For example, the zinc could be alloyed with other metals to increase the hydrogen overpotential [156]. Organic surfactants can also be added to the zinc electrode to reduce the hydrogen evolution rate [157], [158]. Using these techniques with a more appropriate current collector will allow for the creation of a more stable battery.

6.8 Conclusion

On the basis of conductivity change measurements performed, the epoxy and silicone encapsulation schemes developed in this chapter show promise for their use as a printed encapsulation layer for an alkaline battery. The silicone caulk encapsulation layer shows more promise due to lack of resistance change during the conductivity test. Further experiments at higher temperatures and for longer times need to done get an accurate measurement. Corrosion of the zinc electrode has to be dealt with to develop a stable battery, but once this is done, long term studies can be performed to analyze the encapsulation layers to develop a suitable barrier layer for an alkaline battery. Once this is achieved, we will have demonstrated a fully printed silver oxide battery.

Chapter 7. Conclusions and Future Work

7.1 Conclusions

We have demonstrated a flexible, high energy density, printed battery that has the potential to be useful in many flexible, printed devices and applications. In this work, a printed silver oxide battery was developed using extrusion printing and stencil printing to deposit the battery components. We have taken the zinc-silver oxide chemistry and developed the battery components so that they are capable of being printed. Two battery architectures were demonstrated: a planar architecture, with electrodes side-by-side and a vertical architecture, with the electrodes facing each other. The discharge performance of the printed batteries was characterized and used to optimize the performance of the battery.

The planar architecture, although simpler to fabricate due to less stringent layer requirements, suffers from high internal resistances and lower energy densities. In Chapter 3, we have identified the material components for printing the zinc electrode, silver oxide electrode and separator layer for a planar battery. We have optimized the electrode components for high utilization and low resistance. A PEO/KOH electrolyte was used for the separator layer due to its resistance to oxidation by the silver oxide. The optimized planar architecture demonstrated a high resistance of 150-200 ohms at C/2 discharge rates of 1.8 mA/cm^2. Despite the high internal resistances, the battery was capable of volumetric energy densities of 4.1 mWh cm^{-2} and high capacities of 3.5 mAh cm^{-2}. These values are comparable to other printed based batteries in the literature, demonstrating the usefulness of this chemistry as a printed energy source.

The planar architecture was improved upon by developing a vertical printed battery. In Chapter 4, we presented the development of a polyacrylic acid separator for use in a vertical printed battery. This photopolymerized gel contains a polyethylene oxide filler to increase the mechanical stability. After saturation of this layer with a KOH electrolyte, this layer has conductivities on the same order of pure KOH solutions. The vertical printed battery shows better performance than the planar architecture; the internal resistance of the vertical printed battery is lower than that of the printed planar battery (20-30 ohms at a C/2 discharge rate). This printed battery exhibits a higher capacity of 5.4 mAhr/cm^2 and volumetric energy densities of 10 mWhr cm^{-3}. This capacity and energy density are higher than those of the printed planar battery, illustrating the advantages of the vertical architecture; indeed, the achieved capacities are similar to or exceed those of published printed batteries.

In Chapter 5, the vertical battery was characterized in depth using electrochemical impedance spectroscopy (EIS). A three-electrode impedance setup was used with a zinc pseudo-reference electrode to characterize the zinc and silver oxide electrodes individually. A Randel's

circuit model was used to fit the data. The extracted parameters are then used to explain the discharge potential dependence on discharge current in the polarization curve. Various regions of the plot are explained, including the activation polarization and the ohmic polarization. Based on these extracted parameters, suggestions are made for an optimized battery structure.

An important layer that needs to be developed is a flexible, printed encapsulation scheme for a printed battery. We have examined the use of two printable means of encapsulating an alkaline battery: epoxy and silicone caulk. These two polymers are capable of being printed and require room temperatures for processing. The encapsulation layers are characterized with conductivity measurements of a polyacrylic gel and open circuit voltage measurements of a printed silver oxide battery. The silicone encapsulant shows promising results with very little change in the resistance of the encapsulated polyacrylic acid separator. The open circuit battery measurements are convoluted by the presence of corrosion in the zinc electrode. An improved zinc electrode is required to identify a proper encapsulant for an alkaline battery. However, based on the conductivity measurements, the silicone caulk encapsulating layer shows promise for an encapsulated printed battery.

Throughout this work, we have demonstrated a printed, high energy vertical battery with the development of a high ionic conductivity, photopolymerizable alkaline separator based on polyacrylic acid. This separator demonstrates good mechanical stability and ionic conductivities on the order of 0.4 S/cm. Using the synthesized PAA separator, we have demonstrated a stencil printed silver oxide battery with areal capacities of 5.4 mAhr cm^{-2} and volumetric capacities of 7.1 mAhr cm^{-3}. The batteries show no difference in discharge upon flexing at a bend radius of 1.0 cm, indicating their potential in flexible applications. The processes developed are scalable to large scale manufacturing and allow for customization to the application. The demonstrated flexible, high energy density, stencil printed battery has the potential to be useful in many flexible, printed devices and applications.

7.2 Future Work

The printed silver oxide battery shows promise as an energy source for printed electronics. The battery has energy densities and capacities comparable to other printed based batteries in the literature. Further optimization of the battery stack is required to improve the performance of the battery. The zinc electrode needs to be optimized to reduce the corrosion of the zinc electrode. The energy density can be further improved by changing the species of the silver oxide electrode from monovalent silver oxide to divalent silver oxide (Ag_2O to AgO). This will result in a higher open circuit voltage and an increased capacity. The energy density can also be improved by reducing the thickness of the separator layer. This will necessitate the ability to deposit uniform electrode layers and to deposit and polymerize the gel separator precursor solution into thin layers.

In addition to the above optimization of the battery to maximize the energy density and capacity, lifetime studies need to be conducted to characterize the shelf life of the printed battery. This is vital in order to identify the commercial viability of this technology. Specifically, the migration of soluble silver oxide species to the zinc electrode is a problem for zinc-silver oxide batteries because it results in a loss of capacity and has the potential to lead to shorting of the battery. The separator and electrode structures need to be optimized to mitigate this effect and to reduce the transport of the soluble silver oxide species. Minimizing the corrosion of the zinc electrode also needs to be done, as this can lead to pressure build up in the cell which can possibly alter the cell structure and lead to cell rupture.

A lot of work is still required to develop a printed encapsulation scheme for an alkaline battery. A key component will be developing a material that is printable, yet has good barriers and is base stable. Detailed characterization of the barrier layer is required, such as characterizing the rupture strength, the WVTR and the long-term stability of the layer in the presence of an alkaline environment. The interaction of the encapsulating layer and saturated battery stack needs to be understood and any unwanted interactions between them need to be minimized. Methods will need to be developed to characterize the influence of the material choice and material structure, as they will likely have a profound impact on the barrier properties of the encapsulating layer. If a single encapsulation layer is not sufficient as an encapsulating layer, the development of multilayer encapsulation may be needed.

The described work above will require detailed analysis of the battery performance. Improved modeling and battery characterizing (such as EIS) will be required to accurately predict the physical phenomena. There is much work to be done to further improve the performance and understanding of the printed silver oxide battery. However, once the improvements have been made and the challenges have been overcome, the printed silver oxide battery will likely be ready for integration into a printed circuit application, thus creating a lightweight, flexible, and fully powered electronic system.

References

[1] T. E. Rardin and R. Xu, “Printing Processes Used to Manufacture Photovoltaic Solar Cells.,” *J. Technol. Stud.*, vol. 37, no. 2, 2011.

[2] D. J. Hayes, W. R. Cox, and M. E. Grove, “Low-cost display assembly and interconnect using ink-jet printing technology,” *J. Soc. Inf. Disp.*, vol. 9, no. 1, pp. 9–13, Mar. 2001.

[3] N. Gergel-Hackett, B. Hamadani, B. Dunlap, J. Suehle, C. Richter, C. Hacker, and D. Gundlach, “A Flexible Solution-Processed Memristor,” *IEEE Electron Device Lett.*, vol. 30, no. 7, pp. 706–708, Jul. 2009.

[4] A. Knobloch, A. Manuelli, A. Bernds, and W. Clemens, “Fully printed integrated circuits from solution processable polymers,” *J. Appl. Phys.*, vol. 96, no. 4, pp. 2286–2291, 2004.

[5] M. A. M. Leenen, V. Arning, H. Thiem, J. Steiger, and R. Anselmann, “Printable electronics: flexibility for the future,” *Phys. Status Solidi A*, vol. 206, no. 4, pp. 588–597, Apr. 2009.

[6] I. Gibson, D. W. Rosen, and B. Stucker, *Additive manufacturing technologies*. Springer, 2010.

[7] M. Berggren, D. Nilsson, and N. D. Robinson, “Organic materials for printed electronics,” *Nat. Mater.*, vol. 6, no. 1, pp. 3–5, Jan. 2007.

[8] L. Xie, “Heterogeneous Integration of Silicon and Printed Electronics for Intelligente Sensing Devices,” dissertation, KTH, 2014.

[9] G. H. Gelinck, H. E. A. Huitema, E. van Veenendaal, E. Cantatore, L. Schrijnemakers, J. B. P. H. van der Putten, T. C. T. Geuns, M. Beenhakkers, J. B. Giesbers, B.-H. Huisman, E. J. Meijer, E. M. Benito, F. J. Touwslager, A. W. Marsman, B. J. E. van Rens, and D. M. de Leeuw, “Flexible active-matrix displays and shift registers based on solution-processed organic transistors,” *Nat. Mater.*, vol. 3, no. 2, pp. 106–110, Feb. 2004.

[10] F. Liao, C. Chen, and V. Subramanian, “Organic TFTs as gas sensors for electronic nose applications,” *Sens. Actuators B Chem.*, vol. 107, no. 2, pp. 849–855, Jun. 2005.

[11] Y. J. Chan, C. P. Kung, and Z. Pei, “Printed RFID: technology and application,” in *Radio-Frequency Integration Technology: Integrated Circuits for Wideband Communication and Wireless Sensor Networks, 2005. Proceedings. 2005 IEEE International Workshop on*, 2005, pp. 139 – 141.

[12] J. B. Lee and V. Subramanian, “Weave patterned organic transistors on fiber for E-textiles,” *IEEE Trans. Electron Devices*, vol. 52, no. 2, pp. 269–275, 2005.

[13] J. A. Rogers and Y. Huang, “A curvy, stretchy future for electronics,” *Proc. Natl. Acad. Sci.*, vol. 106, no. 27, pp. 10875–10876, Jul. 2009.

[14] R. Kitsomboonloha, S. J. S. Morris, X. Rong, and V. Subramanian, “Femtoliter-Scale Patterning by High-Speed, Highly Scaled Inverse Gravure Printing,” *Langmuir*, vol. 28, no. 48, pp. 16711–16723, Dec. 2012.

[15] D. J. Gundlach, “Organic electronics: Low power, high impact,” *Nat. Mater.*, vol. 6, no. 3, pp. 173–174, Mar. 2007.

[16] S. Priya and D. J. Inman, *Energy harvesting technologies*, vol. 21. Springer, 2009.

[17] V. Chawla and Dong Sam Ha, “An overview of passive RFID,” *IEEE Commun. Mag.*, vol. 45, no. 9, pp. 11–17, Sep. 2007.

[18] R. Venkatasubramanian, E. Siivola, T. Colpitts, and B. O’Quinn, “Thin-film thermoelectric devices with high room-temperature figures of merit,” *Nature*, vol. 413, no. 6856, pp. 597–602, Oct. 2001.

[19] H. Matsumoto, K. Kuribayashi, H. Uda, Y. Komatsu, A. Nakano, and S. Ikegami, “Screen-printed CdS/CdTe solar cell of 12.8% efficiency for an active area of 0.78 cm2,” *Sol. Cells*, vol. 11, no. 4, pp. 367–373, May 1984.

[20] A. Erturk and D. J. Inman, *Piezoelectric Energy Harvesting*. John Wiley & Sons, 2011.

[21] S. Roundy, D. Steingart, L. Frechette, P. Wright, and J. Rabaey, “Power Sources for Wireless Sensor Networks,” in *Wireless Sensor Networks*, H. Karl, A. Wolisz, and A. Willig, Eds. Springer Berlin Heidelberg, 2004, pp. 1–17.
[22] A. Burke, “Ultracapacitors: why, how, and where is the technology,” *J. Power Sources*, vol. 91, no. 1, pp. 37–50, Nov. 2000.
[23] D. Pech, M. Brunet, P.-L. Taberna, P. Simon, N. Fabre, F. Mesnilgrente, V. Conédéra, and H. Durou, “Elaboration of a microstructured inkjet-printed carbon electrochemical capacitor,” *J. Power Sources*, vol. 195, no. 4, pp. 1266–1269, Feb. 2010.
[24] L. C. Hoffman and T. Nakayama, “Screen printed capacitor dielectrics,” *Microelectron. Reliab.*, vol. 7, no. 2, pp. 131–135, May 1968.
[25] “Thin and Flexible Lithium Polymer Batteries – SOLICORE – The Future of Power, Today.” [Online]. Available: http://www.solicore.com/flexion-batteries.asp. [Accessed: 14-Apr-2014].
[26] C. C. Ho, “Dispenser Printed Zinc Microbattery with an Ionic Liquid Gel Electrolyte,” Ph.D., University of California, Berkeley, United States -- California, 2010.
[27] G. A. Ghiurcan, C.-C. Liu, A. Webber, and F. H. Feddrix, “Development and Characterization of a Thick-Film Printed Zinc-Alkaline Battery,” *J. Electrochem. Soc.*, vol. 150, no. 7, pp. A922–A927, Jul. 2003.
[28] A. M. Gaikwad, G. L. Whiting, D. A. Steingart, and A. C. Arias, “Highly Flexible, Printed Alkaline Batteries Based on Mesh-Embedded Electrodes,” *Adv. Mater.*, vol. 23, no. 29, pp. 3251–3255, Aug. 2011.
[29] J. Newman and K. E. Thomas-Alyea, *Electrochemical Systems*. John Wiley & Sons, 2004.
[30] M. E. Orazem and B. Tribollet, *Electrochemical Impedance Spectroscopy*. John Wiley & Sons, 2011.
[31] P. Calvert, “Inkjet Printing for Materials and Devices,” *Chem. Mater.*, vol. 13, no. 10, pp. 3299–3305, Oct. 2001.
[32] S. B. Fuller, E. J. Wilhelm, and J. M. Jacobson, “Ink-jet printed nanoparticle microelectromechanical systems,” *Microelectromechanical Syst. J. Of*, vol. 11, no. 1, pp. 54–60, 2002.
[33] H. Sirringhaus, T. Kawase, R. H. Friend, T. Shimoda, M. Inbasekaran, W. Wu, and E. P. Woo, “High-Resolution Inkjet Printing of All-Polymer Transistor Circuits,” *Science*, vol. 290, no. 5499, pp. 2123–2126, Dec. 2000.
[34] M. Singh, H. M. Haverinen, P. Dhagat, and G. E. Jabbour, “Inkjet Printing—Process and Its Applications,” *Adv. Mater.*, vol. 22, no. 6, pp. 673–685, Feb. 2010.
[35] F. C. Krebs, “Fabrication and processing of polymer solar cells: A review of printing and coating techniques,” *Sol. Energy Mater. Sol. Cells*, vol. 93, no. 4, pp. 394–412, Apr. 2009.
[36] N. C. van der Vaart, H. Lifka, F. P. M. Budzelaar, J. E. J. M. Rubingh, J. J. L. Hoppenbrouwers, J. F. Dijksman, R. G. F. A. Verbeek, R. Van Woudenberg, F. J. Vossen, M. G. H. Hiddink, J. J. W. M. Rosink, T. N. M. Bernards, A. Giraldo, N. D. Young, D. A. Fish, M. J. Childs, W. A. Steer, D. Lee, and D. S. George, “Towards large-area full-color active-matrix printed polymer OLED television,” *J. Soc. Inf. Disp.*, vol. 13, no. 1, pp. 9–16, Jan. 2005.
[37] A. De la Fuente Vornbrock, “Roll printed electronics: Development and scaling of gravure printing techniques,” 2009.
[38] D. A. Clark, “Major Trends in Gravure Printed Electronics,” 2010.
[39] B. Michel, A. Bernard, A. Bietsch, E. Delamarche, M. Geissler, D. Juncker, H. Kind, J.-P. Renault, H. Rothuizen, H. Schmid, P. Schmidt-Winkel, R. Stutz, and H. Wolf, “Printing meets lithography: Soft approaches to high-resolution patterning,” *IBM J. Res. Dev.*, vol. 45, no. 5, pp. 697–719, 2001.
[40] R. S. Khandpur, *Printed Circuit Boards: Design, Fabrication, Assembly and Testing*. Tata McGraw-Hill Education, 2005.
[41] T. Yang and R. Van Olmen, “Robust design for a multilayer ceramic capacitor screen-printing process case study,” *J. Eng. Des.*, vol. 15, no. 5, pp. 447–457, 2004.

[42] N. Lim, J. Kim, S. Lee, N. Kim, and G. Cho, “Screen Printed Resonant Tags for Electronic Article Surveillance Tags,” *IEEE Trans. Adv. Packag.*, vol. 32, no. 1, pp. 72–76, Feb. 2009.
[43] K. Gilleo, “Rheology and Surface Chemistry for Screen Printing,” *Screen Print. Web Httpettrends ComfilespaperuploadsRheology 20and 20Surface 20Chemistry 20for 20Screen 20Print Ing Pdf*, 1989.
[44] P. K. Wright, D. A. Dornfeld, A. Chen, C. C. Ho, and J. W. Evans, “Dispenser printing for prototyping microscale devices,” *Trans NAMRISME*, vol. 38, pp. 555–561, 2010.
[45] C. C. Ho, J. W. Evans, and P. K. Wright, “Direct write dispenser printing of a zinc microbattery with an ionic liquid gel electrolyte,” *J. Micromechanics Microengineering*, vol. 20, no. 10, p. 104009, Oct. 2010.
[46] C. C. Ho, D. Steingart, J. Evans, and P. Wright, “Tailoring Electrochemical Capacitor Energy Storage Using Direct Write Dispenser Printing,” *ECS Trans.*, vol. 16, no. 1, pp. 35–47, Dec. 2008.
[47] K. T. Braam, S. K. Volkman, and V. Subramanian, “Characterization and optimization of a printed, primary silver–zinc battery,” *J. Power Sources*, vol. 199, no. 0, pp. 367–372, Feb. 2012.
[48] J. Daniel, “Printed Electronics: Technologies, Challenges and Applications,” presented at the International Workshop on Flexible and Printed Electronics (IWFPE 10), Muju Resort, Korea, 08-Sep-2010.
[49] A. M. Gaikwad, D. A. Steingart, T. N. Ng, D. E. Schwartz, and G. L. Whiting, “A flexible high potential printed battery for powering printed electronics,” *Appl. Phys. Lett.*, vol. 102, no. 23, p. 233302, Jun. 2013.
[50] C. Ho, J. Evans, M. Mark, J. Rabaey, M. Koplow, L. Miller, A. Chen, E. Reilly, and P. Wright, “Technologies for an Autonomous Wireless Home Healthcare System,” in *Sixth International Workshop on Wearable and Implantable Body Sensor Networks, 2009. BSN 2009*, 2009, pp. 29–34.
[51] M. Attaran, “RFID: an enabler of supply chain operations,” *Supply Chain Manag. Int. J.*, vol. 12, no. 4, pp. 249–257, Jun. 2007.
[52] M. Bustillo, “Wal-Mart radio tags to track clothing,” *Wall Str. J.*, vol. 23, p. A1, 2010.
[53] S.-M. Wu, J.-R. Yang, and T.-Y. Liu, “A transponder IC for wireless identification systems,” in *Personal, Indoor and Mobile Radio Communications, 1996. PIMRC’96., Seventh IEEE International Symposium on*, 1996, vol. 1, pp. 238 –241 vol.1.
[54] N. Cho, S.-J. Song, S. Kim, S. Kim, and H.-J. Yoo, “A 5.1- mu;W UHF RFID tag chip integrated with sensors for wireless environmental monitoring,” in *Solid-State Circuits Conference, 2005. ESSCIRC 2005. Proceedings of the 31st European*, 2005, pp. 279 – 282.
[55] V. Subramanian, J. B. Chang, A. de la Fuente Vornbrock, D. C. Huang, L. Jagannathan, F. Liao, B. Mattis, S. Molesa, D. R. Redinger, D. Soltman, S. K. Volkman, and Qintao Zhang, “Printed electronics for low-cost electronic systems: Technology status and application development,” in *Solid-State Circuits Conference, 2008. ESSCIRC 2008. 34th European*, 2008, pp. 17–24.
[56] V. Subramanian, J. M. J. Frechet, P. C. Chang, D. C. Huang, J. B. Lee, S. E. Molesa, A. R. Murphy, D. R. Redinger, and S. K. Volkman, “Progress Toward Development of All-Printed RFID Tags: Materials, Processes, and Devices,” *Proc. IEEE*, vol. 93, no. 7, pp. 1330–1338, 2005.
[57] J. W. Long, B. Dunn, D. R. Rolison, and H. S. White, “Three-dimensional battery architectures,” *Chem. Rev.*, vol. 104, no. 10, pp. 4463–4492, 2004.
[58] K. Sun, T.-S. Wei, B. Y. Ahn, J. Y. Seo, S. J. Dillon, and J. A. Lewis, “3D Printing of Interdigitated Li-Ion Microbattery Architectures,” *Adv. Mater.*, vol. 25, no. 33, pp. 4539–4543, Sep. 2013.
[59] H.-S. Min, B. Y. Park, L. Taherabadi, C. Wang, Y. Yeh, R. Zaouk, M. J. Madou, and B. Dunn, “Fabrication and properties of a carbon/polypyrrole three-dimensional microbattery,” *J. Power Sources*, vol. 178, no. 2, pp. 795–800, Apr. 2008.
[60] J.-M. Tarascon and M. Armand, “Issues and challenges facing rechargeable lithium batteries,” *Nature*, vol. 414, no. 6861, pp. 359–367, Nov. 2001.

[61] M. M. Thackeray, C. Wolverton, and E. D. Isaacs, “Electrical energy storage for transportation—approaching the limits of, and going beyond, lithium-ion batteries,” *Energy Environ. Sci.*, vol. 5, no. 7, p. 7854, 2012.
[62] J. B. Goodenough and K.-S. Park, “The Li-Ion Rechargeable Battery: A Perspective,” *J. Am. Chem. Soc.*, vol. 135, no. 4, pp. 1167–1176, Jan. 2013.
[63] A. J. Smith, J. C. Burns, and J. R. Dahn, “A High Precision Study of the Coulombic Efficiency of Li-Ion Batteries,” *Electrochem. Solid-State Lett.*, vol. 13, no. 12, pp. A177–A179, Dec. 2010.
[64] X. Z. Niu, S. L. Peng, L. Y. Liu, W. J. Wen, and P. Sheng, “Characterizing and Patterning of PDMS-Based Conducting Composites,” *Adv. Mater.*, vol. 19, no. 18, pp. 2682–2686, 2007.
[65] A. Hammami, N. Raymond, and M. Armand, “Lithium-ion batteries: Runaway risk of forming toxic compounds,” *Nature*, vol. 424, no. 6949, pp. 635–636, Aug. 2003.
[66] J. Y. Song, Y. Y. Wang, and C. C. Wan, “Review of gel-type polymer electrolytes for lithium-ion batteries,” *J. Power Sources*, vol. 77, no. 2, pp. 183–197, Feb. 1999.
[67] N. Singh, C. Galande, A. Miranda, A. Mathkar, W. Gao, A. L. M. Reddy, A. Vlad, and P. M. Ajayan, “Paintable Battery,” *Sci. Rep.*, vol. 2, Jun. 2012.
[68] “Solicore Extends Technology Innovation with World’s First Digitally Printed Battery - Technology News - redOrbit.” [Online]. Available: http://www.redorbit.com/news/technology/1113007153/solicore-extends-technology-innovation-with-worlds-first-digitally-printed-battery/. [Accessed: 14-Apr-2014].
[69] A. Kozawa and R. A. Powers, “Electrochemical reactions in batteries. Emphasizing the MnO2 cathode of dry cells,” *J. Chem. Educ.*, vol. 49, no. 9, p. 587, Sep. 1972.
[70] “Ultra Thin Battery | UT Series.” [Online]. Available: http://www.bluesparktechnologies.com/index.php/products-and-services/battery-products/ultra-thin-series. [Accessed: 14-Apr-2014].
[71] A. Himy, *Silver-Zinc Battery: Phenomena and Design Principles*, First. New York, New York: Vantage Press, Inc, 1996.
[72] J. W. Schultze, *Electrochemical microsystem technologies*. CRC Press, 2002.
[73] N. A. Hampson, J. B. Lee, and J. R. Morley, “The electrochemistry of oxides of silver—a short review,” *Electrochimica Acta*, vol. 16, no. 5, pp. 637–642, May 1971.
[74] D. F. Smith, G. R. Graybill, R. K. Grubbs, and J. A. Gucinski, “New developments in very high rate silver oxide electrodes,” *J. Power Sources*, vol. 65, no. 1–2, pp. 47–52, Mar. 1997.
[75] D. Linden and T. B. Reddy, *Handbook of batteries*. McGraw-Hill, 2002.
[76] S. Arouete, K. F. Blurton, and H. G. Oswin, “Controlled Current Deposition of Zinc from Alkaline Solution,” *J. Electrochem. Soc.*, vol. 116, no. 2, pp. 166–169, Feb. 1969.
[77] F. R. McLarnon and E. J. Cairns, “The Secondary Alkaline Zinc Electrode,” *J. Electrochem. Soc.*, vol. 138, no. 2, pp. 645–656, Feb. 1991.
[78] K. M. C C Ho, “A super ink jet printed zinc–silver 3D microbattery,” *J. Micromechanics Microengineering*, vol. 19, no. 9, p. 094013, 2009.
[79] C. B. Arnold, H. Kim, and A. Piqué, “Laser direct write of planar alkaline microbatteries,” *Appl. Phys. A*, vol. 79, no. 3, pp. 417–420, Aug. 2004.
[80] “Silver Prices Per Ounce Today.” Silver Price OZ.
[81] D. Huang, F. Liao, S. Molesa, D. Redinger, and V. Subramanian, “Plastic-Compatible Low Resistance Printable Gold Nanoparticle Conductors for Flexible Electronics,” *J. Electrochem. Soc.*, vol. 150, no. 7, pp. G412–G417, Jul. 2003.
[82] P. Arora and Z. Zhang, “Battery separators,” *Chem. Rev.*, vol. 104, no. 10, pp. 4419–4462, 2004.
[83] M. Gallo, “Cellulosic Fibers for Alkaline Battery Separators.”

[84] G. A. Ghiurcan, C.-C. Liu, A. Webber, and F. H. Feddrix, “Development and Characterization of a Thick-Film Printed Zinc-Alkaline Battery,” *J. Electrochem. Soc.*, vol. 150, no. 7, pp. A922–A927, Jul. 2003.
[85] J. F. Fauvarque, S. Guinot, N. Bouzir, E. Salmon, and J. F. Penneau, “Alkaline poly(ethylene oxide) solid polymer electrolytes. Application to nickel secondary batteries,” *Electrochimica Acta*, vol. 40, no. 13–14, pp. 2449–2453, Oct. 1995.
[86] C.-C. Yang, S.-J. Lin, and S.-T. Hsu, “Synthesis and characterization of alkaline polyvinyl alcohol and poly(epichlorohydrin) blend polymer electrolytes and performance in electrochemical cells,” *J. Power Sources*, vol. 122, no. 2, pp. 210–218, Jul. 2003.
[87] D. W. Sheibley, L. C. Hsu, and M. A. Manzo, “Polyvinyl alcohol battery separator containing inert filler,” *Natl. Aeronaut. Space Adm. Rep.*, vol. -1, Jun. 1981.
[88] D. W. Sheibley, M. A. Manzo, and O. D. Gonzalez-Sanabria, “Cross-Linked Polyvinyl Alcohol Films as Alkaline Battery Separators,” *J. Electrochem. Soc.*, vol. 130, no. 2, pp. 255–259, Feb. 1983.
[89] E. T. Wise and S. G. Weber, “A Simple Partitioning Model for Reversibly Crosslinked Polymers and Application to the Poly(vinyl alcohol)/Borate System (‘Slime’),” *Macromolecules*, vol. 28, no. 24, pp. 8321–8327, Nov. 1995.
[90] F. F. Hatta, M. Z. A. Yahya, A. M. M. Ali, R. H. Y. Subban, M. K. Harun, and A. A. Mohamad, “Electrical conductivity studies on PVA/PVP-KOH alkaline solid polymer blend electrolyte,” *Ionics*, vol. 11, no. 5–6, pp. 418–422, Sep. 2005.
[91] A. Lewandowski, K. Skorupska, and J. Malinska, “Novel poly(vinyl alcohol)–KOH–H2O alkaline polymer electrolyte,” *Solid State Ion.*, vol. 133, no. 3–4, pp. 265–271, Aug. 2000.
[92] D. Berndt and D. Spahrbier, “Batteries,” in *Ullmann’s Encyclopedia of Industrial Chemistry*, Wiley-VCH Verlag GmbH & Co. KGaA, 2000.
[93] T. P. Dirkse, L. A. Vander Lugt, and H. Schnyders, “The reaction of silver oxides with potassium hydroxide,” *J. Inorg. Nucl. Chem.*, vol. 25, no. 7, pp. 859–865, Jul. 1963.
[94] P. Robert, “The Nature of Cellulose as Related to Its Application as a Zinc-Silver Oxide Battery Separator,” in *Zinc-silver oxide batteries,*, A. Fleischer and J. J. Lander, Eds. J. Wiley, pp. 263–269.
[95] J. T. L. Jr and C. B. Lundsager, “Alkaline battery with separator of high surface area,” US4287276 A01-Sep-1981.
[96] Y. Higashihata, T. Nakamura, and T. Shimizu, “Binder for batteries, and electrode compositions and batteries incorporating same,” US5707763 A13-Jan-1998.
[97] G. A. Dalin, “Improvement of Performance of Zinc Electrodes,” in *Zinc-Silver Oxide Batteries*, John Wiley & Sons, INC, pp. 87–95.
[98] L. Binder, W. Odar, and K. Kordesch, “A study of rechargeable zinc electrodes for alkaline cells requiring anodic limitation,” *J. Power Sources*, vol. 6, no. 3, pp. 271–289, Dec. 1981.
[99] N. A. Hampson, “Kinetics of the Zinc electrode,” in *Zin-silver oxide batteries*, J. J. Lander and A. Fleischer, Eds. J. Wiley, 1971, pp. 37–61.
[100] J. Zhu, Y. Zhou, and C. Gao, “Influence of surfactants on electrochemical behavior of zinc electrodes in alkaline solution,” *J. Power Sources*, vol. 72, no. 2, pp. 231–235, Apr. 1998.
[101] G. Inzelt, “Pseudo-reference Electrodes,” in *Handbook of Reference Electrodes*, G. Inzelt, A. Lewenstam, and F. Scholz, Eds. Springer Berlin Heidelberg, 2013, pp. 331–332.
[102] “Thin Flexible Batteries | Battery Solutions,” *Blue Spark battery products*. [Online]. Available: http://www.bluesparktechnologies.com/index.php/products-and-services/battery-products. [Accessed: 14-May-2014].
[103] C. C. Ho, “Dispenser Printed Zinc Microbattery with an Ionic Liquid Gel Electrolyte,” Jan. 2010.
[104] M. Ream, “The Role of Printed Carbon-Zinc Thin Film Batteries in Interactive Printed Media,” presented at the 2010 Flexible Electronics & Displays Conference, Phoenix, Arizona, 02-Feb-2010.

[105] Y. Li and C. P. Wong, “Recent advances of conductive adhesives as a lead-free alternative in electronic packaging: Materials, processing, reliability and applications,” *Mater. Sci. Eng. R Rep.*, vol. 51, no. 1–3, pp. 1–35, Jan. 2006.
[106] X. Z. Niu, S. L. Peng, L. Y. Liu, W. J. Wen, and P. Sheng, “Characterizing and Patterning of PDMS-Based Conducting Composites,” *Adv. Mater.*, vol. 19, no. 18, pp. 2682–2686, Sep. 2007.
[107] H. Cong and T. Pan, “Photopatternable Conductive PDMS Materials for Microfabrication,” *Adv. Funct. Mater.*, vol. 18, no. 13, pp. 1912–1921, Jul. 2008.
[108] “Conductive Silver Inks.” [Online]. Available: http://www.creativematerials.com/products/silver-inks/. [Accessed: 18-Apr-2014].
[109] A. Arkhireyeva and S. Hashemi, “Effect of temperature on fracture properties of an amorphous poly(ethylene terephthalate) (PET) film,” *J. Mater. Sci.*, vol. 37, no. 17, pp. 3675–3683, Sep. 2002.
[110] X. Zhu, H. Yang, Y. Cao, and X. Ai, “Preparation and electrochemical characterization of the alkaline polymer gel electrolyte polymerized from acrylic acid and KOH solution,” *Electrochimica Acta*, vol. 49, no. 16, pp. 2533–2539, Jul. 2004.
[111] H. S. Lim, J. D. Margerum, S. A. Verzwyvelt, A. M. Lackner, and R. C. Knechtli, “Degradation Mechanisms of Nylon Separator Materials for a Nickel-Cadmium Cell in KOH Electrolytes,” *J. Electrochem. Soc.*, vol. 136, no. 3, pp. 605–612, Mar. 1989.
[112] Z. Wang, Z. Wu, N. Bramnik, and S. Mitra, “Fabrication of High-Performance Flexible Alkaline Batteries by Implementing Multiwalled Carbon Nanotubes and Copolymer Separator,” *Adv. Mater.*, vol. 26, no. 6, pp. 970–976, Feb. 2014.
[113] K. Saotome, “Process for improving a water absorbent polyacrylic acid polymer and an improved polymer produced by said process,” US4783510 A08-Nov-1988.
[114] G. Bokias, A. Durand, and D. Hourdet, “Molar mass control of poly(N-isopropylacrylamide) and poly(acrylic acid) in aqueous polymerizations initiated by redox initiators based on persulfates,” *Macromol. Chem. Phys.*, vol. 199, no. 7, pp. 1387–1392, Jul. 1998.
[115] R. M. Smith and D. E. Hansen, “The pH-Rate Profile for the Hydrolysis of a Peptide Bond,” *J Am Chem Soc*, vol. 120, no. 35, pp. 8910–8913, 1998.
[116] “Ciba IRGACURE 2959 Datasheet.” Ciba Speacialty Chemicals.
[117] M. Singh, O. Odusanya, G. M. Wilmes, H. B. Eitouni, E. D. Gomez, A. J. Patel, V. L. Chen, M. J. Park, P. Fragouli, H. Iatrou, N. Hadjichristidis, D. Cookson, and N. P. Balsara, “Effect of Molecular Weight on the Mechanical and Electrical Properties of Block Copolymer Electrolytes,” *Macromolecules*, vol. 40, no. 13, pp. 4578–4585, Jun. 2007.
[118] N. A. Peppas, R. M. Ottenbrite, K. Park, and T. Okano, *Biomedical Applications of Hydrogels Handbook*. Springer, 2010.
[119] S. Wu, H. Li, and J. P. Chen, “Modeling Investigation of Volume Variation Kinetics of Fast Response Hydrogels,” *J. Macromol. Sci. Part C Polym. Rev.*, vol. 44, no. 2, pp. 113–130, 2004.
[120] W. E. Hennink and C. F. van Nostrum, “Novel crosslinking methods to design hydrogels,” *Adv. Drug Deliv. Rev.*, vol. 64, Supplement, pp. 223–236, Dec. 2012.
[121] J. E. Elliott, M. Macdonald, J. Nie, and C. N. Bowman, “Structure and swelling of poly(acrylic acid) hydrogels: effect of pH, ionic strength, and dilution on the crosslinked polymer structure,” *Polymer*, vol. 45, no. 5, pp. 1503–1510, Mar. 2004.
[122] V. F. S. GANJI FARIBA and F. E. VASHEGHANI, “THEORETICAL DESCRIPTION OF HYDROGEL SWELLING: A REVIEW,” *Iran. Polym. J. Engl.*, 2010.
[123] P. Hiemenz and T. Lodge, *Polymer Chemistry*, Second Edition. CRC Press.
[124] D. A. Steingart, A. Redfern, C. Ho, P. Wright, and J. Evans, “Jonny Galvo: A Small, Low Cost Wireless Galvanostat,” *ECS Trans.*, vol. 1, no. 21, pp. 17–22, Jun. 2006.

[125] P. Spitzer, S. Wunderli, K. Maksymiuk, A. Michalska, A. Kisiel, Z. Galus, and G. Tauber, “Reference Electrodes for Aqueous Solutions,” in *Handbook of Reference Electrodes*, G. Inzelt, A. Lewenstam, and F. Scholz, Eds. Springer Berlin Heidelberg, 2013, pp. 77–143.
[126] K. Shono, T. Kobayashi, M. Tabuchi, Y. Ohno, H. Miyashiro, and Y. Kobayashi, “Proposal of simple and novel method of capacity fading analysis using pseudo-reference electrode in lithium ion cells: Application to solvent-free lithium ion polymer batteries,” *J. Power Sources*, vol. 247, pp. 1026–1032, Feb. 2014.
[127] “Basics of Electrochemical Impedance Spectroscopy.” Gamry Instruments.
[128] L. Ramaley and C. G. Enke, “Instrumentation for the Measurement of the Electrical Double Layer Capacitance at Solid Electrodes,” *J. Electrochem. Soc.*, vol. 112, no. 9, pp. 943–947, Sep. 1965.
[129] T. P. Dirkse and R. Shoemaker, “Double Layer Capacitance of Zinc Electrodes in KOH Solutions,” *J. Electrochem. Soc.*, vol. 115, no. 8, pp. 784–786, Aug. 1968.
[130] T. P. Dirkse, D. DeWit, and R. Shoemaker, “Silver Oxide Electrode Processes,” *J. Electrochem. Soc.*, vol. 114, no. 12, pp. 1196–1200, Dec. 1967.
[131] “Testing Electrochemical Capacitors: Part 3 – Electrochemical Impedance Spectroscopy.” Gamry Instruments, 2014.
[132] J. Bisquert, “Theory of the Impedance of Electron Diffusion and Recombination in a Thin Layer,” *J. Phys. Chem. B*, vol. 106, no. 2, pp. 325–333, Jan. 2002.
[133] S. a. G. R. Karunathilaka, N. A. Hampson, T. P. Haas, R. Leek, and T. J. Sinclair, “The impedance of the alkaline zinc-mercuric oxide cell. I. Cell behaviour and interpretation of impedance spectra,” *J. Appl. Electrochem.*, vol. 11, no. 5, pp. 573–582, Sep. 1981.
[134] D. Qu, “The cause of the voltage ‘dip’ during the high rate discharge of the primary alkaline MnO2/Zn cells,” *Electrochem. Commun.*, vol. 8, no. 9, pp. 1527–1530, Sep. 2006.
[135] L. G. Austin and H. Lerner, “Review of Fundamental Investigations of Silver Oxide Electrodes,” DTIC Document, 1965.
[136] X. G. Zhang, *Corrosion and Electrochemistry of Zinc*. Springer, 1996.
[137] O. A. Petrii, R. R. Nazmutdinov, M. D. Bronshtein, and G. A. Tsirlina, “Life of the Tafel equation: Current understanding and prospects for the second century,” *Electrochimica Acta*, vol. 52, no. 11, pp. 3493–3504, Mar. 2007.
[138] H. Yang, G. V. Zhuang, and P. N. Ross Jr., “Thermal stability of LiPF6 salt and Li-ion battery electrolytes containing LiPF6,” *J. Power Sources*, vol. 161, no. 1, pp. 573–579, Oct. 2006.
[139] “Lithium Ion Cell Pouch.” [Online]. Available: http://www.eaglepicher.com/r-n-d/new-product-development/lithium-ion-cell-pouch. [Accessed: 17-Feb-2014].
[140] S. Nam, H. Park, Y. Lim, K. Lee, K. Choi, H. Hwang, G. Park, and J. Kim, “Multi layer for encapsulation comprising a planarizing organic thin layer and a conformal organic thin layer,” US20100272945 A128-Oct-2010.
[141] T. P. Dirkse and F. D. Haan, “Corrosion of the Zinc Electrode in the Silver-Zinc-Alkali Cell,” *J. Electrochem. Soc.*, vol. 105, no. 6, pp. 311–315, Jun. 1958.
[142] C. Chakkaravarthy, A. K. A. Waheed, and H. V. K. Udupa, “Zinc—air alkaline batteries — A review,” *J. Power Sources*, vol. 6, no. 3, pp. 203–228, Dec. 1981.
[143] “File:LeakedBattery 2701a.jpg,” *Wikipedia, the free encyclopedia*. .
[144] K. F. Blurton and A. F. Sammells, “Metal/air batteries: Their status and potential — a review,” *J. Power Sources*, vol. 4, no. 4, pp. 263–279, 1979.
[145] N. US Department of Commerce, “ESRL Global Monitoring Division - Global Greenhouse Gas Reference Network.” [Online]. Available: http://www.esrl.noaa.gov/gmd/ccgg/trends/. [Accessed: 31-Dec-2013].
[146] J. A. Jeevarajan and T. Inoue, *A Novel Lithium-ion Laminated Pouch Cell Tested For Performance And Safety*. 2006.

[147] C. Shen, V. R. S. S. Mokkapati, F. Santagata, A. Bossche, and P. M. Sarro, “Low temperature encapsulation of nanochannels with water inside,” in *Solid-State Sensors, Actuators and Microsystems Conference (TRANSDUCERS), 2011 16th International*, 2011, pp. 854 –857.
[148] L. K. Massey, *Permeability Properties of Plastics and Elastomers, 2nd Ed.: A Guide to Packaging and Barrier Materials*. William Andrew, 2003.
[149] F. Hensen, *Plastics Extrusion Technology*. Hanser-Gardner Publications, 1988.
[150] D. Roy, P. K. Basu, P. Raghunathan, and S. V. Eswaran, “Photo-induced cross-linking mechanism in azide–novolac negative photoresists: molecular level investigation using NMR spectroscopy,” *Magn. Reson. Chem.*, vol. 41, no. 9, pp. 671–678, Sep. 2003.
[151] G. Blagoi, M. Lillemose, D. Haefliger, A. Boisen, and S. Keller, “Processing of thin SU-8 films,” *J. Micromechanics Microengineering*, vol. 18, no. 12, pp. 125020–125029, Dec. 2008.
[152] E. W. Garnish, “Chemistry and properties of epoxide resins,” *Composites*, vol. 3, no. 3, pp. 104–111, 1972.
[153] F. W. van Der Weij, “The action of tin compounds in condensation-type RTV silicone rubbers,” *Makromol. Chem.*, vol. 181, no. 12, pp. 2541–2548, Dec. 1980.
[154] Y. Hu, V. Topolkaraev, A. Hiltner, and E. Baer, “Measurement of water vapor transmission rate in highly permeable films,” *J. Appl. Polym. Sci.*, vol. 81, no. 7, pp. 1624–1633, 2001.
[155] X. G. Zhang, “Galvanic Corrosion of Zinc and Its Alloys,” *J. Electrochem. Soc.*, vol. 143, no. 4, pp. 1472–1484, Apr. 1996.
[156] A. R. Suresh Kannan, S. Muralidharan, K. B. Sarangapani, V. Balaramachandran, and V. Kapali, “Corrosion and anodic behaviour of zinc and its ternary alloys in alkaline battery electrolytes,” *J. Power Sources*, vol. 57, no. 1–2, pp. 93–98, Sep. 1995.
[157] V. K. Nartey, L. Binder, and K. Kordesch, “Identification of organic corrosion inhibitors suitable for use in rechargeable alkaline zinc batteries,” *J. Power Sources*, vol. 52, no. 2, pp. 217–222, Dec. 1994.
[158] J. Dobryszycki and S. Biallozor, “On some organic inhibitors of zinc corrosion in alkaline media,” *Corros. Sci.*, vol. 43, no. 7, pp. 1309–1319, Jul. 2001.